June 2021

Harnessing the Mechanics of Thin-Walled Metallic Structures: from Plate-Lattice Materials to Cold-Formed Steel Shear Walls

Fani Derveni
University of Massachusetts Amherst

Recommended Citation

Derveni, Fani, "Harnessing the Mechanics of Thin-Walled Metallic Structures: from Plate-Lattice Materials to Cold-Formed Steel Shear Walls" (2021). *Doctoral Dissertations*. 2174.
https://doi.org/10.7275/22291381.0 https://scholarworks.umass.edu/dissertations_2/2174

HARNESSING THE MECHANICS OF THIN-WALLED METALLIC STRUCTURES: FROM PLATE-LATTICE MATERIALS TO COLD-FORMED STEEL SHEAR WALLS

A Dissertation Presented

by

FANI DERVENI

Submitted to the Graduate School of the
University of Massachusetts Amherst in partial fulfillment
of the requirements for the degree of

DOCTOR OF PHILOSOPHY

May 2021

Structural Engineering & Mechanics

HARNESSING THE MECHANICS OF THIN-WALLED METALLIC STRUCTURES: FROM PLATE-LATTICE MATERIALS TO COLD-FORMED STEEL SHEAR WALLS

A Dissertation Presented

by

FANI DERVENI

Approved as to style and content by:

Kara D. Peterman, Co-Chair

Simos Gerasimidis, Co-Chair

Sergio F. Breña, Member

Jessica D. Schiffman, Member

John E. Tobiason, Department Head
Civil & Environmental Engineering

ACKNOWLEDGMENTS

Back in September 2017, I was 23 years old when I decided to move to the US to pursue my PhD studies at UMass Amherst. At that time, I could not imagine how challenging and intense, but at the same time how fulfilling this journey would be almost four years later. Of course, several people played a decisive role for me during these years.

First and foremost, I would like to express my deepest gratitude to my both advisors, Profs. Kara Peterman and Simos Gerasimidis, for believing in me and for giving me this opportunity. I am indebted to their advice and support during my PhD studies and all the valuable discussions. They both, have been amazing mentors and role models for me and my career goals. I wish to say a huge thank you to both of them for giving me the chance to express my research interests, test my limits, and grow as a researcher and as a professional.

I am greatly thankful to my committee members, Profs. Sergio Brena and Jessica Schiffman, who promptly agreed to serve in my PhD committee and provide me with their valuable feedback and discussions about my work. In addition, I am extremely grateful to Profs. Benjamin Schafer, Tara Hutchinson and Andrew Gross, whose advice and support were a milestone in the completion of my PhD work. I also wish to deeply thank Profs. Sanjay Arwade and Scott Civjan for their insightful guidance and suggestions during my teaching assistanships in their classes.

My gratitude extends to Profs. Eleni Christofa and Eric Gonzales for the warm welcome in their house for many social events. I would also like to say a deep thank you to Prof. Christofa for her important recommendations about my postdoc at EPFL and Switzerland. I also wish to acknowledge all the great Professors at UMass that I had the opportunity to meet as a student in their classes. Furthermore, I would like to recognize the invaluable assistance of all UMass staff during my studies, and express my special thanks to Mark Gauthier and Jodi Ozdarski, who were always willing to help me, guide me, and discuss with me during these years.

I also wish to thank all the colleagues and friends I had the chance to meet and work with at our office in Marston building. A deep thanks to Panos, George, Kshitij, Abbas, Alaa, Fiona, Divyansh and Rhyan, while my special regards go to Hernan (and his family). Hernan, I am grateful for your huge support, encouragement, and balance you readily offer me during these four years. I cannot leave Amherst without acknowledging my friends outside of the Structural Engineering department. I am very thankful to Haris, Katerina, Iro, Ana-Maria, Antonis, Hossein, Androcles, Sofia, Andronikos, Deniz, and Rodrigo. I also had great pleasure collaborating with Zhidong and Amanpreet outside of UMass. To all my amazing friends in Greece, Poland and all around the world, a huge thanks for their support and positive vibes.

Last but certainly not least, I would like to express my sincere gratitude and appreciation to my parents and my sister for always believing in me, for supporting every decision I make, and for all their unconditional support and love. Thank you so much for always being there for me.

ABSTRACT

HARNESSING THE MECHANICS OF THIN-WALLED METALLIC
STRUCTURES: FROM PLATE-LATTICE MATERIALS TO
COLD-FORMED STEEL SHEAR WALLS

May 2021

Fani Derveni

Diploma, Aristotle University of Thessaloniki, Greece

M.S., University of Massachusetts Amherst, US

Ph.D., University of Massachusetts Amherst, US

Directed by: Drs. Kara D. Peterman and Simos Gerasimidis

Thin-walled structures have received a lot of interest during the last years due to their light weight, cost efficiency, and ease in fabrication and transportation, along with their high strength and stiffness. This dissertation focuses on the mechanical performance of thin-walled metallic structures from cold-formed steel shear walls and connections (PART I) to plate-lattice architected materials (PART II) via computational, experimental, and probabilistic methods.

Cold-formed steel (CFS) shear walls subjected to seismic loads is the focus of PART I of this dissertation. An innovative three-dimensional shell finite element model of oriented strand board (OSB) sheathed CFS shear walls is introduced and benchmarked by nine different experimental studies. Particular attention is given to the fastener behavior since they are governed by significant inherent variability and they represent a dominant failure mechanism in CFS shear walls. Shear fastener behavior is experimentally determined and introduced into the finite element approach. To further address the connection variability, an extensive parametric analysis accompanied by Monte Carlo simulations are conducted. Design recommendations for higher capacity sheathings (fiber cement board (FCB) and steel-gypsum (SG) composite board) that are not currently enabled in design specifications are also introduced.

Architected plate-lattice materials subjected to uniaxial compression is the focus of PART II of this dissertation. Architected materials are structures whose mechanical performance is governed by their geometry rather than their constituent material. Plate-lattices are composed of plates along the planes of crystalline structures. They represent the stiffest and strongest existing materials, since they can reach the Hashin-Shtrikman and the Suquet upper bounds. The stability and imperfection sensitivity of plate-lattices are evaluated in this work via elastic and plastic shell finite element analyses. Plate-lattice geometries of cubic symmetry are examined, such as the simple cubic (SC), the body-centered cubic (BCC), the face-centered cubic (FCC) structures and their combinations (SC-BCC, SC-FCC) over a range of relative densities between ρ^*=0.5% and ρ^*=25%. Imperfections are characterized by modal shapes at five different imperfection amplitudes. Finally, knockdown factors are recommended for these metamaterials.

TABLE OF CONTENTS

List of Figures

List of Tables

Part I:

Lateral Performance of Cold-Formed Steel Shear Walls and Connections

1 INTRODUCTION: PART I

1.1 Cold-formed steel shear walls: background and motivation

Cold-formed steel (CFS) has demonstrated a significant escalation and a wide use in low- and mid-rise repetitively-framed construction in the last 50 years, due to its numerous advantages over traditional structural engineering materials. Chief among these are high strength-to-weight ratio, low-cost maintenance, high durability, recyclability, non-combustibility, and, ease in installation and prefabrication. CFS is used for both structural and non-structural applications and can be used as lateral force resisting systems. Additionally, CFS is extensively used as partition walls and in secondary systems (such as purlins or girts) in metal buildings. CFS-framed buildings enable efficient on-site and remote-site fabrication methods via modularization. Shear walls are the primary lateral load resisting system in CFS construction. Typical CFS shear walls are comprised of the main structural frame (CFS stud lipped channels and CFS track unlipped channels) connected to x-bracing or sheathing on the exterior and/or in the interior, such as wood panels, steel sheets, cement-based panels, gypsum-based boards. To eliminate the overturning moment and prevent the wall uplift under earthquake or wind events, hold-downs or tie-rods are used at the base of the wall. Additional components, such as a ledger track, vertical and horizontal seams can be also present in shear wall construction. A typical CFS shear wall graphical representation is illustrated in Fig. 1.1.

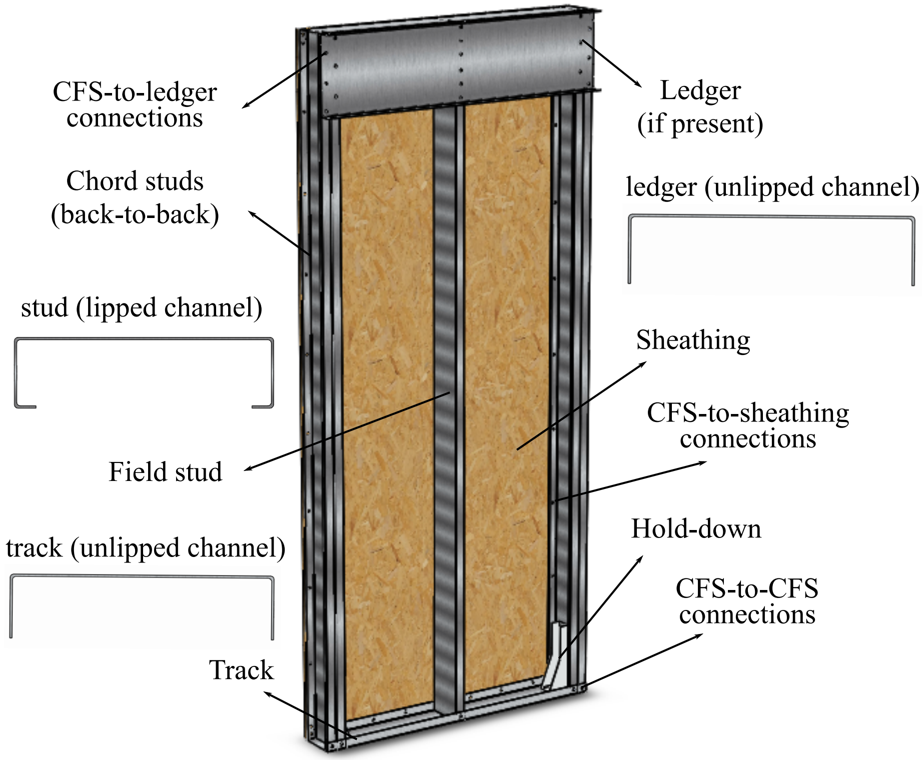

Figure 1.1: Typical sheathed cold-formed steel (CFS) shear wall configuration and details. CFS studs (lipped channels) and CFS tracks (unlipped channels) represent the wall structural frame connected to sheathing panels in the exterior side, and connected to the foundation by hold-downs. Construction details, such as ledger track and/or vertical seam, might be present.

CFS shear walls have seen significant study worldwide, with a wealth of experimental, computational and analytical results aimed at understanding their behavior. Recently, there are various experimental studies on wood-, and steel-sheathed CFS shear walls focused on the shear capacity predictions of different shear wall configurations. These are discussed in the subsequent literature review. In aggregate, they explore a wide range of characteristics influencing structural behavior. Since full-scale shear wall tests are a cost-intensive research approach, the next step in shear wall analysis is to develop a robust computational tool to enable greater innovation in the industry. That necessitates the introduction of a generalized benchmark computational approach, that can account for different wall configurations and details, as well as the variable CFS connection response, and can allow for deterministic wall response assessment.

Furthermore, current AISI-S400 [5] design provisions include CFS shear wall capacity predictions for wood- and steel-sheathed walls limited to very specific CFS and sheathing thicknesses, specific screw diameters and specific fastener spacings. That means that there is not only a need for enhancing the current provisions with different parameters and wall characteristics, but also a need for expanding the design code into new higher lateral capacity systems in order to enable their adoption and use by practitioners. Recently, cementitious and gypsum-based composite panels have explored onto the construction market due to their higher fire and weather resistance, long-life span, lower acoustic transmission, and superior mechanical properties. Design recommendations are required for these CFS shear wall systems in order to enable their adoption within design specifications and allow for safe and efficient structural alternatives to the state-of-the-practice methods.

As modern engineering practice pushes innovative, effective and sustainable construction methods to the forefront, it is essential for behavior to lead the way. This work successfully benchmarks a new high fidelity modeling approach, and provides the first insights into the performance of CFS shear walls sheathed in cementitious and composite panels.

1.2 Literature review

Cold-formed steel research can be loosely divided into system-level investigations (such as full buildings), subsystem-level evaluation (such as shear walls) and component-level assessment (such as connections or members). Each has seen significant research effort in recent decades around the world. Furthermore, different experimental, finite element, analytical, theoretical, and probabilistic methods have been used to shed light on the lateral performance of CFS framing systems.

1.2.1 CFS full-building level research

Full CFS system behavior has been evaluated under different loading conditions and different building characteristics. A two-story OSB-sheathed CFS building subjected to earthquake loading was examined by Schafer et al. [89], as a part of the recent CFS-NEES project. Both non-destructive and destructive testing (Peterman et al. [84], Peterman et al. [85]) has been conducted, as well as a computational modeling approach (Leng et al. [67]). Furthermore, a five-story CFS building behavior sheathed with composite steel-gypsum panels tested by Wang et al. [110] under seismic loading, demonstrating physical damage in shear wall components used in architectural facades. A six-story CFS building sheathed with steel-gypsum sheathings is subjected to seismic events, post-seismic fire exposure and post-fire earthquake events in Hutchinson et al. [59], displaying various component failure mechanisms, while the building resisted collapse.

1.2.2 CFS sub-system shear wall level research

Sub-system shear wall lateral performance is experimentally investigated by various researches throughout US and Canada. CFS shear walls sheathed with OSB, gypsum wallboard, plywood, and FiberBond wallboard are tested by Santa Clara University (Serrette et al. [95], Serrette et al. [96], Serrette et al. [94], Serrette et al. [97]). These tests predicted shear wall capacities of OSB-sheathed CFS shear walls which have been adopted by the design code provisions in the North American Standard. McGill University (Branston et al. [19], Branston [18], Chen [24], Blais [15], Hikita [57]) has explored the lateral performance of OSB- and plywood-sheathed CFS shear walls under monotonic and reversed cyclic loading. The effect of shear wall aspect ratio, fastener spacing and CFS thickness was evaluated to further improve the CFS design guidelines. OSB-sheathed shear walls of different wall aspect ratios and field stud thickness, as well as additional details such as ledger, vertical and horizontal seams, and interior gypsum board have been laterally tested by Johns Hopkins University (Liu et al. [70]), Liu et al. [69]) to enhance the design possibilities with walls composed of different construction details. OSB-sheathed shear wall response was dominated by the shear fastener behavior between the structural frame and the sheathing panels.

CFS shear walls sheathed with steel sheets have been also extensively examined via different experimental programs. The impact of wall aspect ratio, steel sheet thickness, and spacing of the screws on steel-sheathed wall response was examined by Yu [116]. The effect of loading condition, CFS profile thickness and framing type was studied by DaBreo et al. [27]. Singh et al. [100] investigated the impact of exterior finish and wall type in steel-sheathed wall response through shake table seismic and monotonic tests. Furthermore, shear walls sheathed with corrugated steel have been experimentally evaluated under lateral and/or gravity loading (Fülöp and Dubina [46], Zhang et al. [118]). Towards an effort of reaching higher shear capacities, different gypsum-based and cement-based materials have received an increasing interest from the research community and design practice. Shear walls sheathed with fiber cement board (FCB) sheathing have been tested under monotonic and/or cyclic loading (Zeynalian and Ronagh [117], Khaliq and Moghis [64]), while shear walls sheathed with steel-gypsum (SG) have been tested under cyclic and fire loading by Hoehler et al. [58]. Resistant gypsum-based sheathings have been also studied through subsystem tests (Macillo et al. [72]) and full building tests (Fiorino et al. [42]). The effect of different sheathings, such as steel, gypsum, fiber cement board, steel and gypsum composite, fiber cement board and steel composite, is examined under cyclic loading by Mohebbi et al. [76], demonstrating that higher wall strength and stiffness occurred when FCB and gypsum sheathings are present in comparison to bare steel sheathing.

CFS shear wall finite element analyses have been conducted using different softwares and methods. The finite element software OpenSees [74] is used to introduce performance-based modeling approaches for OSB-sheathed CFS shear walls (Buonopane et al. [20], Bian et al. [14], Kechidi and Bourahla [63]), while software DRAIN-3DX is used through a spring representation (Fülöp and Dubina [46]). In addition, finite element software ABAQUS (ABAQUS [1]) is used towards a high fidelity modeling approach for OSB-sheathed walls emphasizing fastener response (Ngo [78], Ding [37]), while focusing on specific shear wall configurations and characteristics and underestimating their capacity. Steel-sheathed CFS shear walls have been also computationally explored via phenomenological performance-based modeling in OpenSees (Singh and Hutchinson [99]) and high-fidelity modeling in ABAQUS (Zhang et al. [118]). Gypsum-based CFS shear wall finite element modeling is conducted by Fiorino et al. [44] through SAP2000 detailed modeling, and unified truss models in OpenSees. Even though, multiple experimental research efforts exist for sheathed CFS shear walls, a robust high fidelity computational benchmark tool capable of capturing strength, stiffness and failures for a variety of sheathings and wall characteristics has not yet been reported.

1.2.3 CFS connection level research

Numerous research efforts have been conducted to experimentally assess the connection response between cold-formed steel members and sheathing. CFS-to-wood connection shear behavior was evaluated by Okasha [79] through different component thicknesses and wood orientations, while CFS-to-OSB and CFS-to-gypsum connection response is examined under monotonic and cyclic loading by Peterman et al. [83], investigating the effect of fastener spacing and CFS thickness, and extracting Pinching4 parameters to describe their un- and re-loading behavior. The shear connection behavior of OSB- and gypsum-sheathed CFS studs is tested under monotonic and cyclic loading by Fiorino et al. [40], investigating the impact of sheathing orientation, screw edge distance, as well as cyclic protocol and load rate, while additionally the effect of humidity, screw over-driving, screw spacing, and specimen re-use is monotonically examined (Vieira and Schafer [107], Vieira Jr and Schafer [108]). The CFS-to-OSB connection shear response is also examined via a random fastener characterization of a lognormal distribution by Bian et al. [13], aiming to address the inherent variability of these fasteners and understand their impact in shear wall response through Monte Carlo simulations.

Different sheathing types, such as OSB, steel, plywood, and gypsum, connected to CFS members were tested through single-screw tests by Tao et al. [106] and Pinching4 shear connection parameters were extracted, while steel-sheathed connection specimens are tested under monotonic and asymmetric cyclic loading by Zhang et al. [119]. Shear connection behavior between CFS members and cement-based and gypsum-based sheathing materials were also monotonically tested (Selvaraj and Madhavan [93], Fiorino et al. [43]). Besides shear connection response evaluation, pull-out steel-to-steel connection behavior was recently monotonically tested by Castaneda and Peterman [22] by varying the CFS steel sheet thickness. Although CFS-to-OSB shear connection behavior has been determined experimentally, none of these test programs test sufficient repetitions to enable a statistical characterization of the variability. Furthermore, limited studies have been conducted on the impact of higher capacity sheathings, such as FCB and SG composite, on the hysteretic shear connection behavior.

1.3 Dissertation organization of PART I

The main goal of this work is to provide an innovative benchmark fastener-based shear wall modeling approach for sheathed CFS shear walls under lateral loading through experimentally-obtained fastener data and to enhance the possibilities of efficient and higher capacity design options through design guideline recommendations.

PART I of this dissertation is organized as follows:

- Chapter 1 (this Chapter) includes the introduction and motivation for PART I of this dissertation, as well as the literature review for the examined fields and the contribution of this study to the research community and the design practice.

- Chapter 2 focuses on the lateral behavior of oriented strand board (OSB) sheathed cold-formed steel (CFS) shear walls by introducing and validating an experimentally-derived fastener-based computational approach. Analytically, this Chapter is composed of an experimental program of 30 identical CFS-to-OSB variable connection specimens, a finite element model of OSB-sheathed CFS shear walls introduction and validation by previous experimental studies, and an extensive parametric analysis and reliability of the modeling parameters. This Chapter presents the work of Derveni et al. [32], and [28], [31].

- Chapter 3 presents the recommended design guidelines for CFS shear walls sheathed with fiber cement board (FCB) and steel-gypsum (SG) composite panels through fasterner-based modeling, as well as the proposed fastener hysteretic characterization. In detail, this Chapter consists of an experimental program of 18 CFS-to-FCB and CFS-to-SG connection specimens under monotonic and cyclic loading, a Pinching4 model connection characterization, a computational model of FCB- and SG-sheathed CFS shear walls, and a shear capacity design predictions recommendation and validation. This Chapter presents the work of Derveni et al. [29], and [30].

- Chapter 4 includes the summary and overall conclusions of PART I of this dissertation, as well as potential future extensions of this work.

2 EXPERIMENTALLY DERIVED FASTENER-BASED FINITE ELEMENT MODELING OF COLD-FORMED STEEL SHEAR WALLS

Chapter overview: This chapter evaluates the lateral response of oriented strand-board (OSB) sheathed cold-formed steel (CFS) shear walls, introduces a benchmark finite element modeling approach, conducts an experimental program of 30 connection specimens, and examines connection variability in shear wall behavior through a parametric analysis and Monte Carlo simulations.

2.1 Experimental program of CFS-to-sheathing shear connections

Shear connection behavior represents the dominant failure mechanism of oriented strand board (OSB) sheathed cold-formed steel (CFS) shear walls necessitating the full characterization of their strength, stiffness, ductility, degradation, failure modes, and statistical variability. The shear connection behavior is investigated herein through 30 identical CFS-to-OSB connection experiments to obtain statistically significant data.

2.1.1 Test specimen and test rig

The test program is composed of stud-screw-sheathing assemblies subjected to monotonic loading, as adapted from Peterman et al. [83]. Two OSB sheathing sheets are connected to two CFS studs on both sides with eight CFS-to-OSB fasteners, as shown in Fig. 2.1. Hot-rolled steel plates enclose the CFS stud webs (Fig. 2.1c, Fig. 2.1d), aiming to restrain the deformation of the web of the studs and to lead the failure to the fasteners. Loading is applied at the top part of the specimen, while the bottom part is fixed. The test rig is illustrated in Fig. A.1a in Appendix A.

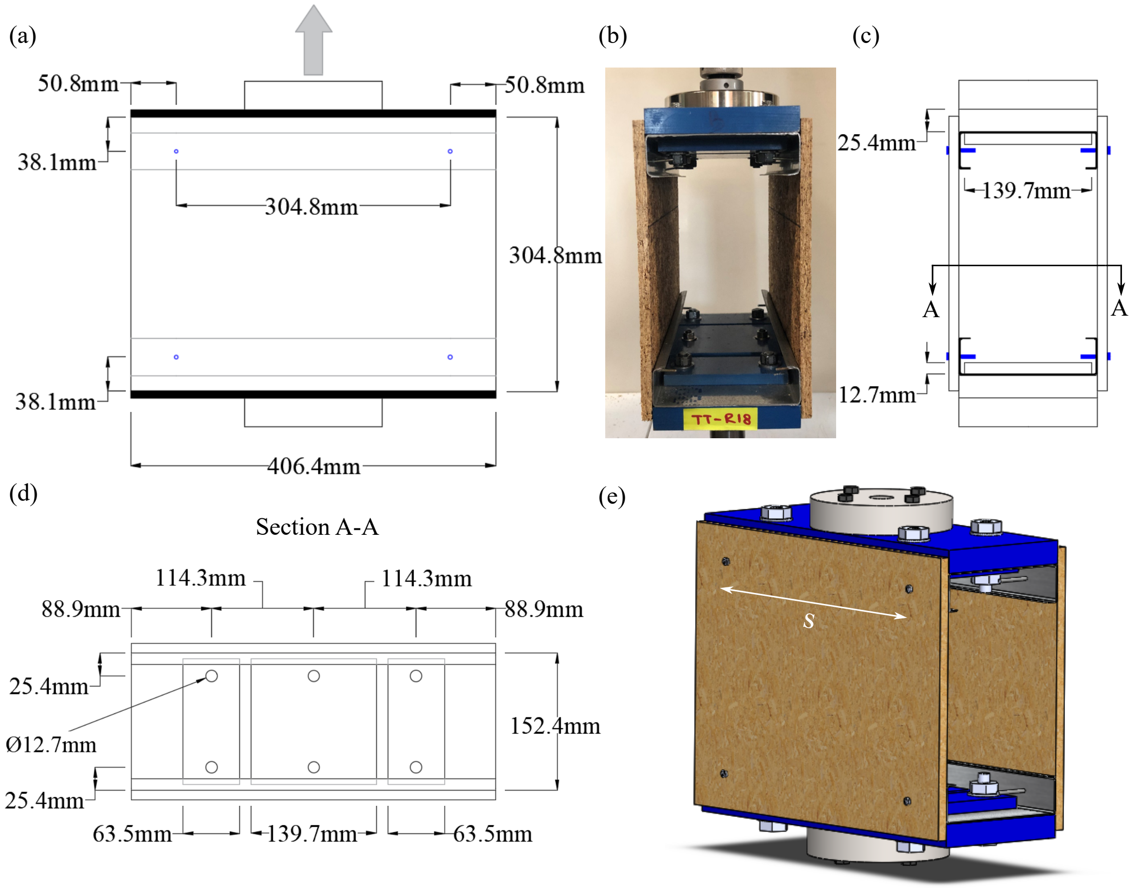

Figure 2.1: Test rig and connection specimens (stud-screw-sheathing). (a) Front view of the specimen indicating loading direction, (b) actual test specimen photo in the rig, (c) side view of the specimen indicating steel plate dimensions, (d) inside view of the specimen representing A-A section, and (e) isometric view of the specimen indicating the fastener spacing s=304.8 mm. A test program of 30 identical experiments is conducted to examine connection variability.

The specimens are constructed of 304.8 mm x 406.4 mm (12 in. x 16 in.) of 11.11 mm (7/16 in.) thick, Exposure 1 OSB sheathing sheets connected to 1.37 mm (54 mils) thick CFS studs (lipped channel sections) of 152.4 mm deep web, 41.3 mm wide flange, 12.7 mm deep lip (600S162-54 notation in AISI-S200 [4]). OSB sheathing and CFS members are connected via M4 x 50 (No. 8) flathead QuickDrive screws located at 38.1 mm (1.5 in.) from the edge of the sheathing in the center of the flanges of the studs (AISI-S100 [3]) and spaced every s=304.8 mm (12 in.). In real shear walls, fasteners tilt parallel to the stud flanges, and do not bear on the studs. This test setup causes the fasteners to tilt perpendicular to the flanges, leading to bearing at large deformations. To avoid fastener bearing on the web of CFS studs due to the excessive fastener tilting during the tests, all screw edges were cut. Based on Vieira and Schafer [107], screw edge cutting does not affect the connection behavior, and prevents failure phenomena not present in actual shear wall behavior.

2.1.2 System test connection results of 30 identical specimens

System force-displacement behavior of the 30 identical tests is illustrated in Fig. 2.2c, indicating a significant 38% peak strength variability. The governing connection failure modes were either screw pull-through (occurred in 21 specimens) or screw shear failure (occurred in 9 specimens). Actual specimen pictures after testing depicting pull-through and shear failures are shown in Fig. 2.2a and Fig. 2.2b respectively. The progression of failure between the different screws depends on minute differences in screw installation, sheathing and steel geometric imperfections, and localized sheathing properties, which allow any screw to fail before others randomly.

Screw pull-through failure mode is a progressive failure mechanism. At the beginning of each test, tilting of all screws is initiated until the pull-through of some of the screws which is followed by the localized sheathing bearing in the locations of the screws.

Shear screw failure mode is governed by abrupt drops in the force-displacement behavior. Tilting of the fasteners is observed until the shear failure of some screws becomes present. Pull-through across some of the fasteners is also observed post-peak leading to local bearing of OSB sheathing.

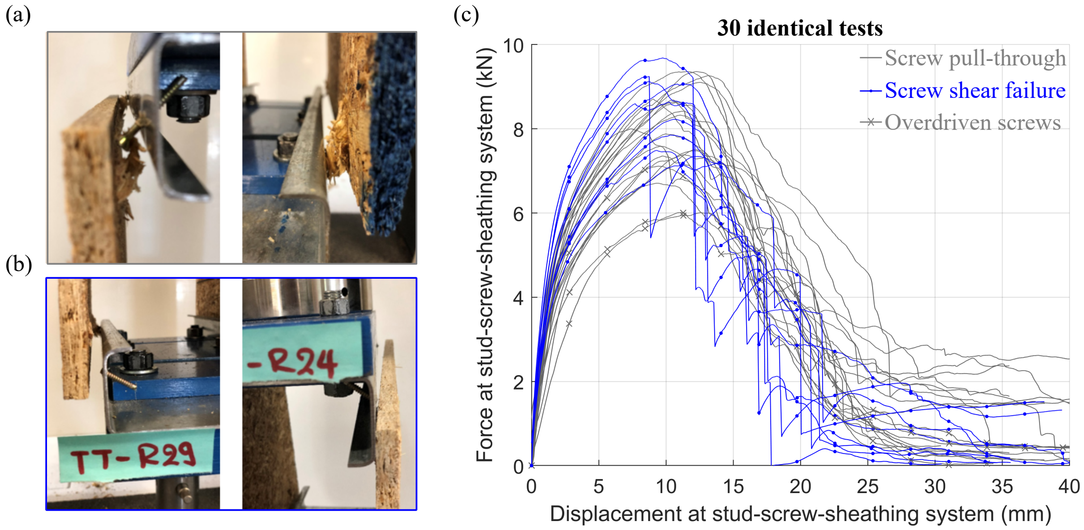

Figure 2.2: Experimental system shear fastener results of 30 tests under monotonic loading. The governing failure mechanisms of these systems are either (a) screw pull-through (photos of actual specimens after testing) or (b) shear screw failure (photos of actual specimens after testing). (c) Force-displacement illustration of system connection behavior including the response of the different failure modes, as well as the over-driven screws impact.

The impact of over-driven screws is also examined via three tested specimens indicated in Fig. 2.2c with cross markers. Each of these specimens included one over-driven screw which was backed out to flush with the OSB sheathing. The results illustrate lower predicted capacities of these instances, as also described by Vieira and Schafer [107]. Screw over-driving is a common construction error which allows the screw to pull-through easier and faster while bearing, and thus it affects the connection capacity. Tensile coupon testing of CFS studs taken from the same batch with the specimens that failed due to both screw pull-through and shear screw failure resulted to yield strength of 332 MPa (48 ksi) and 335 MPa (51 ksi) respectively. The stress-strain response of the coupon tests is illustrated in Fig. A.2b in the Appendix A.

2.1.3 Individual screw response conversion

System connection testing is chosen over individual screw testing to account for and reduce connection variable response. To convert the response of the system of eight fasteners to the response of each single fastener, Eq. 1, Eq. 2 and Eq. 3 are used to calculate the individual screw force P_i, the individual screw displacement Δ_i and the individual screw stiffness K_i, respectively (derived from Vieira and Schafer [107]). Fig. 2.3a represents a schematic representation of force and displacement distribution to obtain single screw shear behavior (as illustrated in Fig. A.2a in Appendix A).

The single screw force P_i (from free body diagram in Fig. 2.3a) is calculated as:

$$P_i = \frac{P}{4} \ . \tag{1}$$

The individual fastener displacement Δ_i (deformation localization in fastener locations) is defined as:

$$\Delta_i = \frac{\Delta}{2} \ . \tag{2}$$

The stiffness per screw K_i (parallel spring model) is calculated as:

$$K_i = \frac{K}{2} \ . \tag{3}$$

where P is the system force, Δ is the system displacement, and K is the system stiffness.

2.1.4 Statistical characterization of fastener behavior

To address the CFS fastener response variability, a statistical characterization is conducted herein by using the average connection response μ of the 30 identical tests, their standard deviations σ, and their coefficient of variations COV, as summarized in Table 2.1. The mean backbone of the 30 tests is defined based on a four-point fit to data curve at 40% peak load, 80% peak load, 100% peak load and 30% post peak load, as illustrated in Fig. 2.3b. Fig. 2.3b also includes the upper and lower response bounds based on $\mu \pm \sigma$ and $\mu \pm 2\sigma$. Shaded areas indicate the reliability range of CFS-to-OSB connection data. A significant COV=12% is obtained for connection peak strength, which is within the range obtained from a previous experimental study of 5-12 test repetitions of CFS-to-OSB fasteners by Iuorio et al. [60].

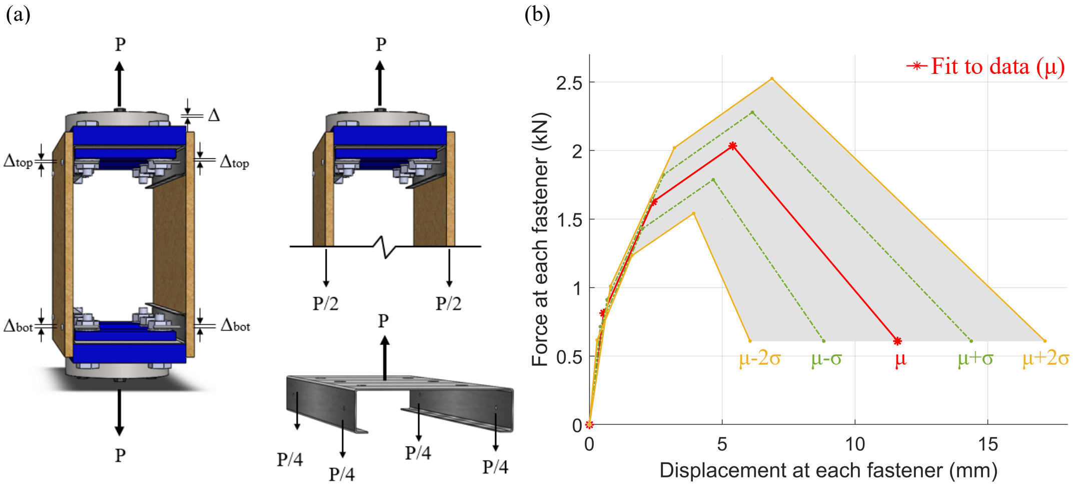

Figure 2.3: Individual screw response conversion from stud-screw-sheathing system behavior and statistical characterization. (a) Conversion of system to screw behavior via displacement and force schematic representation. (b) Individual screw force-displacement behavior using the statistical average μ of the 30 identical tests, as well as the $\mu \pm \sigma$ bounds, and $\mu \pm 2\sigma$ bounds.

Connection variability is further investigated in Section 2.4 via a probabilistic approach based on random fastener response characterization. Design codes do not include strength comparisons for these fasteners.

Table 2.1: Statistical characterization obtained from the 30 identical connection tests. P_1, P_2, P_3, P_4 denote the load and Δ_1, Δ_2, Δ_3, Δ_4 the displacement of each of the four points constructing the CFS-to-OSB fastener behavior.

Backbone data points	Mean μ (kN)	Std σ (kN)	COV (%)
P_1 @ 40% Peak load	0.814	0.098	12.10
P_2 @ 80% Peak load	1.627	0.197	12.10
P_3 @ Peak load	2.034	0.246	12.10
P_4 @ 30% Peak load	0.610	0.074	12.10
Backbone data points	Mean μ (mm)	Std σ (mm)	COV (%)
Δ_1 @ 40% Peak load	0.540	0.125	23.30
Δ_2 @ 80% Peak load	2.400	0.400	16.70
Δ_3 @ Peak load	5.400	0.737	13.80
Δ_4 @ 30% Peak load	11.60	2.800	24.00

2.2 Finite element modeling of OSB-sheathed CFS shear walls

The main focus of this study is to introduce and validate a robust benchmark finite element model of OSB-sheathed CFS shear walls. A high fidelity modeling approach is introduced by using the finite element software ABAQUS [1], and is validated by nine different wall experiments throughout US and Canada (Liu et al. [70], Branston [18], Blais [15], Hikita [57]). The introduced computational method aims to accurately capture strength, stiffness and failure mechanisms of OSB-sheathed walls regardless of wall configuration, dimensions, and different components and details. All the examined shear walls adopted in this work are composed of a CFS structural frame composed of chord studs, field studs and tracks, OSB sheathing in one side, hold-downs in the bottom part of the walls to prevent the uplift, and screws connecting the CFS members, as well as the OSB sheathing to the CFS frame. Particular attention is given to the CFS-to-OSB connection behavior by describing it via experimental data.

2.2.1 Model geometry

The simulated OSB-sheathed CFS shear walls are adopted from two different test rigs based on the CFS-NEES study (Liu et al. [70]) and the McGill studies (Branston [18], Blais [15], Hikita [57]). Various CFS and OSB member cross-sectional properties, hold-down components and details presence (ledger, vertical seam) are investigated throughout the different examined wall configurations. A schematic representation of the simulated shear wall geometries including symbols (notation list in Appendix A) for dimensional and cross-sectional properties are illustrated in Fig. 2.4. Table 2.2 summarizes the CFS member different cross-sections, while Table 2.3 presents the different wall dimensions (aspect ratios), component thicknesses and hold-down types between the selected wall configurations.

Table 2.2: Cross-sectional dimensions of all examined CFS members (H is the web depth, B is the flange width, and D is the lip depth of each CFS component).

Wall selection	Component	Cross-section	B (mm)	H (mm)	D (mm)
Liu et al. 2014	Stud	C-lipped	41.3	152.4	12.7
	Track	C-unlipped	38.1	157.4	–
	Ledger	C-unlipped	50.8	304.8	–
Branston 2004	Stud	C-lipped	41.3	92.08	12.7
	Track	C-unlipped	30.2	92.08	–
Blais 2006 & Hikita 2006	Stud	C-lipped	41.3	92.08	12.7
	Track	C-unlipped	31.8	92.08	–

Two different wall configurations of different aspect ratios, a 1.22 m x 2.74 m (4 ft x 9 ft) and a 2.44 m x 2.74 m (8 ft x 9 ft), are adopted from Liu et al. [70] and are subjected to monotonic loading. CFS studs and tracks constitute the structural frame connected to a ledger track at the top interior wall side, to OSB sheathing at the full exterior wall side, and to hold-downs at the bottom chord stud part. The smallest aspect ratio (h/w) wall consists of an additional vertical seam in the middle field stud flange composed of two rows of connections spaced every 152.4 mm (6 in.). Horizontal seams are not included in the finite element analysis, since they do not fail during the test and they have little effect in shear wall capacity. CFS members are assembled via M5 (No. 10) screws, while CFS frame to OSB sheathing are assembled via self-drilling M4 (No. 8) flathead Simpson Quick Drive screws in both wall configurations.

Table 2.3: Wall and component dimension, and detail selection for all nine simulated CFS shear walls. (w is the wall width, h is the wall height, t_s is the OSB thickness, t_1 is the stud thickness, t_2 is the track thickness, s_p is the wall perimeter screw spacing and s_f is the wall field stud screw spacing).

Wall Database (Test No.)	w x h (m)	t_1 (mm)	t_2 (mm)	t_s (mm)	s_p (mm)	s_f (mm)	Hold-down
Liu et al. 2014 (1c)	1.22 x 2.74	1.37	1.37	11.11	152.4 *	304.8	S/HDU6
Liu et. al 2014 (11c)	2.44 x 2.74	1.37	1.37	11.11	152.4 *	304.8	S/HDU6
Hikita 2006 (51b)	1.22 x 2.44	1.37	1.09	11.11	152.4	304.8	S/HD10
Branston 2004 (21abc)	1.22 x 2.44	1.12	1.12	11.11	152.4	304.8	S/HD10
Branston 2004 (23abc)	1.22 x 2.44	1.12	1.12	11.11	101.6	304.8	S/HD10
Branston 2004 (25abc)	1.22 x 2.44	1.12	1.12	11.11	76.20	304.8	S/HD10
Blais 2006 (41abc)	1.22 x 2.44	1.09	1.09	9.525	152.4	304.8	S/HD10
Blais 2006 (43abc)	1.22 x 2.44	1.09	1.09	9.525	101.6	304.8	S/HD10
Blais 2006 (45abc)	1.22 x 2.44	1.09	1.09	9.525	76.20	304.8	S/HD10

* Staggered perimeter fastener application

Seven different wall configurations of 1.22 m x 2.44 m (4 ft x 8 ft) dimensions are adopted from McGill effort (Branston [18], Blais [15], Hikita [57]) and are subjected to monotonic loading. CFS studs and tracks consist the structural frame connected to OSB sheathing at the exterior side of the walls, and to hold-downs at the bottom part of the chord studs. The OSB sheathing is connected to the CFS members via M4 (No. 8) self-piercing screws, while studs are connected to tracks by M5 (No. 10) screws, and back-to-back chord studs are fastened through M4 (No. 8) screws. The impact of shear wall perimeter fastener spacing is investigated through three different spacings at 12.7 mm (1/2 in.) screw edge distance.

All simulated OSB-sheathed CFS shear walls are simulated using their nominal dimensions, and cross-sectional and material properties to ensure a consistent and general benchmark modeling approach. Geometric imperfections, and residuals stresses and strains are not included in this modeling method (similarly to Ngo [78] and Ding [37]) since CFS members did not buckle during the tests and the wall behavior was fastener-governed.

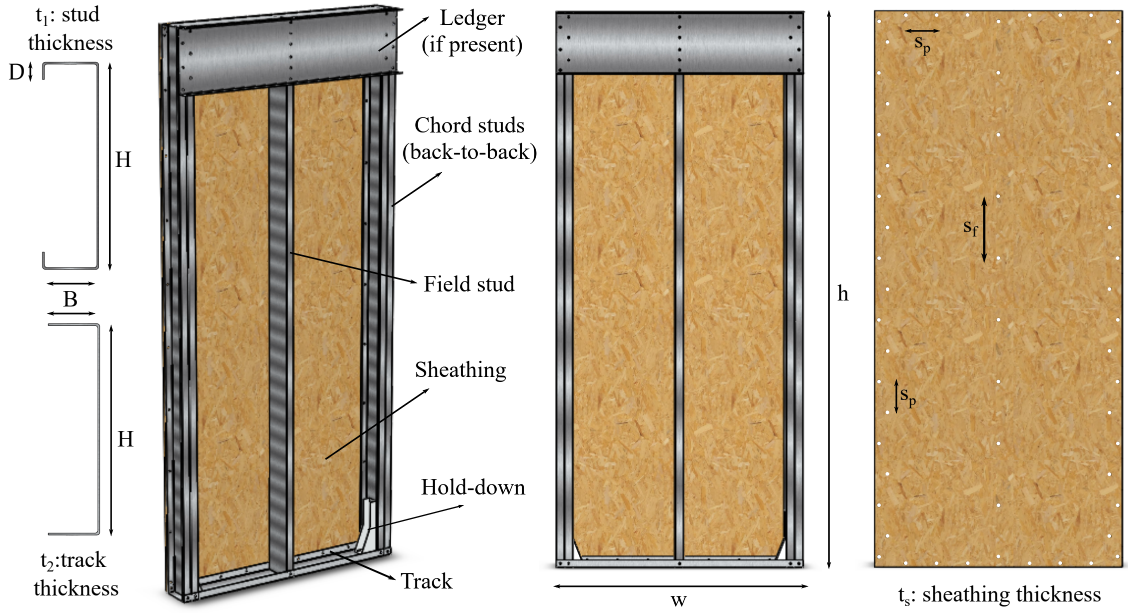

Figure 2.4: Representation of a typical OSB-sheathed CFS shear wall configuration including dimension symbols for wall and component cross-sections. Stud and track cross-sections are described by their web depth H, their flange width B, their lip depth D (for studs), and their thickness t_1 and t_2 respectively. Wall dimensions are described by their height h and their width w, while sheathing thickness is denoted as t_s. The fastener spacing is classified as perimeter spacing s_p, and field stud spacing s_f. Nine shear walls of different configurations and dimensions are simulated.

2.2.2 Mesh discretization and element type

All CFS components and OSB sheathing are constructed and assembled in ABAQUS software by using three-dimensional four-node S4R shell elements with reduced integration points. Fig. 2.5 illustrates wall schematics and different views of a typical simulated wall including the mesh of all components. A fine mesh of a size of 6.35 mm (0.25 in.) is selected for CFS members (studs, tracks, ledger) and a coarser mesh of a size of 50.8 mm (2 in.) is chosen for the OSB sheathing. CFS component mesh size and element type effects are assessed by Schafer et al. [90]. The selected fine mesh of CFS members allows for two elements in the lips of the studs, while the effect of a finer mesh of 38.1 mm (1.5 in.) in OSB sheathing is addressed in Subsection 2.3.2.

2.2.3 Material properties

The material properties of all simulated components are described herein. OSB sheathing is modeled as orthotropic elastic material, while CFS members are modeled as isotropic and elastic perfectly plastic materials.

2.2.3.1 OSB material properties

Elastic orthotropic material properties for OSB sheathing are obtained by converting the panel bending stiffness $(EI)_s$ and the panel rigidity $(Gt)_s$ into Young's modulus E_s and shear modulus G_s respectively, as analytically discussed in Schafer et al. [91]. The OSB panel bending stiffness parallel to the strength axis $(EI)_{s1}$, the panel bending stiffness perpendicular to the strength axis $(EI)_{s2}$, and the panel rigidity through thickness $(Gt)_{s12}$ are described in APA-D510C [8] for both simulated sheathing types, the 11.11 mm (7/16 in.) thick and the 9.525 mm (3/8 in.) thick OSB, as shown in Table 2.4. Eq. 4 and Eq. 5 are used to obtain the Young's modulus and the shear modulus respectively (Table 2.4).

The Young's modulus of OSB sheathing is defined as:

$$E_s = \frac{12(EI)_s}{t_s^3} \ . \tag{4}$$

The shear modulus of OSB sheathing is calculated as:

$$G_s = \frac{(Gt)_s}{t_s} \ . \tag{5}$$

where t_s is the sheathing thickness of each selected OSB panel.

Orthotropic material properties are introduced to the finite element model via Engineering Constants from ABAQUS library. To obtain orthotropic material properties, Young's modulus and shear modulus in all three-dimensions are required. The out-of-plane Young's modulus E_{s3} is set equal to E_{s2} from Table 2.4, and out-of-plane shear moduli G_{s13} and G_{s23} are set equal to G_{s12} from Table 2.4, while the Poisson's ratio v_s=0.3 is introduced in all three-dimensions. The effect of different shear moduli in shear wall response is further discussed in Subsection 2.3.2.

Table 2.4: OSB sheathing material properties. Modulus of elasticity and shear modulus are calculated based on the OSB thickness and OSB rate of the different experimental configurations.

OSB sheathing type	$(EI)_{s1}$ $(kN - mm^2/mm)$	$(EI)_{s2}$ $(kN - mm^2/mm)$	$(Gt)_{s12}$ (kN/mm)
	|| strength axis	⊥ strength axis	through thickness
11.11mm, 24/16 rated	734.36	150.64	14.62
9.525mm, 24/0 rated	564.90	103.56	13.57
OSB sheathing type	E_{s1} (MPa)	E_{s2} (MPa)	G_{s12} (MPa)
	|| strength axis	⊥ strength axis	through thickness
11.11mm, 24/16 rated	6422	1317	1316
9.525mm, 24/0 rated	7844	1438	1425

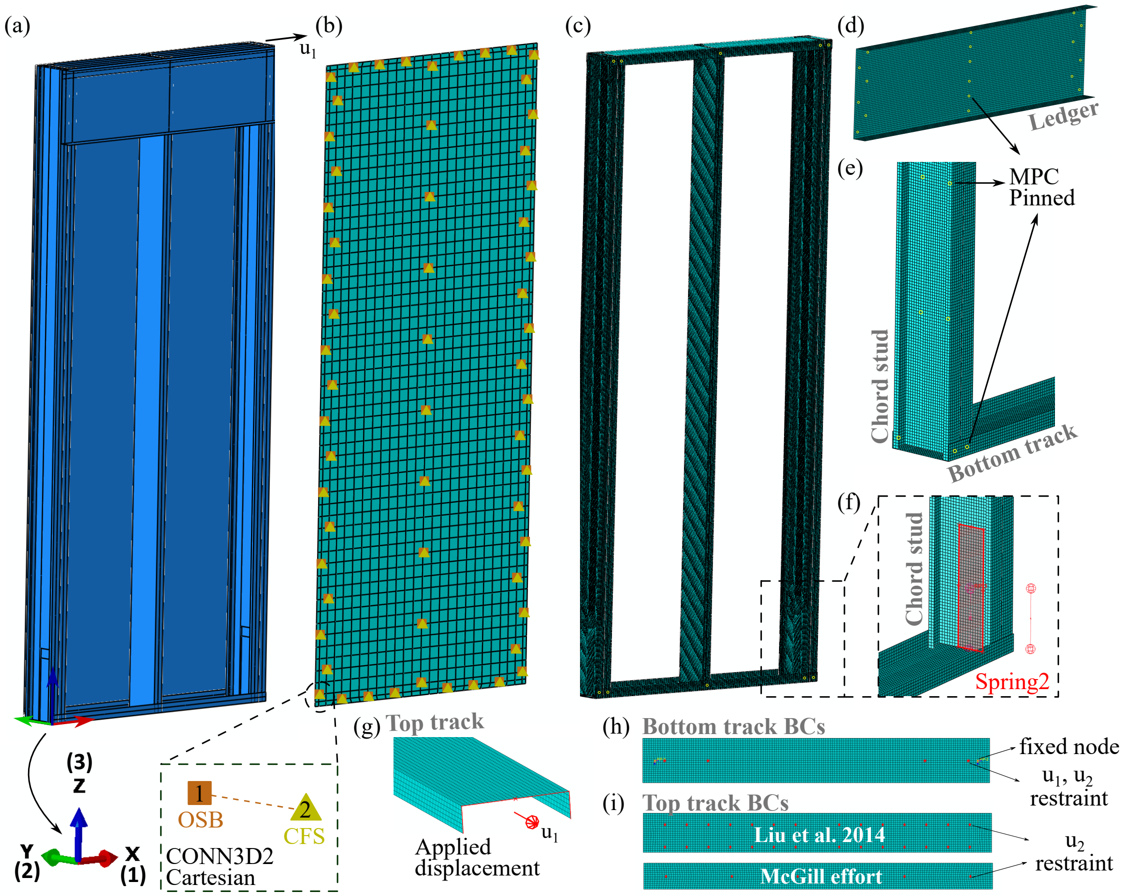

Figure 2.5: Representation of a typical simulated shear wall including mesh discretization and connection classification. (a) Shear wall assembly including the selected coordinate system and loading. (b) Mesh representation of OSB sheathing and CFS-to-OSB connection simulation via the connector element Cartesian. (b) CFS structural frame including studs, tracks and their connections. (d) Ledger mesh and its connection to the frame via MPC pinned constraints, and (e) back-to-back chords studs connected through MPC pinned constraints. (f) Hold-down representation by a rigid body and a Spring2 element. (g) Displacement control loading application at top track. (h) Bottom track and (i) top track boundary conditions for the different walls.

2.2.3.2 CFS material properties

Elastoplastic material properties are implemented in the finite element modeling approach for all CFS components. A modulus of elasticity equal to E=203 GPa

(29500 ksi), and a Poisson's ratio equal to v=0.3 remain constant between the different shear wall configurations. For the shear walls adopted from Liu et al. [70], the yield strength is equal to σ_y=344 MPa (50 ksi), while for the McGill effort walls (Branston [18], Blais [15], Hikita [57]) the yield strength is σ_y=230 MPa (33 ksi). The impact of measured yield strengths in full shear wall behavior is assessed in Subsection 2.3.2.

2.2.4 Connection simulation

Shear wall connections are classified into two categories in this work, CFS-to-CFS connections (between CFS members) and CFS-to-OSB (between CFS members and OSB sheathing), and are simulated via different modeling assumptions. CFS-to-OSB connections constitute the critical load path of OSB-sheathed shear walls during testing, while CFS-to-CFS connections did not fail during the tests.

2.2.4.1 CFS-to-CFS connection modeling

Multi-point constraints (MPC) pinned are used to simulate CFS-to-CFS connections. MPC pinned allows for independent motion of all three rotational degrees of freedom, while it constraints all three translational degrees of freedom. CFS-to-CFS connections appear in the examined CFS shear walls between a) back-to-back chord stud webs though two lines of connections spaced every 304.8 mm (12 in.) vertically, b) stud-to-track center points of their flanges (both in chord and field studs), and c) stud-to-ledger as flange-to-web connections spaced every 50.8 mm (2 in.) at top interior wall side. CFS-to-CFS connections and their location are illustrated in Figs. 2.5c, 2.5d and 2.5e.

2.2.4.2 CFS-to-OSB connection modeling

Connector elements (CONN3D2) Cartesian are selected for CFS-to-OSB connection simulation. CONN3D2 Cartesian allows for motion in all three translational degrees of freedom through an assigned nonlinear connection behavior. CFS-to-OSB connections represent the dominant failure mechanism in the full shear wall response, as discussed in the experimental studies by Liu et al. [70], Branston [18], Blais [15] and Hikita [57]. For this reason, experimentally-determined shear behavior is introduced to represent the response of these connections. Connector element behavior is assigned to wires at the locations of CFS-to-OSB connections, which are created between two matching nodes between OSB sheathing (first selected node) and CFS members (second selected node), as illustrated in Fig. 2.5b.

For the shear CFS-to-OSB connection behavior, experimental four-point nonlinear response is introduced in the finite element model based on available tests of the same screw diameters and CFS and OSB material thicknesses with the simulated shear walls. To simulate the connection behavior of the nine selected OSB-sheathed CFS shear walls, four different fastener behaviors are adopted, as summarized in Table 2.5 and illustrated in Fig. 2.6b:

- 1.37 mm CFS to 11.11 mm OSB (54 mils to 7/16 in.) connection behavior obtained from Peterman et al. [83] and introduced in Liu et al. [70] walls,
- 1.37 mm CFS to 11.11 mm OSB (54 mils to 7/16 in.) fastener data based on the mean (μ) backbone of the 30 identical tests conducted in Section 2.1 and assigned in Hikita [57] wall,
- 1.12 mm CFS to 11.11 mm OSB (44 mils to 7/16 in.) connection behavior adopted via a linear interpolation between available tests of 0.84 mm CFS to

11.11 mm OSB (33 mils to 7/16 in.) and 1.37 mm CFS to 11.11 mm OSB (54 mils to 7/16 in.) from Peterman et al. [83] and introduced in Branston [18] walls, and

- 1.09 mm CFS to 9.525 mm OSB (43 mils to 3/8 in.) connection data obtained from an approximated fastener capacity reduction factor of the thickness difference between 9.525 mm (3/8 in.) and 11.11 mm (7/16 in.) OSB sheathings and assigned in Blais [15] walls.

Besides their experimental-derived behavior, the orientation of CFS-to-OSB simulated connections need to be addressed via connection local coordinate systems. As illustrated in Fig. 2.6a the connection vector forces are not aligned with any of the global coordinate system axes, and thus individual connection local coordinate systems are introduced to provide accurate shear wall results and failure modes. For this purpose, a two-stage analysis is introduced:

- At Stage A, a rotation angle θ is calculated based on the connection force in z-direction and the connection force in x-direction, as depicted in Fig. 2.6a. To obtain the rotation angle and subsequently local connection coordinate systems, a linear elastic analysis is conducted at this stage by eliminating any geometric and connection nonlinearities, as well as CFS member plasticity.

- At Stage B, a local coordinate system is introduced to each individual connection by rotating the global coordinate system about the out-of-plane y-direction. This prevents the potential connection capacity overestimation due to axis misalignment. A final pushover analysis is conducted at this stage, by including material plasticity, and connection and geometric nonlinearities, to obtain wall strength, stiffness and failure mode results.

Table 2.5: Four-point backbone of monotonic CFS-to-OSB connection behavior (symmetric response in tension and compression). The load-displacement (P_i-Δ_i) connection response is chosen based on the different examined CFS to OSB thicknesses.

CFS to OSB thickness pattern	P_1 (kN)	P_2 (kN)	P_3 (kN)	P_4 (kN)	Δ_1 (mm)	Δ_2 (mm)	Δ_3 (mm)	Δ_4 (mm)
1.37mm to 11.11mm [1]	0.879	1.742	2.178	0.653	0.576	3.301	6.846	10.76
1.37mm to 11.11mm [2]	0.814	1.627	2.034	0.610	0.540	2.400	5.400	11.60
1.12mm to 11.11mm	0.802	1.605	2.006	0.602	0.735	3.239	6.477	12.16
1.09mm to 9.525mm	0.682	1.364	1.705	0.512	0.735	3.239	6.477	12.16

1 Experimentally-determined by Peterman et al. [83]

2 Experimentally-determined via 30 tests in this study

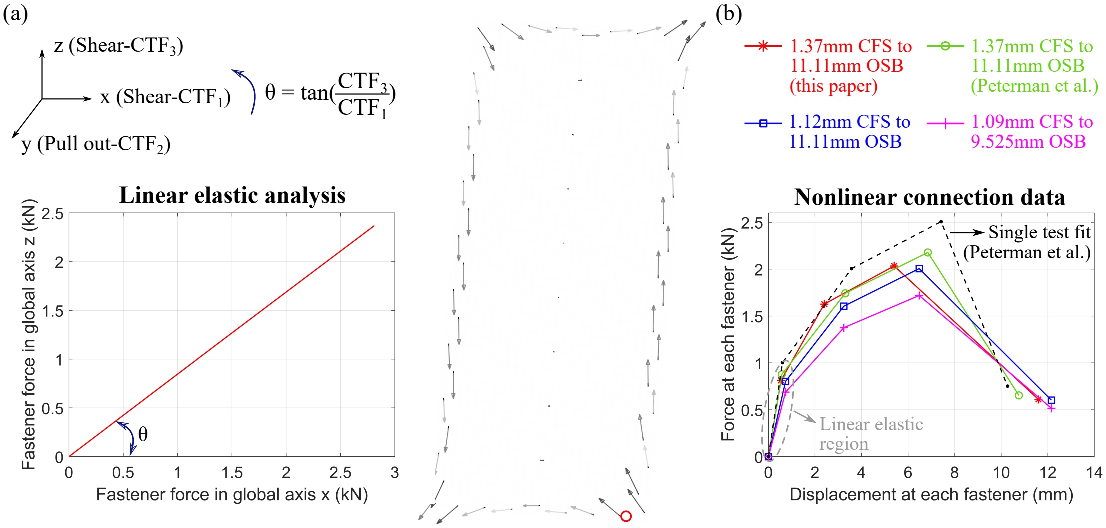

Figure 2.6: CFS-to-OSB connection data and simulation method (two-stage approach). (a) Connection vector forces of a prior linear elastic analysis, and individual screw local coordinate system calculation. A rotation angle θ is calculated as the total connection force at z-axis (CTF_3) over the total connection force at x axis (CTF_1), leading to the rotation of the global coordinate system about the out-of-plate y-axis (Direction 2). (b) Nonlinear average connection data used for all different simulated walls. The solid lines indicate the fastener response used to validate the FE approach, while the dashed lines is used in the parametric analysis.

The pull-out CFS-to-OSB connection behavior is simulated via a high stiffness of 1750 kN/mm (10000 kips/in.) to prevent any significant OSB out-of-plane movement. Connection pull-out stiffness is further examined in this study in Subsection 2.3.2.

2.2.5 Hold-down simulation and boundary conditions

Hold-downs are used at the bottom part of all examined shear walls to withstand the overturning moment under lateral loading. A rigid body is simulated at the bottom part of the chord stud webs, whose reference point (RP) in the middle is connected to the foundation by a linear spring element fixed in the vertical z-direction (Spring2 from ABAQUS library), as illustrated in Fig. 2.5f. The Spring2 stiffness is obtained based on the hold-down type in combination to attached chord stud thickness (taken from the manufacturer specifications based on ASD calculations), as follows:

- For Liu et al. [70] walls, Simpson Strong-Tie S/HDU6 hold-down type is attached to 1.37 mm (54 mils) thick CFS chord studs. The hold-down tensile stiffness is equal to 2929 kN/m (56.7 kips/in.), while the compressive stiffness is 1000 times higher than the tensile stiffness, as adopted by Leng et al. [67].

- For McGill effort walls, Simpson Strong-Tie S/HD10 hold-down type is connected to 1.12 mm (44 mils) or 1.09 mm (43 mils) thick CFS studs (Branston [18] and Blais [15]) and to 1.37 mm (54 mils) thick studs (Hikita [57]). The stiffness in tension is equal to 17388 kN/m (99.3 kips/in.) and 22292 kN/m (127.3 kips/in.) respectively. The stiffness in compression is defined as 1000 times higher than the stiffness in tension for both types.

Bottom and top boundary conditions are adopted by the respective simulated OSB-sheathed shear wall experimental studies (Liu et al. [70], Branston [18], Blais [15], Hikita [57]). In all nine examined shear walls, four shear anchors (two of them in hold-down locations) are used in the test program to connect the bottom tracks to the ground. The shear anchors are modeled as pinned nodes by restraining the horizontal (x-direction) and out-of-plane (y-axis) directions, as illustrated in Fig. 2.5h. Top boundary conditions differentiate between the Liu et al. [70] and the McGill work (Branston [18], Blais [15], Hikita [57]) based on the respective test rigs (Fig. 2.5i):

- Two lines of nodes in the top tracks spaced every 76.2 mm (3 in.) are used to restrain the out-of-plane wall motion (y-direction) for Liu et al. [70] shear walls. The selected node pattern is based on the actuator location and the test rig of the experimental study by [70].
- One line of nodes is used in the top track spaced every 230 mm (9 in.) for Branston [18], Blais [15] and Hikita [57] shear walls to restrain the movement of the walls out-of-plane. This pattern is adopted by McGill University's test rig at which six shear anchors (rig bolts) are used in the node locations.

2.2.6 Component interactions and lateral loading

Surface-to-surface contact is selected to represent the CFS structural frame to OSB sheathing interactions. Hard contact is introduced to define the normal behavior between OSB sheathing and CFS studs and tracks. Sheathing is selected as the master surface while CFS members constitute the slave surfaces between these contact pairs, since OSB board is modeled by a coarser mesh than studs and tracks. Tangential contact behavior is not introduced herein, while the impact of friction coefficients between 0.2 and 0.6 in wall response is investigated in Subsection 2.3.2.

Lateral loading is monotonically applied at the top of all the examined OSB-sheathed CFS shear walls through displacement control, as illustrated in Fig. 2.5g. A displacement of 0.127 m (5 in.) and of 0.08 m (3 in.) is chosen for Liu et al. [70] walls and McGill effort (Branston [18], Blais [15], Hikita [57]), respectively. The displacement is applied at a reference point (RP) in the middle of the top track whose edges are simulated as a rigid body tied to the RP. Quasi-static analysis (Newton-

Raphson solver) is used in this work with an initial and a maximum step time equal to 0.01, and a minimum time increment of 10^{-7}. The impact of a smaller initial and maximum time step is evaluated in Subsection 2.3.2.

2.3 Result validation and discussion

The finite element modeling results are validated herein by nine experimental studies. An extensive parametric analysis is also conducted focusing on the reliability of CFS-to-OSB connections and the effect of different modeling parameters in OSB-sheathed CFS shear wall response.

2.3.1 Experimental validation of finite element model

The introduced modeling approach is benchmarked for strength, stiffness and failure mechanisms using existing experimental data. Specifically, wall peak load, initial stiffness, secant stiffness, and dominant wall failures are discussed.

2.3.1.1 Force-displacement behavior

Fig. 2.7 illustrates the force-displacement behavior of all nine simulated walls (red-colored lines) and its comparison with the response of the respective experiments (blue-colored lines) from Liu et al. [70], Branston [18], Blais [15] and Hikita [57]. Wall peak load is accurately predicted within 5% for eight of the nine shear walls, and within 11% for one of the walls. Wall capacities and the percentage differences between simulations and tests are summarized in Table 2.6. Computational displacement at each wall peak strength is captured within 5% in comparison to the three tests from Branston [18] and the three tests from Blais [15]), while a percentage discrepancy of 23% appears in comparison to the two wall tests from Liu et al.

[70] and the wall test from Hikita [57]). As shown in Fig. 2.7, six of the adopted shear wall experiments include three repetitions of the same test (Experiment No. 1, Experiment No. 2, Experiment No. 3) illustrating the variable wall response up to 11% between identical tests in terms of capacity and displacement at peak strength. Wall variability is also addressed in Subsection 2.3.2 via a parametric analysis, while post-peak behavior is out of the scope of this research.

The introduced finite element modeling approach, as shown in Fig. 2.7, is also able to capture the peak strength decrease and stiffness increase as the perimeter fastener spacing increases from 76.2 mm (3 in.) to 101.6 mm (4 in.) and to 152.4 mm (6 in.), and as wall aspect ratio increases (smaller wall width).

Table 2.6: Shear wall capacity comparisons between experiments, finite element (FE) models and AISI-S400-15 design predictions. Capacity overprediction is indicated by (+), and capacity underprediction by (−). Wall strength is captured within 11% in all of the simulated wall specimens.

CFS Shear Wall Database (Test No.)	Experimental Work (kN)	FE Model (kN)	Model Difference* (%)	AISI-S400 Code (kN)	Code Difference* (%)
Liu et al. 2014 (1c)	21.80	19.44	−11.9	14.87	−31.8
Liu et. al 2014 (11c)	38.73	38.17	−2.19	33.45	−13.6
Hikita 2006 (51b)	28.18	29.64	+5.18	22.92	−18.7
Branston 2004 (21abc)	16.36	17.01	+3.97	12.07	−26.2
Branston 2004 (23abc)	24.78	25.07	+1.17	17.80	−28.2
Branston 2004 (25abc)	30.09	31.28	+3.95	22.92	−23.8
Blais 2006 (41abc)	14.63	14.64	+0.07	11.70	−20.0
Blais 2006 (43abc)	21.59	21.39	−0.93	17.43	−19.3
Blais 2006 (45abc)	28.93	27.82	−3.84	22.19	−23.3
Overall:			3.69		22.8
COV:			1.11		4.37

$*$ In comparison with test results

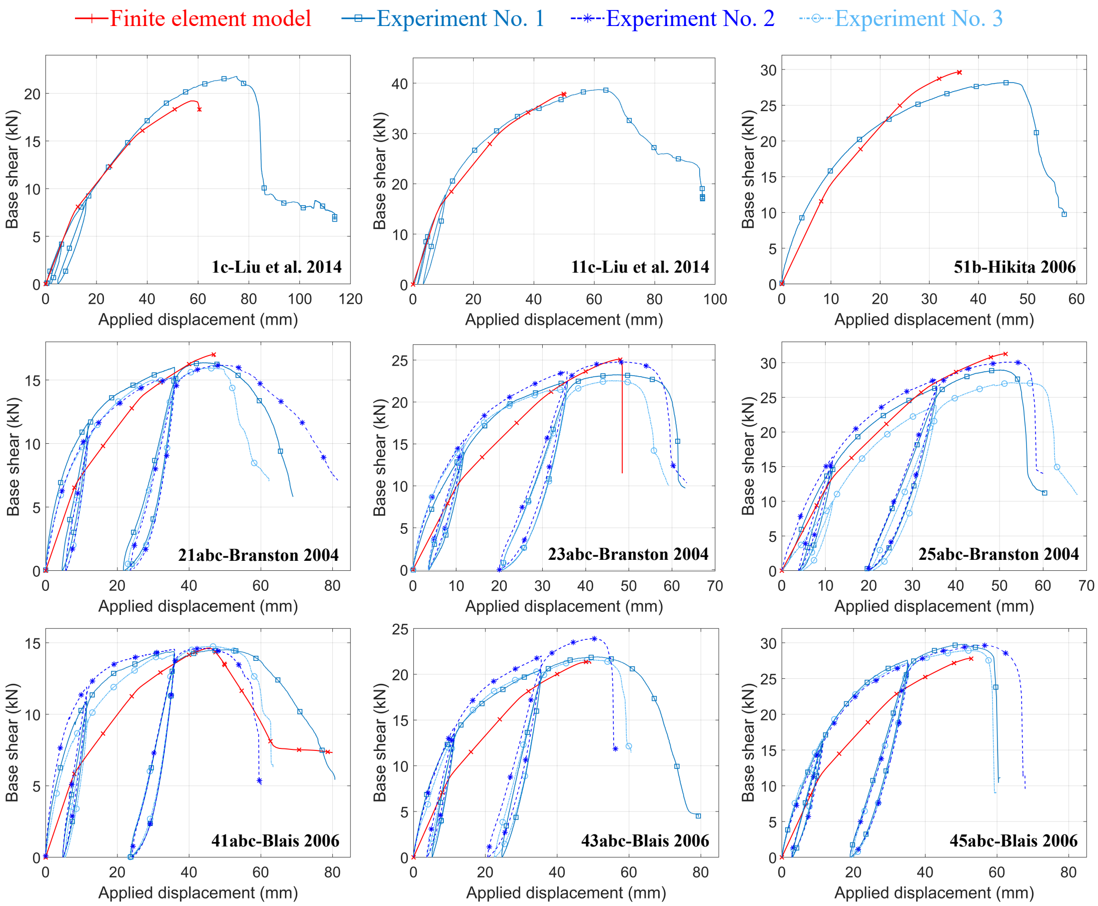

Figure 2.7: Force-displacement finite element behavior of the examined nine shear wall configurations in comparison with the respective available experimental response. The experiment numbers in the legend indicate the repetition number of each test, while the identifier of each test program used to validate the finite element approach is indicated in the lower right part of all graphs. These graphs are intended to be used for strength and stiffness comparisons between computational and experimental results.

2.3.1.2 Initial and secant stiffness

OSB-sheathed CFS shear wall pre-preak stiffness is characterized by its tangent and secant response stiffness, as shown in Fig. 2.8. Fig. 2.8a illustrates a load-displacement graph that indicates the selected three stiffness regions denoted as initial stiffness ($K_{initial}$) from 0% to 40% model peak load (region OA), middle stiffness

(K_{middle}) from 40% to 80% model peak load (region AB), and final stiffness (K_{final}) from 80% to 100% model peak load (region BC). The respective finite element stiffness results normalized by the experimental stiffness results ($K_{model}/K_{experiment}$) are shown in Fig. 2.8b against the nine examined OSB-sheathed CFS shear walls. Tangent stiffness is accurately predicted when CFS-to-OSB behavior is informed with available experimental data from the same test program and rig and by using identical test components (as in [70]) or when the CFS-to-OSB connection data are obtained from the same OSB and CFS member thicknesses (as in [57]). Higher stiffness discrepancies are predicted when CFS-to-OSB connections are obtained by CFS thickness interpolation (as in [18]) or both CFS and OSB thicknesses interpolation (as in [15]). The significance of experimentally derived CFS-to-OSB connection response is further discussed in Subsection 2.3.2.

Secant stiffness (K_{secant}), as described from the load-displacement graph between 0% to 100% model peak load (region OC) in Fig. 2.8c and as illustrated via stiffness ratios ($K_{model}/K_{experiment}$) in Fig. 2.8d, is accurately captured in comparison to the respective tested walls.

2.3.1.3 Failure modes

Local connection coordinate systems, as obtained from a prior linear elastic analysis, are illustrated in Fig. 2.9a (specimen 1c from Liu et al. [70] is demonstrated for result representation). The resultant connection vector forces are in alignment with the local coordinate systems and their angles remain constant until wall peak load. The angles might change slightly post-peak load for some of the vector forces.

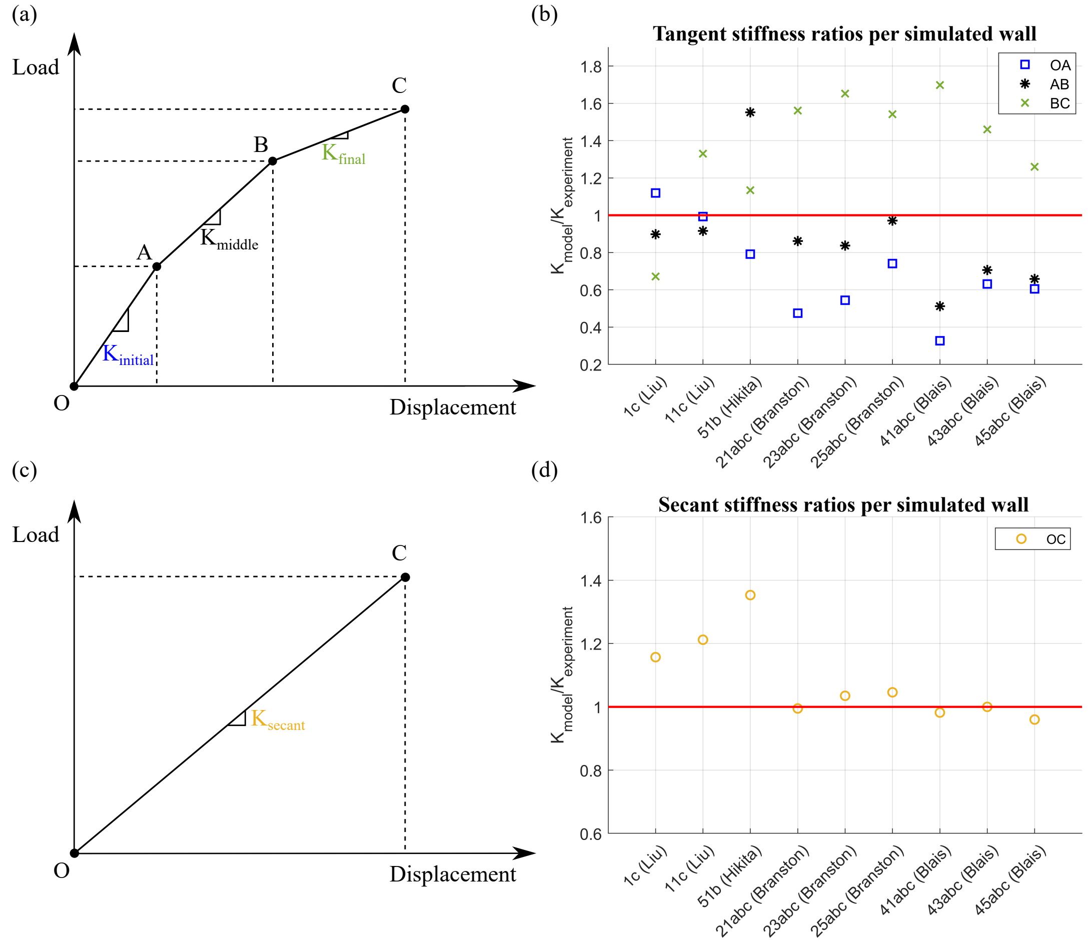

Figure 2.8: Finite element stiffness evaluation of OSB-sheathed CFS shear walls in comparison to experimental stiffness results. Tangent stiffness is calculated based on (a) a typical load-displacement curve indicating the three different stiffness regions pre-peak as initial ($K_{initial}$), middle (K_{middle}) and final (K_{final}), and (b) the respective stiffness ratios against all simulated walls. Secant stiffness is calculated based on (c) a typical load-displacement curve indicating one region pre-peak as secant (K_{secant}) and (b) the respective stiffness ratios for each examined test specimen.

The dominant failure mode in OSB-sheathed CFS shear wall response, as reported in previous experimental studies, is the pull-through or shear failure of CFS-to-OSB screws followed by OSB tear out or bearing. The finite element modeling approach in this work accurately captures the CFS-to-OSB governing connection failures in agreement with the respective tests. Connection failures are progressively distributed between the connections along the length of studs and tracks initiated from the right bottom wall corner, and propagated to the left corner and lastly to the top wall corners. Fig. 2.9c depicts the progression of connection failure in the right bottom wall part (described with symbols in Fig. 2.9a). Corner fasteners are the most critical since they fail first transferring the load and the failure to each immediate adjacent fastener until the global wall failure when most of the connections have reached their capacity (indicated with the dashed line in Fig. 2.9c).

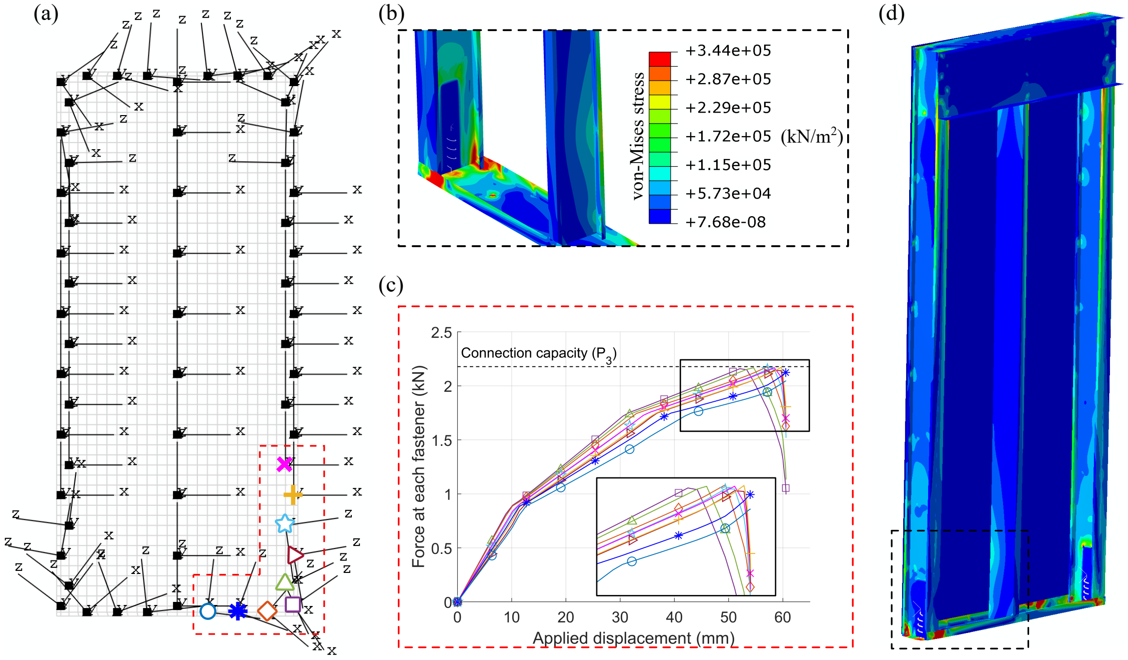

Figure 2.9: Failure mechanisms and finite element result post-processing. (a) Representation of shear wall local connection coordinate system. (b) Von-mises stresses (zoom-in) at bottom track at failure. (c) Connection progression of failure in the lower right part of the shear wall (markers are used). (d) Shear wall deformation (von-Mises stress) indicating high stress concentration near stud-to-track connections.

Shear wall deformed shape and von-Mises stresses for section point 1 (until yielding) are depicted in Fig. 2.9d and in the exploded view in Fig. 2.9b. High stresses are observed close to the connections between CFS studs and tracks, while smaller stresses are predicted in the OSB sheathing (rotates as a rectangle during loading).

2.3.2 Parametric analysis

This section investigates the sensitivity or insensitivity of the introduced finite element modeling assumptions and parameters, such as the simulation of connections, boundary conditions, OSB sheathing, contact, mesh, hold-downs, material properties and time increment. The impact of these parameters in the wall peak strength is the focus herein, as suggested by the AISI-S400 [5] design capacity predictions.

2.3.2.1 CFS-to-OSB connection reliability analysis

The impact of CFS-to-OSB connection predicted variability in OSB-sheathed CFS shear wall full response is explored herein. The finite element shear wall behavior is examined by using three different experimentally-derived CFS-to-OSB connection data in the shear wall computational modeling. The 1.22 m x 2.74 m (4 ft x 9 ft) shear wall by Liu et al. [70] is selected for representation of the results, since the components in the shear wall experiment are identical to the components in the connection tests by Peterman et al. [83]. The test results in Section 2.1 of this work refer to the same component thicknesses and screw type as [70], but are taken from a different batch. For this reason, the wall's nonlinear CFS-to-OSB connection behavior is adopted from:

- Peterman et al. [83] by using the average response of the tested specimens (shown with a circle-marker solid line in Fig. 2.6b),
- Peterman et al. [83] by using a fit to data of a single test of the highest capacity (indicated with a dot-marker dashed line in Fig. 2.6b), and
- Section 2.1 of this current work by using the statistical experimental mean μ (depicted with a star-marker solid line in Fig. 2.6b).

The CFS shear wall computational force-displacement response is illustrated in Fig. 2.10a, Fig. 2.10b, Fig. 2.10c for the three different connection data respectively in comparison to test behavior. The results demonstrate that although connection data are all obtained from the same OSB and CFS members and screws, a 16% wall capacity variability is predicted between the different computational results. This highlights the significant sensitivity of the OSB-sheathed CFS shear wall modeling approach by the CFS-to-OSB connections, and recommends the use of experimental connection data using components from the same batch with each respective wall.

To further characterize the connection variability effect in shear wall behavior, the $\mu\pm\sigma$ and $\mu\pm2\sigma$ connection lower and upper bounds of the 30 identical tests in Section 2.1 are used in the Liu et al. [70] shear wall model. The finite element modeling results illustrated in Fig. 2.10d demonstrate a peak strength variance of ±12% for introduced connection data within one standard deviation (σ), and capacity variance of ±25% for connection behavior within two standard deviations. The potential intermediate wall behaviors are enclosed by the bounds and are indicated with shaded areas in Fig. 2.10d. These results conclude the sensitivity of the introduced fastener-based modeling approach to CFS-to-OSB connection response.

2.3.2.2 Modeling insensitivity parameters

The impact of various modeling parameters and assumptions to the introduced finite element modeling approach is described herein via a parametric analysis with regards to shear wall peak strength (specimen 1c from Liu et al. [70]). Table 2.7 summarizes the examined parameters and provides their respective percentage differences in comparison to the mean computational wall capacity indicated with a red-colored line in Fig. 2.10d. The effect of each parameter is evaluated herein by altering an individual parameter at each simulation while maintaining all the remaining assumptions as described in Section 2.2. Positive (+) and negative (−) signs in Table 2.7 indicate capacity increase and decrease when compared to the mean computational wall capacity respectively, while (±) indicates both decrease and increase in the examined parameter variation range.

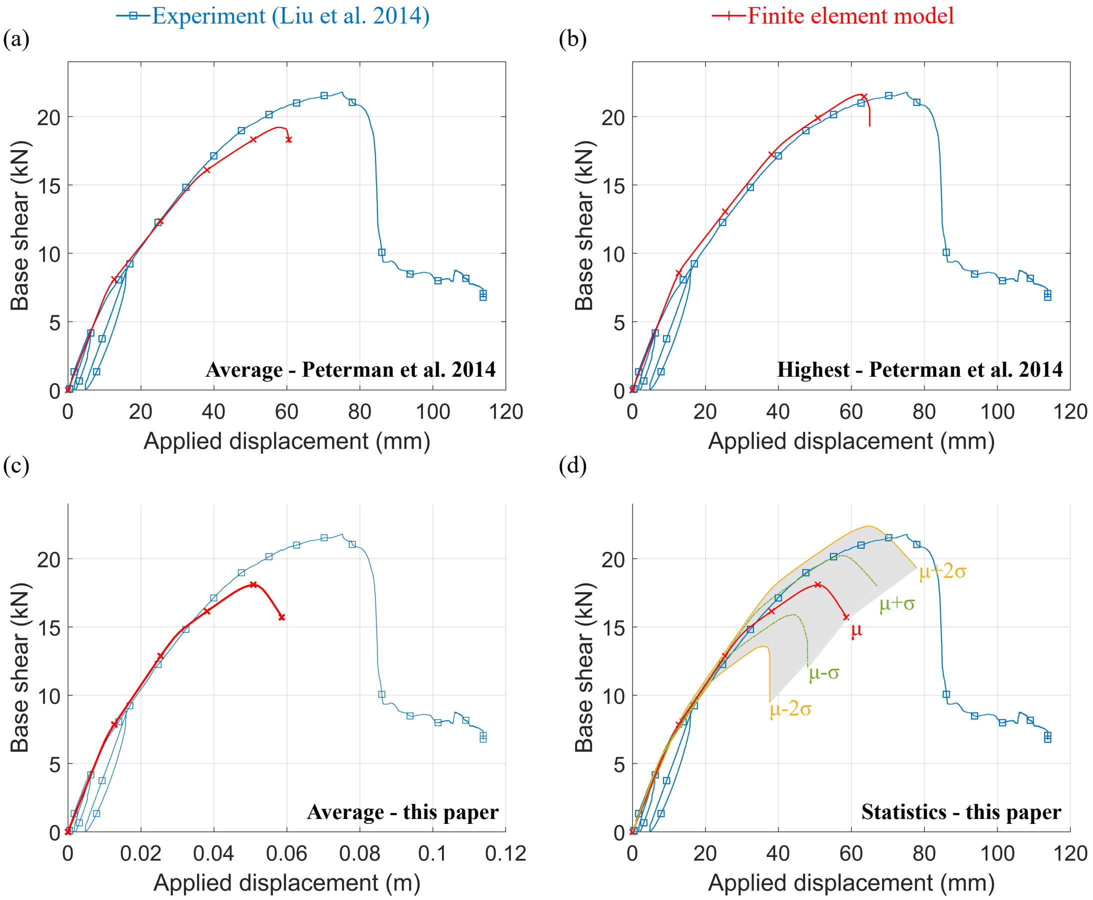

Figure 2.10: OSB-sheathed CFS shear wall lateral performance accounting for connection variability (test 1c from Liu et al. [70] for representation). Different data of 1.37 mm CFS to 11.11 mm OSB connections are adopted from (a) Peterman et al. [83] using the average test behavior, (b) Peterman et al. [83] using the highest strength test behavior, and (c) this current study using the average response of the 30 tests. (d) Shear wall response enclosed by the higher and lower response bounds using the $\mu \pm \sigma$ and $\mu \pm 2\sigma$ connection statistical data of the 30 tests is shown.

The modeling assumptions and parameters investigated in this study and summarized in Table 2.7 vary by the use of:

- a global coordinate system for all CFS-to-OSB connections in comparison to the individual connection local coordinate systems,
- a reduced stiffness varied between 0% to 100% of the initial CFS-to-OSB connection stiffness in local z-axis in comparison to same nonlinear behavior in both shear directions,
- a tangential contact definition varying the friction coefficient between 0.2 and 0.6 in addition to the normal hard contact definition,
- connector elements Cartesian to simulate CFS-to-CFS connections (stud-to-track) in comparison with MPC pinned constraints choice,
- measured material properties of CFS profiles (yield strength and stiffness) compared to nominal dimensions,
- an additional rigid body simulation of the hold-downs at track webs in comparison with rigid body hold-down simulation at chord stud webs,
- an additional contact definition between CFS-to-CFS members by also varying the friction coefficient between 0.2 and 0.8,
- a reduced pull-out connection stiffness varied from 1506 kN/m (9 kips/in.) up to the selected pull-out stiffness of 1750000 kN/m (10000 kips/in.),
- isotropic and/or plastic OSB sheathing modeling compared to elastic orthotropic material properties,
- a smaller mesh size of 38.1 mm (1.5 in.) compared to the 50.8 mm (2 in.) of OSB sheathing,

- fixed boundary conditions in the locations of the shear anchors or pinned shear anchors excluding the boundary conditions in hold-down location anchors in comparison with all pinned bottom track boundary conditions,
- shear modulus varied from the selected 1316 MPa (191 ksi) to 10000 MPa (1450 ksi),
- a maximum and initial time increment of 0.001 in comparison with the selected time step of 0.01, and
- a hold-down stiffness altered between LRFD prediction of 7734 kN/m (41.8 kips/in.) and 17388 kN/m (99.3 kips/in.) compared to the selected ASD prediction of 2929 kN/m (56.7 kips/in.).

Table 2.7: Impact of modeling assumptions and parameters on the capacity of OSB-sheathed CFS shear walls. The introduced computational model is mainly sensitive to CFS-to-OSB connection response.

Sensitivity/insensitivity parameters	Impact sign	Peak load impact
CFS-to-OSB shear connection behavior	(±)	25%
Global connection coordinate system	(+)	4.9%
CFS-to-OSB shear stiffness in perpendicular local axis	(−)	2 − 4.4%
CFS-to-OSB contact friction coefficient	(+)	1.3 − 3.7%
Stud-to-track connection Cartesian modeling	(−)	3.5%
CFS measured material properties	(+)	1.8%
Hold-down additional track rigid body modeling	(+)	1.3%
CFS-to-CFS contact friction coefficient	(−)	0.4 − 1%
CFS-to-OSB pull-out connection behavior	(−)	0.001 − 0.61%
OSB sheathing modeling	(+)	0 − 0.59%
OSB mesh discretization	(+)	0.57%
Shear anchor modeling (BCs)	(+)	0.02 − 0.19%
OSB sheathing shear modulus	(+)	0.03 − 0.09%
Initial and minimum time increment	(+)	0.04%
Hold-down stiffness	(±)	0.01 − 0.02%

The peak strength impact of all these examined modeling parameters, as shown in Table 2.7, is predicted less than 5% in comparison with the finite element wall response using the mean connection behavior of the 30 identical tests. This study further validates the proposed modeling approach, and suggests that the introduced finite element method for OSB-sheathed CFS shear walls is not largely affected by any parameter explored herein, and is primarily and foremost affected by the CFS-to-OSB connection behavior. The examined variables do not also affect the shear wall initial stiffness (Region OA in Fig. 2.8a), besides the hold-down stiffness and OSB shear modulus variations, which both lead to a stiffness increase up to 19%.

2.3.3 Comparison with AISI-S400 design predictions

OSB-sheathed CFS shear wall AISI-S400 [5] design predictions underestimate the shear wall capacity up to 32% in comparison to previous experimental studies (Table 2.7). This current work also verifies the underprediction of design wall capacities through the introduced finite element modeling approach. Since OSB-sheathed CFS shear walls are highly sensitive to connection response, more shear wall test repetitions are necessary for recalibration of the design predictions.

2.4 Probabilistic approach

This section aims to investigate the stochastic response of OSB-sheathed CFS shear walls through random shear fastener characterization and subsequently through shear wall Monte Carlo (MC) simulations. The approach (similarly to Bian et al. [13]) is based on random fastener response distribution throughout the shear wall for deterministic finite element analyses. The 1.22 m x 2.74 m (4 ft x 9 ft) shear wall configuration (specimen 1c from Liu et al. [70]) is adopted for representation, and is additionally modified to provide results not only for 152.4 mm (6 in.) fastener spacing, but also for 304.8 mm (12 in.) and 609.6 mm (24 in.) fastener spacing, as illustrated in Fig. 2.11.

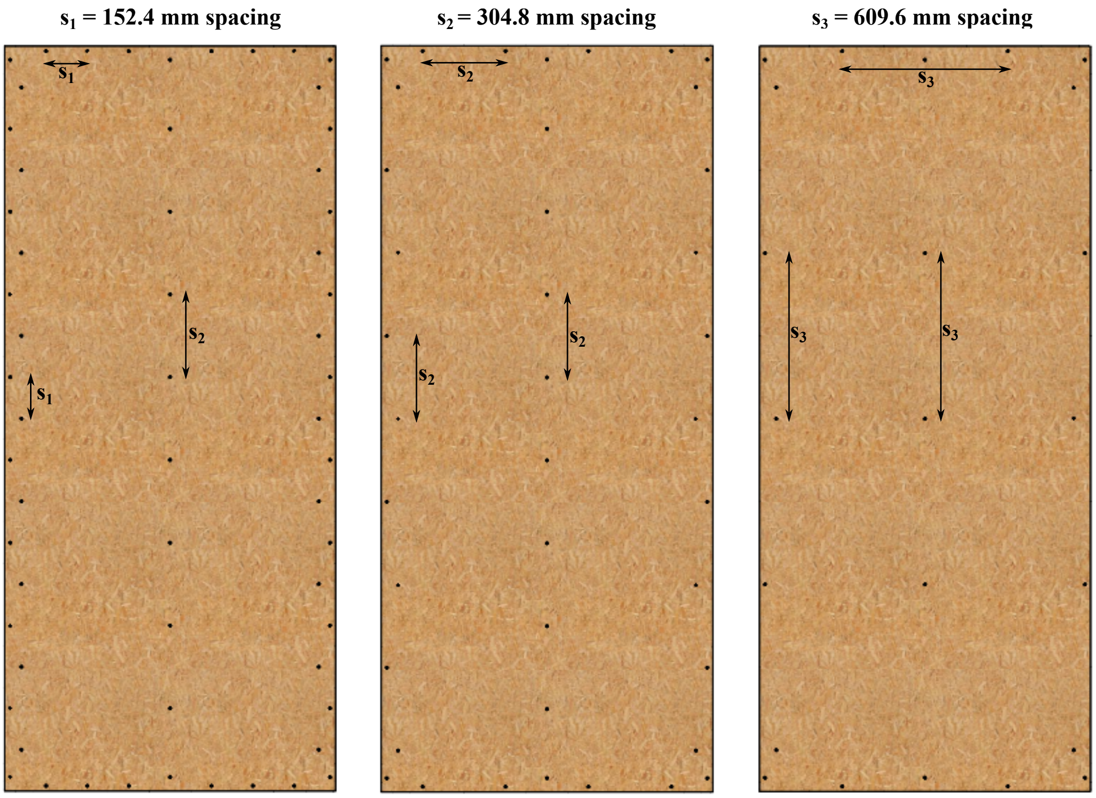

Figure 2.11: Various OSB-sheathed CFS shear walls of different fastener spacings for stochastic response evaluation. Specimen 1c from Liu et al. [70] is used for representation, and fastener spacings of s_1=152.4 mm, s_2=304.8 mm and s_3=609.6 mm are illustrated. The perimeter and field stud fastener spacings vary between the different examined configurations, while all remaining wall characteristics are maintained the same.

2.4.1 Random CFS-to-OSB connection response

Randomness in the structural system is introduced by using the fastener peak load as a random variable. The mean connection capacity (P_3) obtained from the 30 identical tests in Section 2.1 is used as the only random variable, and all remaining response (backbone) parameters are perfectly correlated with peak strength. The statistical characterization of CFS-to-OSB connections, as summarized in Table 2.1, results to a coefficient of variation ($COV{=}\sigma/\mu$) of 12.10% for P_3. Lognormal distribution is adopted for P_3, and a four-point fastener backbone is defined as P_1=40%P_3, P_2=80%P_3 and P_4=30%P_3 (constant post-peak P_4), as discussed in Bian et al. [13]. Stiffness remains constant and equal to the stiffness of the mean (μ) fastener behavior for each branch of the backbone (K_1, K_2, K_3, K_4), and thus displacement (Δ_1, Δ_2, Δ_3, Δ_4) is calculated using Eq. 6, Eq. 7, Eq. 8 and Eq. 9 for each point of the four-point backbone.

$$\Delta_1 = \frac{P_1}{K_1}\ . \tag{6}$$

$$\Delta_2 = \Delta_1 + \frac{P_2 - P_1}{K_2}\ . \tag{7}$$

$$\Delta_3 = \Delta_2 + \frac{P_3 - P_2}{K_3}\ . \tag{8}$$

$$\Delta_4 = \Delta_3 + \frac{P_4 - P_3}{K_4}\ . \tag{9}$$

Fig. 2.12 depicts the generated random connection data, along with the deterministic four-point mean connection response μ_{det}. The resultant random fastener behavior is obtained within and beyond the bounds of the deterministic $\mu \pm \sigma$ and $\mu \pm 2\sigma$ bounds. Since the impact of fastener spacing in the stochastic wall response is examined in this work, the number of generated random data is equal to the number of the CFS-to-OSB connections of each of the simulated shear walls.

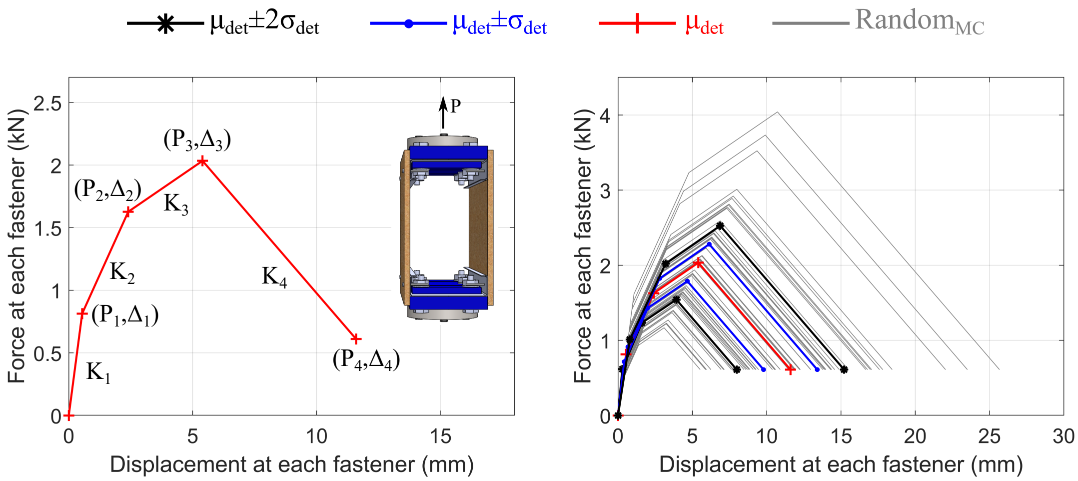

Figure 2.12: Random CFS-to-OSB fastener behavior based on the statistical characterization of the 30 tests. The average four-point mean (μ_{det}) connection response is illustrating including the force (P_i), displacement (Δ_i) and stiffness (K_i) symbols to describe each point. Random connection data are generated based on a single random variable P_3 and by maintaining stiffness constant for all generated data. Random fastener response is not always enclosed between the deterministic $\mu \pm \sigma$ and $\mu \pm 2\sigma$ bounds.

2.4.2 Monte Carlo simulations of OSB-sheathed shear walls

To further investigate the connection variability effect on shear wall system behavior, a probabilistic approach is used herein. Monte Carlo simulations are probabilistic methods that account for the uncertainty of a system behavior through random variable generation. Monte Carlo simulations are conducted, herein, through the deterministic fastener-based finite element modeling approach introduced in Section 2.2, accounting for random fastener distribution. The impact of system randomness in wall performance with 152.4 mm (6 in.), 304.8 mm (12 in.) and 609.6 mm (24 in.) fastener spacings is investigated through in total 90 simulations (30 Monte Carlo (MC) simulations for each configuration is selected). The selection of 30 simulations for each configuration is made based on convergence of their peak strength standard deviation σ_{MC}. For each individual MC simulation, a different set of random fasteners is generated and distributed throughout the wall CFS-to-OSB fasteners. The MC results are illustrated in Fig. 2.13, along with the deterministic wall response (μ_{det}), and the bounds of the deterministic $\mu \pm \sigma$ and $\mu \pm 2\sigma$ for all examined fastener spacings.

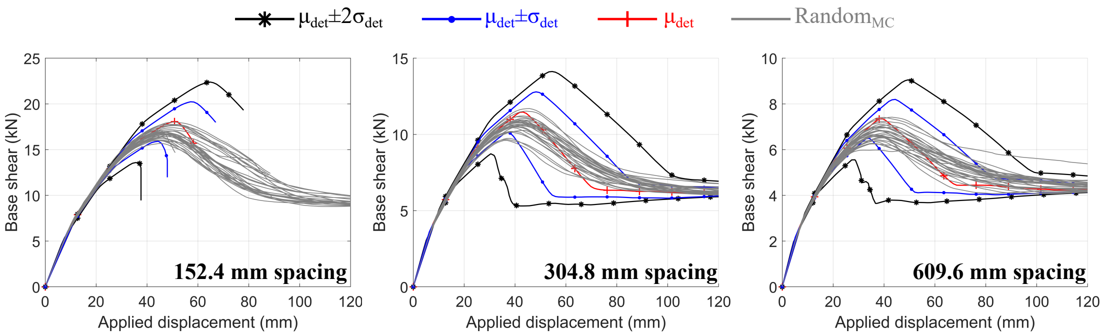

Figure 2.13: Monte Carlo stochastic response of OSB-sheathed CFS shear walls for three different spacings (identifier in lower right part of the graphs). Shear wall response is governed by less variability in comparison to the significant connection variability. The mean deterministic behavior is slightly higher than the mean random behavior in all cases, while capacity decreases as fastener spacing increases. These graphs are intended for comparisons of their statistical results for the three different wall fastener spacings.

The results illustrate that although significant variability governs the CFS-to-OSB fastener behavior (COV=12%), CFS shear wall behavior is governed by less variable response (COV less than 5%) for all fastener spacings. Furthermore, the mean behavior obtained from the Monte Carlo simulations (μ_{MC}) is always lower than the deterministic mean response (μ_{det}), which indicates a series system where the peak strength is negatively affected by the system response. MC-to-deterministic mean ratio is lower than 0.93 for all examined cases. The coefficients of variation COV and the MC-to-deterministic mean ratios μ_{MC}/μ_{det} are summarized in Table 2.8.

A comparison between the different fastener spacings in shear wall response is also conducted herein. As fastener spacing increases from 152.4 mm (6 in.) to 609.6 mm (24 in.), fewer fasteners are used to connect OSB sheathing to CFS members, and as a result the shear wall strength decreases. Furthermore, COV increases with fastener spacing increase (Table 2.8), demonstrating the higher variability that exists for fewer CFS-to-OSB connections in the perimeter and field stud. On the other, the MC-to-deterministic mean ratio is decreased with fastener spacing increase, displaying higher capacity difference between MC and deterministic simulations for smaller fastener spacings.

Table 2.8: Statistical parameters of Monte Carlo simulations in comparison to deterministic models for three different shear wall fastener spacings.

Shear wall spacing	μ_{det} (kN)	μ_{MC} (kN)	σ_{MC} (kN)	COV_{MC} (%)	μ_{MC}/μ_{det} $(-)$
152.4 mm	18.07	16.81	0.586	3.486	0.930
304.8 mm	11.46	10.65	0.477	4.481	0.929
609.6 mm	7.360	6.753	0.345	5.107	0.918

These results conclude that deterministic methods slightly underpredict OSB-sheathed CFS shear wall capacity in comparison to MC analyses. This work is intended to be used for new AISI-S400 [5] design recommendations for CFS shear walls sheathed with OSB, and specifically to introduce a more accurate resistance factor ϕ than the current conservative ϕ=0.6.

3 DESIGN GUIDELINES FOR COLD-FORMED STEEL SHEAR WALLS SHEATHED WITH FIBER CEMENT BOARD AND STEEL-GYPSUM COMPOSITE BOARD

Chapter overview: This chapter assesses the behavior of cold-formed steel (CFS) shear walls sheathed with high capacity fiber cement board (FCB) and steel-gypsum (SG) composite board, experimentally evaluates the monotonic and cyclic shear connection behavior, introduces Pinching4 parameters for connections, and recommends design guidelines for high capacity shear walls.

3.1 Shear connection experimental characterization

The shear response of connections for fiber cement board (FCB) sheathing and steel-gypsum (SG) composite sheathing with cold-formed steel members is experimentally evaluated herein. These tests aim to assess and understand the behavior of high capacity sheathings in connection response, as well as to provide fastener data for finite element modeling applications.

3.1.1 Experimental matrix and assembly

The experimental rig, as described in Chapter 2, focuses on the response evaluation of a system of eight fasteners used to connect two toe-to-toe CFS studs with two sheathing panels of FCB or SG. The actual test rig and the stud-screw-sheathing specimens are illustrated in Fig. 3.1. The screws are located in the flanges of CFS studs, while the deformation of the webs of the studs is restrained via steel plates. This test set up is influenced by Green et al. [50] and Winter [113], and is also adopted by Vieira and Schafer [107] and Peterman et al. [83]. The cross-sectional properties and dimensions of all selected materials are summarized in Table 3.1. In total 18 experiments are conducted evaluating two sheathing types and two screw types under monotonic and cyclic loading, as shown in the test matrix in Table 3.2. Nine specimens are subjected to monotonic loading and nine to cyclic loading, including three repetitions of each sheathing-screw configuration (similarly to Tao et al. [106]).

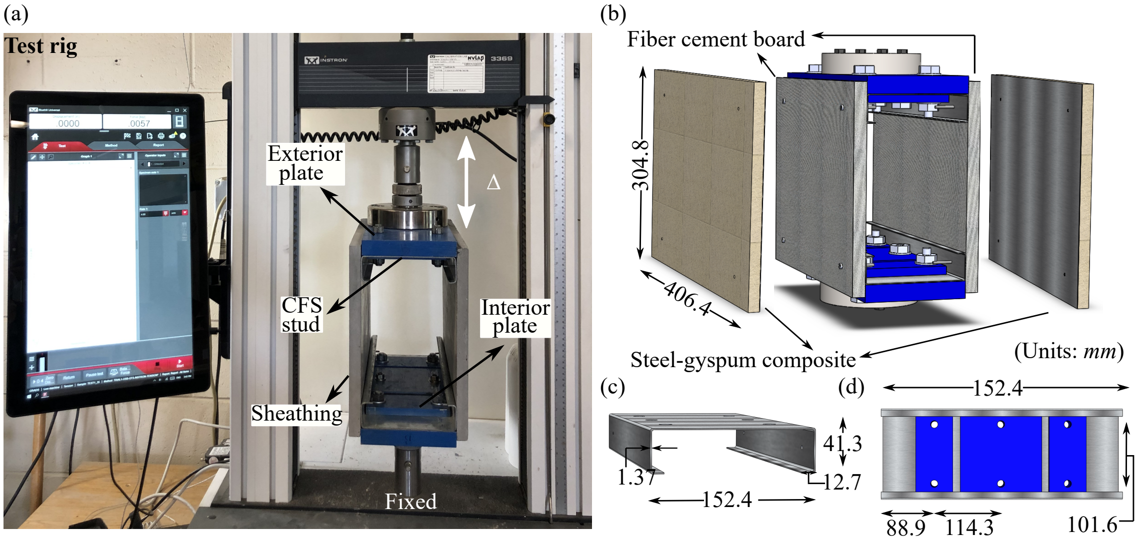

Figure 3.1: CFS-to-FCB and CFS-to-SG connection specimens and test rig. (a) Actual test specimen photo in INSTRON machine, (b) schematic representation of connection specimens of fiber cement board (FCB) or composite steel-gypsum board (SG) sheathing material, (c) cross-sectional dimensions of CFS studs, and (d) inside specimen view including dimensions of steel plates used to restrain stud webs.

Fiber cement board (FCB) of a thickness of 19.05 mm (0.75 in.) and composite steel-gypsum (SG) board of a thickness of 16.59 mm (0.65 in.) are the two sheathing materials selected herein. In the composite SG sheathing, light-gauge steel of a 0.719 mm (0.0283 in.) thickness is adhered to gypsum of a 15.875 mm (5/8 in.) thickness on the exterior board side.

The two investigated self-drilling screw types are an M4 x 50 (No. 8) and an M4 x 40 (No. 8), denoted as screw *a* (taken from the manufacturer) and screw *b* respectively throughout this Chapter (depicted in Fig. A.1b in Appendix A). The diameter of both screw types is the same, while thread length and location, shank length, and drill bit differentiate between the screws. Both screw *a* and screw *b* are examined for the FCB sheathing panel, while the common screw *b* is used for the SG-sheathed specimens. The edge tip of screw *a* is cut to avoid bearing towards the stud webs, as discussed in Chapter 2.

Table 3.1: Component types and cross-sectional dimensions of the experimental connection specimens. Three different sheathing-screw configurations are tested herein (FCB-a, FCB-b, SG-b).

Component	Cross-sectional dimensions (mm)
CFS Studs:	152.4 web, 41.3 flange, 12.7 lip, 1.37 thickness
FCB Sheathing:	304.8 length 406.4 width, 19.05 thickness
SG Sheathing:	304.8 length 406.4 width, 16.59 thickness *
Exterior plates:	406.4 length, 152.4 width, 25.4 thickness
Interior middle plates:	139.7 length, 139.7 width, 12.7 thickness
Interior corner plates:	63.5 length, 139.7 width, 12.7 thickness
Self-drilling screw *a*:	M4 x 50, flat head
Self-drilling screw *b*:	M4 x 40, flat head

$*$ Composite: 0.719mm thick steel adhered to 15.875mm thick gypsum

Screws are located at least 38.1 mm (1.5 in.) from sheathing edges based on AISI-S100-16 [3]. The fastener spacings of 152.4 mm (6 in.) and 304.8 mm (12 in.) are used for the CFS-to-SG specimens (279.4 mm (11 in.) spacing in one specimen), while a constant fastener spacing of 304.8 mm (12 in.) is selected for all CFS-to-FCB sheathed specimens since little connection variability exists between the various fastener spacings.

3.1.2 Test loading

Loading is applied via displacement control at the top of the stud-screw- sheathing specimens, while the bottom part of the specimens is fixed in the test-rig.

3.1.2.1 Monotonic tests

Monotonic tensile loading of a rate of 0.028 mm/hour (0.0011 in./hour) was applied during testing, along with a pre-test load of 45 kN (10 lbs) prior to each experiment. Three monotonic test repetitions were conducted for each sheathing-screw configuration (FCB-a, FCB-b, SG-b) to provide the reference displacements used in the cyclic protocol.

Table 3.2: Test matrix of stud-screw-sheathing connection specimens of different sheathing and screw types, and fastener spacings. In 18 connection specimens are tested under monotonic and cyclic loading.

Loading	Sheathing Type	Screw Type	Screw spacing (mm)	Repetition No.
Monotonic	Fiber Cement Board	a	304.8	R1
			304.8	R2
			304.8	R3
		b	304.8	R1
			304.8	R2
			304.8	R3
	Steel-Gypsum	b	304.8	R1
			152.4	R2
			279.4	R3
Cyclic	Fiber Cement Board	a	304.8	R1
			304.8	R2
			304.8	R3
		b	304.8	R1
			304.8	R2
			304.8	R3
	Steel-Gypsum	b	152.4	R1
			304.8	R2
			152.4	R3

3.1.2.2 Cyclic tests

The CUREE protocol, as described in Krawinkler et al. [65] and widely used in Peterman et al. [83], Fiorino et al. [40], Okasha [79], Fiorino et al. [41] connection tests, and Liu et al. [70], Hoehler et al. [58], Branston et al. [19], DaBreo et al. [27] wall tests, is constructed to apply the cyclic loading herein. The CUREE cyclic loading protocol is constructed for each sheathing-screw specimen (FCB-a, FCB-b, SG-b) by using a reference displacement Δ defined as the 60% of the monotonic displacement at the 80% post-peak load Δ_m (Δ=0.6Δ_m), and is composed of initiation, primary and trailing cycles, as shown in Table 3.3. One cycle every 16 sec (frequency of 0.0625 Hz) is applied during the cyclic loading. The resultant protocol is depicted in Fig. 3.2 as a percentage of Δ, including the reference displacements of all examined specimens configurations (FCB-a, FCB-b, SG-b).

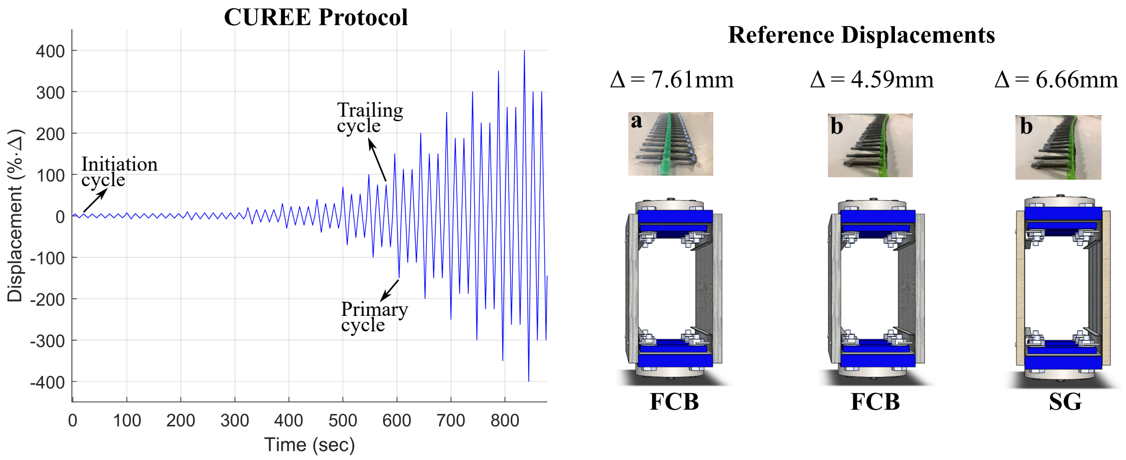

Figure 3.2: CUREE protocol for cyclic loading constructed from initiation, primary and trailing cycles. Displacement is plotted against time as a percentage of reference displacement Δ. The reference displacement of each screw-sheathing configuration (FCB-a, FCB-b, SG-b) is depicted.

Table 3.3: CUREE protocol description for cyclic loading. The CFS-to-sheathing connection specimens are subjected to in total 55 cycles.

Cycle Name	No. of Cycles	Cycle Amplitude
Initiation	6	0.05Δ *
Primary	1	0.075Δ
Trailing	6	0.05625Δ
Primary	1	0.1Δ
Trailing	6	0.075Δ
Primary	1	0.2Δ
Trailing	3	0.15Δ
Primary	1	0.3Δ
Trailing	3	0.225Δ
Primary	1	0.4Δ
Trailing	2	0.3Δ
Primary	1	0.7Δ
Trailing	2	0.525Δ
Primary	1	1.0Δ
Trailing	2	0.75Δ
Primary	1	1.5Δ
Trailing	2	1.125Δ
Primary	1	2.0Δ
Trailing	2	1.5Δ
Primary	1	2.5Δ
Trailing	2	1.875Δ
Primary	1	3.0Δ
Trailing	2	2.25Δ
Primary	1	$3.5.0\Delta$
Trailing	2	2.625Δ
Primary	1	4.0Δ
Trailing	2	3.0Δ

$*$ Δ is the reference displacement

3.1.3 Test results of CFS-to-sheathing connections

System test results of all 18 connection specimens are illustrated in Fig. 3.3. The inset photographs in Fig. 3.3 depict the different failure mechanisms of each sheathing-screw configuration (FCB-a, FCB-b, SG-b) after testing. Full specimen photographs after testing are shown in Fig. A.1c in Appendix A for both FCB and SG sheathings. Strength, stiffness and failure modes are discussed herein. Peak strength (P_{max}), and initial (K_{in} defined at 0-40% peak strength) and secant (K_{sec} defined at 0-100% peak strength) stiffness are summarized in Table 3.4 for all experiments under monotonic and cyclic loading. In general, SG-sheathed specimens result to higher strength and stiffness than FCB-sheathed specimens. Furthermore, monotonic tests of all sheathing-screw specimens demonstrate higher peak strength and lower stiffness compared to the cyclic tests (discussed in Section 3.2).

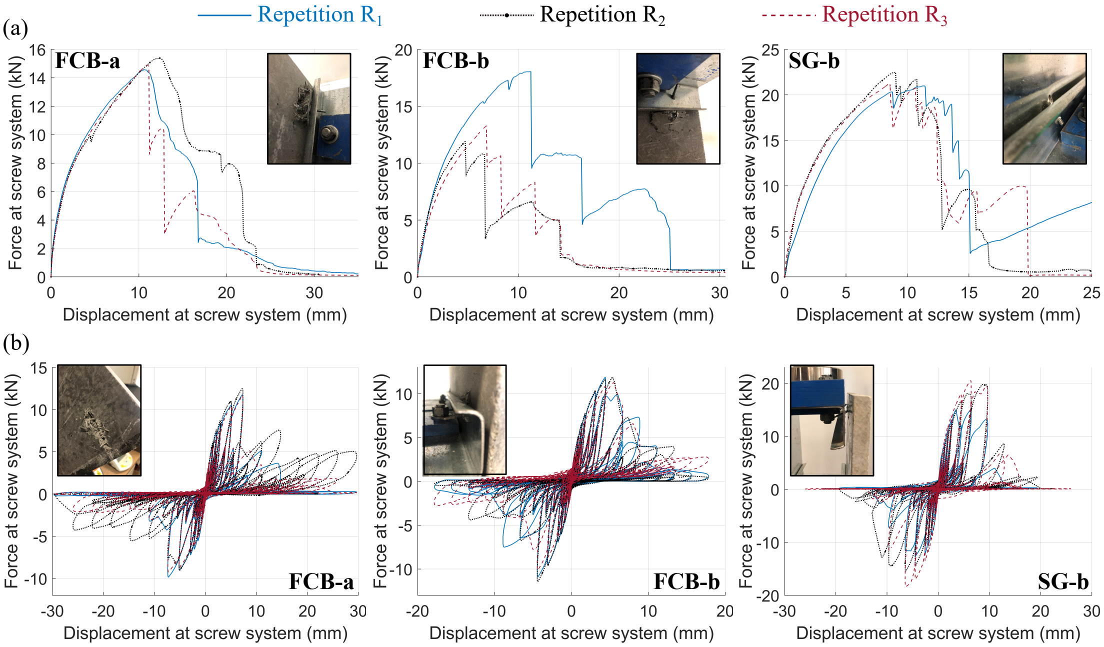

Figure 3.3: System force-displacement test response of in total 18 specimens. (a) Monotonic results (9 specimens) , and (b) cyclic connection results (9 specimens) of each examined sheathing-screw configuration (FCB-a, FCB-b, SG-b). Three identical repetitions of each sheathing-screw configuration are conducted under both monotonic and cyclic loading. Inset photos illustrate the dominant failure mechanisms (either screw pull-through or shear screw failure).

Table 3.4: Summarized test results of the system of eight fasteners. The peak strength P_{max}, and the initial K_{in} and secant K_{sec} stiffness are presented for all 18 experiments under monotonic and cyclic loading.

Monotonic Connection Experiments

Test assembly	Peak strength P_{max} (kN)	Initial stiffness K_{in} (kN/mm)	Secant stiffness K_{sec} (kN/mm)
FCB - a - R_1	14.579	4.596	1.372
FCB - a - R_2	15.383	4.005	1.243
FCB - a - R_3	14.883	4.142	1.366
FCB - b - R_1	18.051	4.749	1.608
FCB - b - R_2	11.920	5.277	2.521
FCB - b - R_3	13.285	4.424	1.947
SG - b - R_1	20.992	4.390	1.846
SG - b - R_2	22.485	6.989	2.491
SG - b - R_3	21.308	7.008	2.485

Cyclic Connection Experiments

Test assembly	Peak strength		Initial stiffness		Secant stiffness	
	${P_{max}}^+$	${P_{max}}^-$	${K_{in}}^+$	${K_{in}}^-$	${K_{sec}}^+$	${K_{sec}}^-$
	(kN)		(kN/mm)		(kN/mm)	
FCB - a - R_1	12.369	– 10.318	4.442	4.700	1.625	1.354
FCB - a - R_2	13.090	– 9.5116	4.601	3.787	1.719	1.783
FCB - a - R_3	12.356	– 9.7672	4.188	4.637	1.622	1.282
FCB - b - R_1	12.428	– 11.438	5.966	5.630	2.702	2.488
FCB - b - R_2	12.691	– 12.022	6.045	5.429	2.219	2.614
FCB - b - R_3	11.825	– 10.584	5.546	5.341	2.019	2.301
SG - b - R_1	15.772	– 13.190	10.22	9.674	2.368	2.826
SG - b - R_2	20.945	– 16.248	6.462	5.951	2.279	2.436
SG - b - R_3	21.353	– 19.104	7.900	8.335	3.201	2.865

3.1.3.1 Monotonic test results

FCB-sheathed connection specimens were governed either by pull-though of the screws or shear failure of the screws under monotonic loading, while SG-sheathed connection specimens were dominated by shear screw failure. Connection specimens governed by pull-through showed higher ductility than assemblies failed due to the abrupt shear failure.

The progression of failure in FCB-a specimens was initiated by screw tilting at the beginning of the tests leading to the pull-through of the fasteners at peak load. The FCB sheathing tear out or bearing, as well as shear failure of some of the remaining screws were present post-peak. Little variability existed in all three FCB-a test repetitions. FCB-b connection specimens were dominated by the initial tilting and shear failure of some of the screws followed by sheathing edge tear out and bearing. One FCB-b test repetition exhibited a variable response, likely due to the presence of one over-driven screw.

In SG-b connection specimens, tilting of the screws occurred at the beginning of the tests leading to the governing shear screw failure, and eventually to the sheathing bearing in both steel and gypsum panels around screw locations. Little behavior variability was predicted between the three identical SG-b test repetitions. Steel and gypsum edge separation was present in two specimens post-peak.

3.1.3.2 Cyclic test results

Both FCB- and SG-sheathed connection specimens were dominated by shear failure of some of the screws under cyclic loading. Slightly lower capacities are predicted in the negative quadrants in comparison to the positive quadrants in all configurations.

FCB-a specimens were governed by shear failure of some of the screws followed by FCB sheathing edge tear out and/or bearing for all test repetitions. Little strength and stiffness variability was predicted between the test repetitions. Higher energy dissipation occurred in one of the FCB-a test repetitions (repetition R_2) at higher drifts post-peak load. Similarly, FCB-b specimen response was governed by shear screw failure accompanied by bearing of the screws at screw locations. Little variability existed in terms of stiffness, strength and energy dissipation between the repetitions. In general, energy dissipation of FCB-b specimens was lower than FCB-a specimens.

In SG-b specimen response, the governing failure mechanism was shear failure of the screws accompanied by localized bearing of steel and gypsum composite sheathing around the locations of the screws. Steel-to-gypsum separation was present post-peak load during some of the repetitions. SG-b specimens exhibited capacity variability in one repetition (repetition R_1), due to an over-driven screw, while fastener spacing did not affect the system connection response.

3.2 Hysteretic characterization of CFS-to-sheathing connections

To provide hysteretic parameters of CFS-to-FCB and CFS-to-SG connections, including backbones and Pinching4 parameters, the system eight-fastener response is converted to individual screw behavior. System load P, system displacement Δ, and system stiffness K are converted into single connection data using the equations derived by Vieira and Schafer [107], as described in Chapter 2. Specifically the load at each screw is calculated as $P_i = P/4$, the individual screw displacement is $\Delta_i = \Delta/2$ and the single screw stiffness is defined as $K_i = K/2$. Single screw results are intended for use in finite element modeling efforts.

3.2.1 Monotonic tests

The average fit to data monotonic connection behavior is obtained via a four-point nonlinear behavior obtained at 40% peak load, 80% load, 100% peak load and 30% post-peak load, as discussed in Chapter 2. Fig. 3.4 illustrates the average fit to data (top graphs) curves of the monotonic results of all FCB-a, FCB-b and SG-b specimens, as obtained by averaging the response of the respective three test repetitions. The mean backbone of each sheathing-screw configuration is summarized in terms of load (ePf_i) and displacement (ePd_i) in Table 3.5 and in terms of stiffness in Table 3.6.

The average connection backbones for monotonic loading allow for quantitative comparisons between the examined sheathing-screw configurations. Average peak connection strength does not largely differ between specimens fastened with screw *a* and specimens fastened with screw *b*. FCB-a specimens outperform FCB-b connection specimens in peak load by 3.66%. Initial stiffness of FCB-b configurations is higher than FCB-a assemblies by 13%. The SG-b average response leads to higher strength and stiffness than the response of FCB-b specimens. SG-sheathed assemblies outperform FCB-a assemblies by 45% in capacity and by 39% in initial stiffness. Similarly, a higher strength of 50% and a higher stiffness of 23% is predicted for SG-b specimens in comparison to FCB-b specimens.

3.2.2 Cyclic tests

To characterize the single screw connection response under cyclic loading, Pinching4 parameters are extracted. Pinching4 model is a uniaxial model generated by Lowes et al. [71] and Altoontash [7] to provide load-displacement response parameters for the re-loading and un-loading behavior of reinforced concrete during cyclic loading. Since CFS fasteners are governed by pinched response, the Pinching4 model has been widely used in Peterman et al. [83] and Tao et al. [106] connection tests and in Liu et al. [70] and Buonopane et al. [20] wall tests, and is adopted herein. Fig. 3.5 depicts the Pinching4 load-displacement model including variables of the symmetric backbone parameters (points A-H), and the symmetric hysteretic parameters (points a-f).

Table 3.5: Four-point average backbones of CFS-to-sheathing connections for monotonic and cyclic tests, and Pinching4 parameters for the cyclic tests. The recommended parameters are symmetric in positive and negative quadrant for all examined FCB-a, FCB-b and SG-b assemblies.

Monotonic Connection Experiments								
	Backbone parameters (mean)*							
Type	ePf$_1$ (kN)	ePf$_2$ (kN)	ePf$_3$ (kN)	ePf$_4$ (kN)	ePd$_1$ (mm)	ePd$_2$ (mm)	ePd$_3$ (mm)	ePd$_4$ (mm)
FCB - a	1.495	2.990	3.737	1.121	0.707	3.275	5.650	8.753
FCB - b	1.442	2.884	3.605	1.081	0.604	2.074	3.797	8.803
SG - b	2.160	4.319	5.399	1.620	0.736	2.579	4.829	8.395

Cyclic Connection Experiments								
	Pinching4 backbone parameters (mean)*							
Type	ePf$_1$ (kN)	ePf$_2$ (kN)	ePf$_3$ (kN)	ePf$_4$ (kN)	ePd$_1$ (mm)	ePd$_2$ (mm)	ePd$_3$ (mm)	ePd$_4$ (mm)
FCB - a	0.987	1.973	2.466	0.437	0.454	1.838	3.429	6.750
FCB - b	1.135	2.270	2.837	0.348	0.415	1.447	2.299	6.083
SG - b	1.618	3.236	4.045	0.169	0.426	1.449	3.001	7.333

	Pinching4 un- and re-loading parameters (mean)*		
Type	rForceP	rDispP	uForceP
FCB - a	0.027	0.437	0.001
FCB - b	0.046	0.346	0.001
SG - b	0.017	0.412	0.001

$*$ Symmetric negative parameters

A four-point nonlinear cyclic backbone response for each sheathing-screw assembly is extracted similarly to the monotonic tests pre-peak, while the fourth point post-peak (points D and H) is chosen at lower drifts to eliminate potential overestimation of energy and/or ductility. An average backbone of the three repetitions of all FCB-a, FCB-b and SG-b configurations is extracted by selecting the minimum backbone curve between the positive and negative quadrant to enforce symmetry, as illustrated in Fig. 3.4 (bottom graphs). All load and displacement parameters of the backbones under cyclic loading are summarized in Table 3.5, and the respective stiffness parameters are presented in Table 3.6.

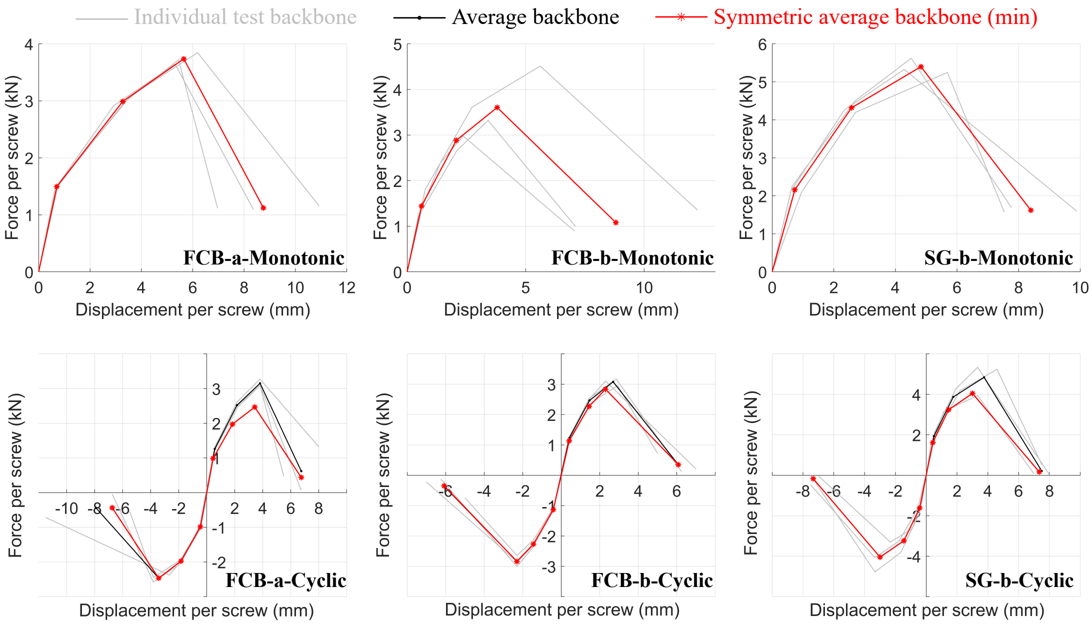

Figure 3.4: Average connection response for both monotonic (top graphs) and cyclic (bottom graphs) loading. Average of the three repetitions of each sheathing-screw configuration is calculated through a four-point backbone for monotonic tests. Symmetric average backbone is obtained by using the minimum average response between positive and negative quadrants for the cyclic tests.

To extract the hysteretic parameters (un-loading: uForceP and uForceN, re-loading: rDispP, rForceP, rDispN and rForceN) of CFS-to-FCB and CFS-to-SG connections, an optimization method in MATLAB [73] is introduced. The optimization scheme is based on the minimization of the error in strength, cumulative energy and energy per cycle between each experiment and the respective Pinching4 model. The cumulative energy of the proposed Pinching4 model is compared with the experimental cumulative energy in Fig. 3.6, concluding a result agreement for all test configurations (FCB-a, FCB-b, SG-b) and test repetitions. To obtain the recommended symmetric average Pinching4 parameters shown in Table 3.5, the un-loading parameters (uForceP, uForceN) are set equal to 0.001 for this optimization method as adopted by Peterman et al. [83]. The load-displacement behavior of the proposed Pinching4 model in comparison to the response of each of the FCB-a, FCB-b, SG-b test repetition is illustrated in Fig. 3.7.

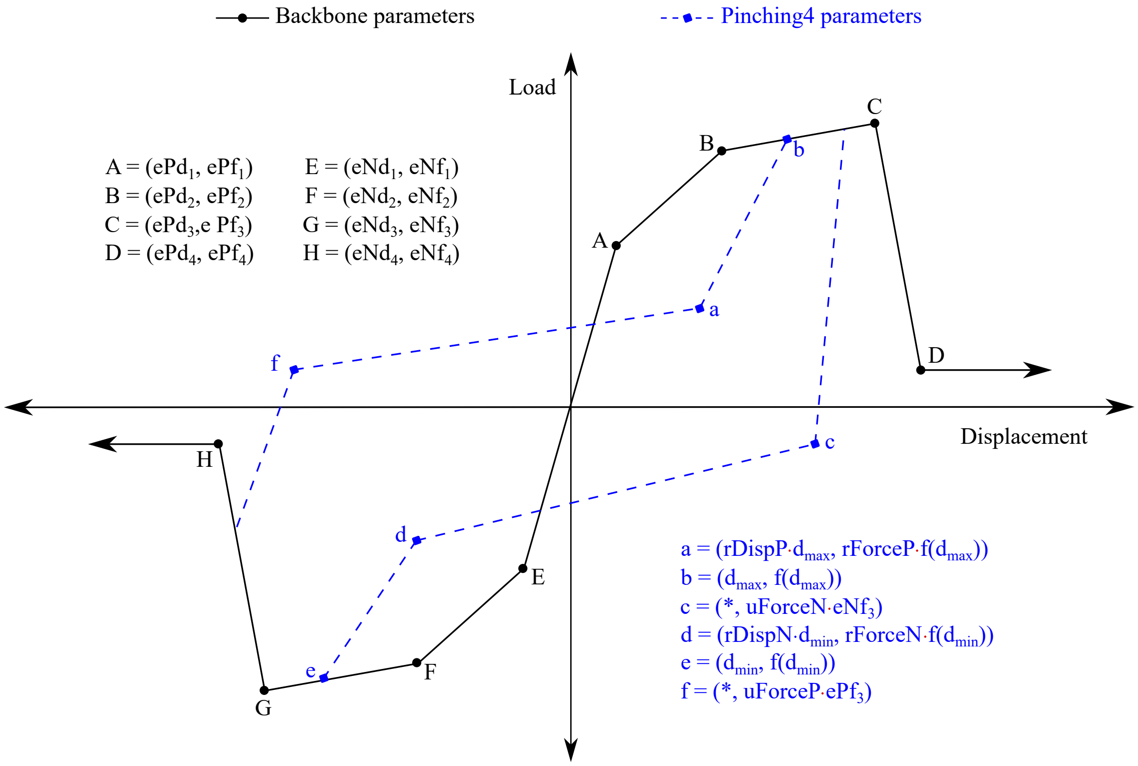

Figure 3.5: Pinching4 uniaxial model composed of four-point backbones and hysteretic parameters (un-loading and re-loading parameters). Uppercase letters are used to define the connection backbones, while lowercase letters are used to characterize the hysteretic parametets in cyclic loading.

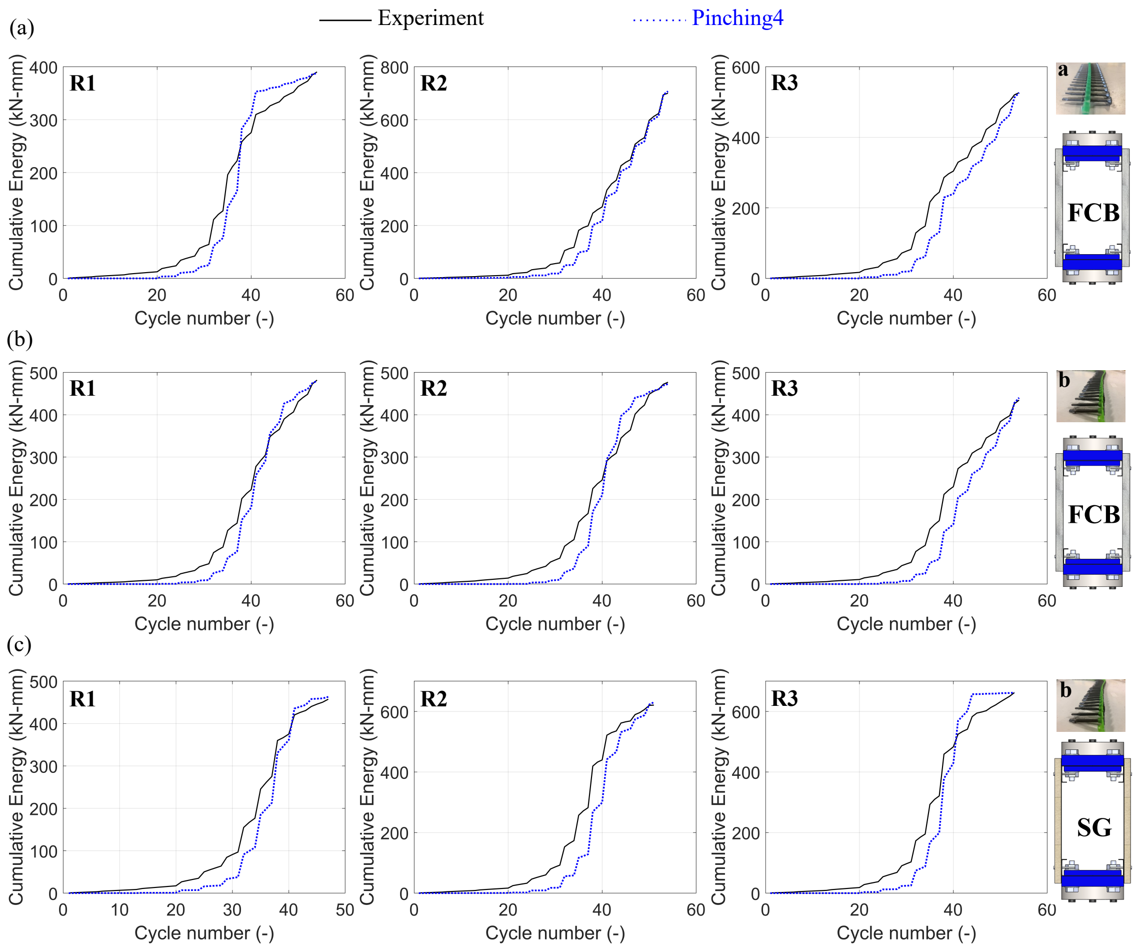

Figure 3.6: Cumulative energy against cycle number of Pinching4 model results in comparison to individual screw test results for (a) FCB-a, (b) FCB-b, and (c) SG-b specimens for all repetitions. Pinching4 models are in agreement with the experimental response.

The average cyclic test results are used for comparisons between the different stud-screw-sheathing configurations. SG-sheathed connection specimens are governed by higher peak strength and stiffness in comparison to FCB sheathed specimens (both FCB-a and FCB-b) by 42-64% and 39-75% respectively. Between the different screw types in FCB-sheathed specimens, FCB-a displayed lower capacity and lower stiffness compared to FCB-b specimens, by 15% and 26% respectively. In general, average cyclic behavior is less strong and more stiff for the respective monotonic behavior of the different FCB-a, FCB-b and SG-b configurations.

Table 3.6: Stiffness of CFS-to-sheathing connections at each branch of the average four-point backbones under monotonic and cyclic loading. K_1 at 0-40% peak load, K_2 at 40-80% peak load, K_3 at 80-100% peak load and K_4 at 100%-last point post-peak load represent the stiffness of all examined sheathing-screw specimens.

Monotonic Connection Experiments				
Sheathing -screw	K_1 (kN/mm)	K_2 (kN/mm)	K_3 (kN/mm)	K_4 (kN/mm)
FCB - a	2.115	0.582	0.315	−0.843
FCB - b	2.387	0.981	0.418	−0.504
SG - b	2.935	1.171	0.480	−1.060

Cyclic Connection Experiments				
Sheathing -screw	K_1 (kN/mm)	K_2 (kN/mm)	K_3 (kN/mm)	K_4 (kN/mm)
FCB - a	2.174	0.712	0.310	−0.611
FCB - b	2.735	1.100	0.665	−0.658
SG - b	3.798	1.582	0.521	−0.895

3.3 Finite element modeling of FCB- and SG-sheathed CFS shear walls

The behavior of high-capacity sheathings (FCB and SG composite) in the full response of CFS shear walls is evaluated in this work through a finite element modeling method described in Chapter 2 and adopted herein. This method suggests a fastener-based finite element model emphasizing the significance of the CFS-to-sheathing connections in the shear wall strength, stiffness and dominant failures. OSB-sheathed shear wall experimental data used in Chapter 2 to validate the introduced method, while this Chapter aims to expand the capabilities of this benchmark modeling effort into FCB- and SG-sheathed shear walls.

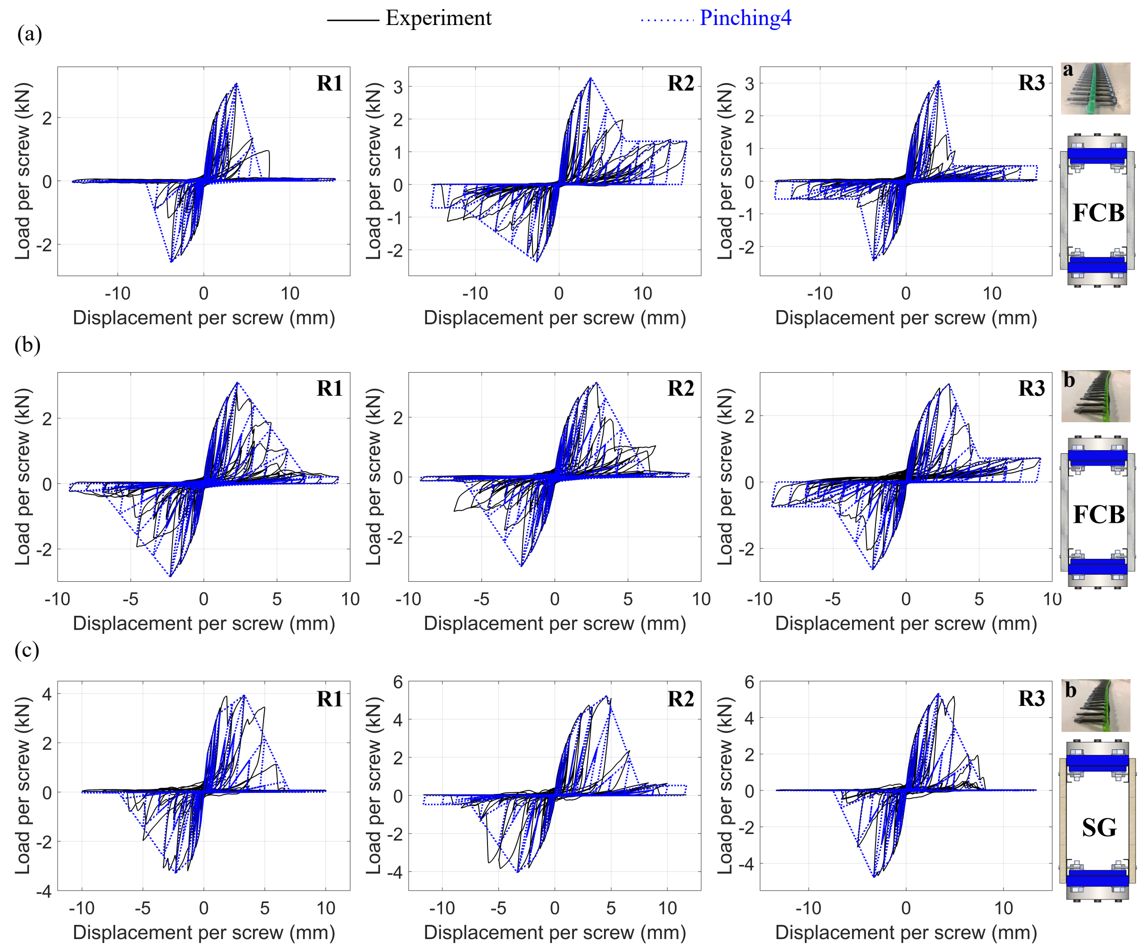

Figure 3.7: Resulted Pinching4 connection response in comparison with the respective experimental results for (a) FCB-a, (b) FCB-b, and (c) SG-b of all test repetitions. The force-displacement response herein indicate behavior at each single fastener. Pinching4 parameters are obtained via an optimization method based on strength and cumulative energy.

The computational model is based on a two-stage method comprised of a linear elastic analysis at Stage A to obtain the CFS-to-sheathing connection vector force rotation during applied loading, and a final pushover analysis at Stage B by implementing local coordinate systems to account for the vector force rotation angle. All existing nonlinearities (connection and geometric) and plasticity are eliminated during Stage A, while included at Stage B to obtain the resulted and accurate lateral shear wall behavior. The alignment of one of the shear axes of the local coordinate systems with the vector force directions aims to accurately predict the connection capacities (eliminating potential overestimation).

3.3.1 Computational model geometry and description

The adopted shear wall configuration is a typical 1.22 m × 2.44 m (4 ft × 8 ft) shear wall of an aspect ratio of h:w=2:1 as required by the current design AISI-S400 [5] specifications. The selected structural shear wall archetype, as depicted in Fig. 3.8, is adopted by the test rig of Branston [18] and is modified in terms of sheathing type and thickness (FCB and SG sheathing instead of OSB) and CFS profiles to implement the experimentally-derived connection response from Section 3.2. In detail, the CFS structural frame is sheathed in the exterior and is connected to the foundation by hold-downs. Fasteners between sheathing (FCB and SG) and CFS members (stud and tracks) are located at 12.7 mm (1/2 in.) from the edges of the sheathing panels by varying their spacing. As recommended by AISI-S400-15 [5], the impact of perimeter fastener spacing is investigated through a 152.4 mm (6 in.), a 101.6 mm (4 in.), a 76.2 mm (3 in.), and a 50.8 mm (2 in.) connection spacing, while field to sheathing connection spacing is maintained constant and equal to 304.8 mm (12 in.). The wall component dimensions and cross-sectional properties (similarly to the connection specimens in Table 3.1) are selected as follows:

- CFS studs of a thickness of 1.37 mm (54 mils), web depth of 152.4 mm (6 in.), flange width of 41.3 mm (3.62 in.), and lip depth of 12.7 mm (0.5 in.).
- CFS tracks of a thickness of 1.37 mm (54 mils), web depth of 152.4 mm (6 in.), and flange width of 41.3 mm (3.62 in.).
- FCB sheathing of a thickness of 19.05 mm (0.75 in.) or SG composite of a thickness of 16.59 mm (0.65 in.) composed of steel of a thickness of 0.719 mm

(0.0283 in.) adhered to gypsum of a thickness of 15.875 mm (5/8 in.).

- M4 x 50 (No. 8) screw (type *a*) or M4 x 40 (No.8) screw (type *b*) for the connections between CFS members and sheathing.
- M5 (No. 10) screws for the connections between CFS studs to CFS tracks, and M4 (No. 8) screws for back-to-back stud connections.
- Simpson Strong-Tie S/HD10S hold-downs (Simpson Strong-Tie Co. Inc. [98]).

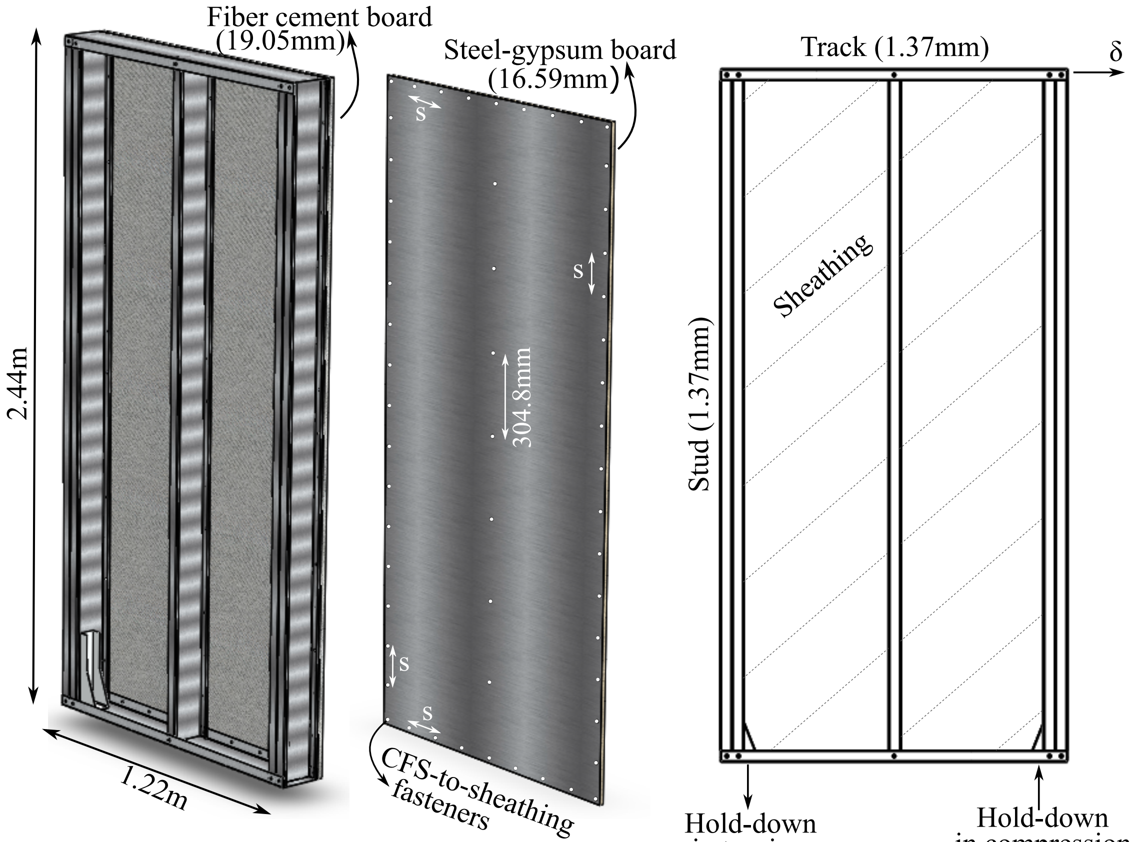

Figure 3.8: FCB-sheathed or SG-sheathed CFS shear wall configurations used in the finite element modeling approach. The adopted shear wall configuration is based on the experimental rig of Branston [18]. A wall aspect ratio of h:w=2:1 (height:width) is selected and the impact of fastener spacing (s=152.4mm, s=101.6mm, s=76.2mm, s=50.8mm) is assessed under lateral loading δ.

3.3.2 Mesh size and type

The mesh discretization of CFS members, and FCB and SG sheathing is adopted by Chapter 2 and is displayed in Fig. 3.9 including different wall views. A fine mesh size of 6.35 mm (0.25 in.) is selected for CFS studs and tracks, while a coarser mesh size of 50.8 mm (2 in.) is assigned to both high capacity sheathings (FCB and SG). All shear wall components are simulated through S4R elements which represent four-node shell elements with reduced integration scheme and linear shape functions.

3.3.3 Component material properties

The CFS material properties include a Young's modulus of E=203 GPa (29500 GPa), a Poisson's ration of v=0.3, and a yield strength of σ_y=345 MPa (50 ksi). An elastic perfectly plastic isotropic material is chosen for CFS members.

Due to the governing connection failures, the FCB material is simulated as an elastic isotropic material. A modulus of elasticity equal to 8963 MPa (1300 ksi) is used, as provided from the manufacturer.

The composite SG sheathing is simulated via a composite section definition at which different plies of different elastic moduli are defined. SG is modeled as elastic isotropic material by using a Young's modulus of 203 GPa (29500 ksi) for the steel ply, and a Young's modulus of 3479 MPa (505 ksi) for the gypsum ply as obtained from Gypsum Association [53]. Gypsum bending stiffness $(EI)_g$ is provided as 440-1160 kN-mm^2/mm (3000-8000 lb-in^2/in) and it is converted into Young's modulus as described in Chapter 2 through the equation E_g=12$(EI)_g/{t_g}^3$, where E_g is the gypsum Young's modulus and t$_g$ the gypsum thickness. The gypsum modulus of elasticity varies within 1320–3479 MPa, while the highest E_g is used herein.

3.3.4 Connection modeling and contact definition

The modeling of the connections and the interactions in shear wall simulations is adopted by Chapter 2.

The CFS-to-CFS connections are simulated differently than the CFS-to-sheathing connections (CFS-to-FCB and CFS-to-SG), as follows:

- Multi-point pinned constraints (MPC) are used for CFS-to-CFS connections. The MPC pinned definition is introduced between two nodes by setting their displacements equal. The first chosen node is a dependent node, while the second selected node is the independent. CFS-to-CFS connections are illustrated in Fig. 3.9b between studs and tracks (in the middle of their flanges) and between chord-stud webs (in two lines) spaced every 304.8 mm (12 in.).
- Connector elements Cartesian (CONN3D2) are selected for CFS-to-FCB and CFS-to-SG connections, which act as springlike elements allowing for independent behavior between the three translational degrees of freedom. The first chosen node in the sheathing connected to the second selected node in the CFS members constitute a wire at which CONN3D2 is applied. The two shear connection directions are simulated through the average experimental load-displacement data extracted in Section 3.2 for monotonic tests, while pull-out behavior is set equal to a rigid behavior of a stiffness of 1750000 kN/m (2929 kips/in.)

Contact pairs are used to define the interactions between CFS stud and track to FCB and SG sheathing. Normal behavior to eliminate the out-of-plane penetration of the sheathing into the CFS members is defined through a hard contact definition. Sheathing is chosen as the master surface, while CFS structural frame is selected as the slave surface.

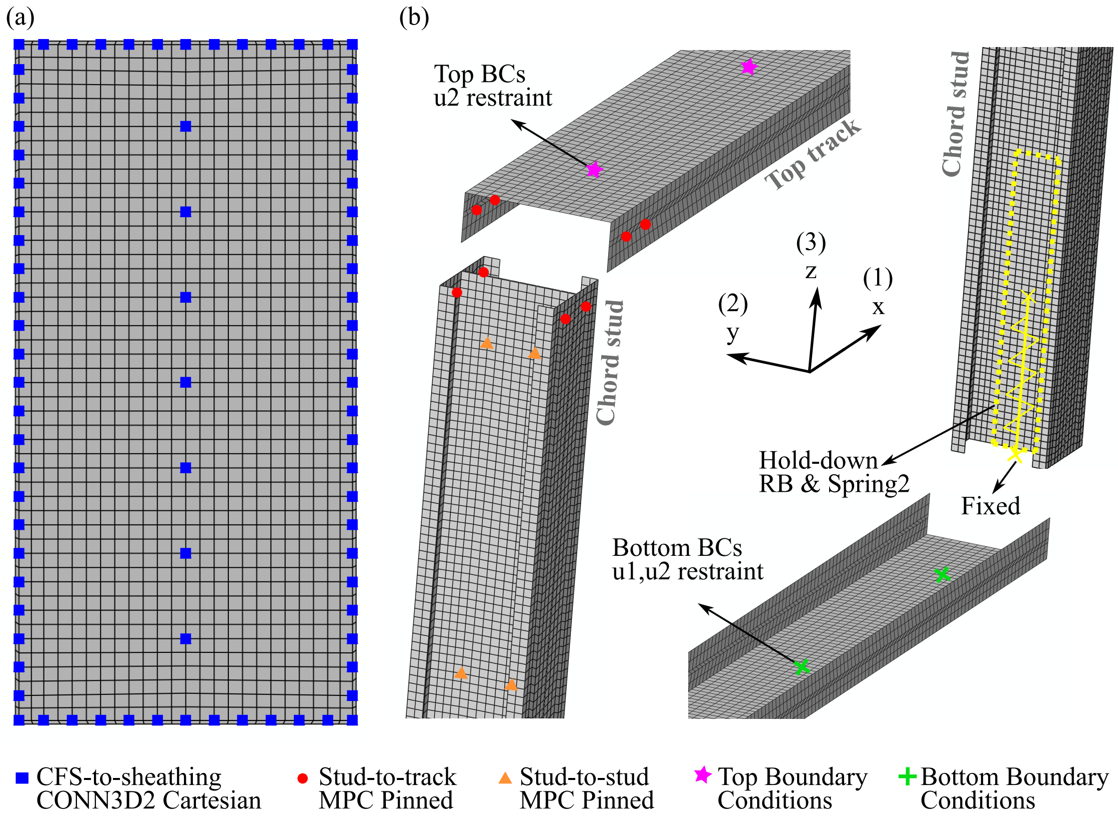

Figure 3.9: FCB-sheathed and SG-sheathed CFS shear wall mesh discretization and connection representation in ABAQUS software. (a) Sheathing mesh is depicted along with CFS-to-sheathing connections simulated via CONN3D2 Cartesian connector element. (b) Exploded view of CFS components (studs and tracks), their mesh and their connections through MPC pinned constraints are shown. Top and bottom boundary conditions, as well as hold-downs simulated by a rigid body and a linear spring behavior (Spring2) are illustrated. A global coordinate system is included.

3.3.5 Applied load and boundary conditions

Monotonic applied loading of 0.08 m (3.15 in.) is introduced at the center of the top track cross-section. A rigid body is defined at this edge of the track tied to a reference point at which the load is applied via displacement control. A maximum and an initial step of 0.01 is chosen, while a minimum step of 10^{-7} is selected.

Top boundary conditions are applied at the web of the top track via six nodes spaced every 230 mm (9 in.), restraining the out-of-plane wall motion (y-axis). Fig. 3.9b illustrates the top track boundary conditions through magenta stars at the locations where the wall is attached to the test rig in Branston [18]. Bottom boundary conditions are introduced in the locations of the shear anchors in Branston [18] and are illustrated via green crosses in Fig. 3.9b. Horizontal (x-axis) and out-of-plane (y-axis) movement are restrained in these node locations.

Hold-downs are attached at the bottom wall part to prevent the wall uplift, as graphically illustrated in Fig. 3.9b. A rigid body is defined at the locations of hold-downs in both chord studs tied to a reference point in the middle. The reference point is connected to the ground via a two-node spring element (Spring2 from ABAQUS) at which a linear behavior is applied in a fixed direction (z-axis). The stiffness of the hold-down spring is calculated based on ASD provisions from Simpson S/HD10S specifications and is equal to 22292 kN/m (127.3 kips/in.) in tension. The stiffness in compression is equal to 1000 times the tensile stiffness (Leng et al. [67]), as discussed in Chapter 2.

3.3.6 FCB- and SG-sheathed CFS shear wall computational results

Load-displacement resultant behavior of FCB-sheathed shear walls fastened with both screw a and screw b, and SG-sheathed shear walls fastened with screw b is illustrated in Fig. 3.10 for the four different perimeter fastener spacings of 152.4 mm (6 in.), 101.6 mm (4 in.), 76.2 mm (3 in.), and 50.8 mm (2 in.). Strength, stiffness and failure mechanisms are discussed herein by comparing the response of the different sheathings, as well as the response of the various fastener spacings for each configuration.

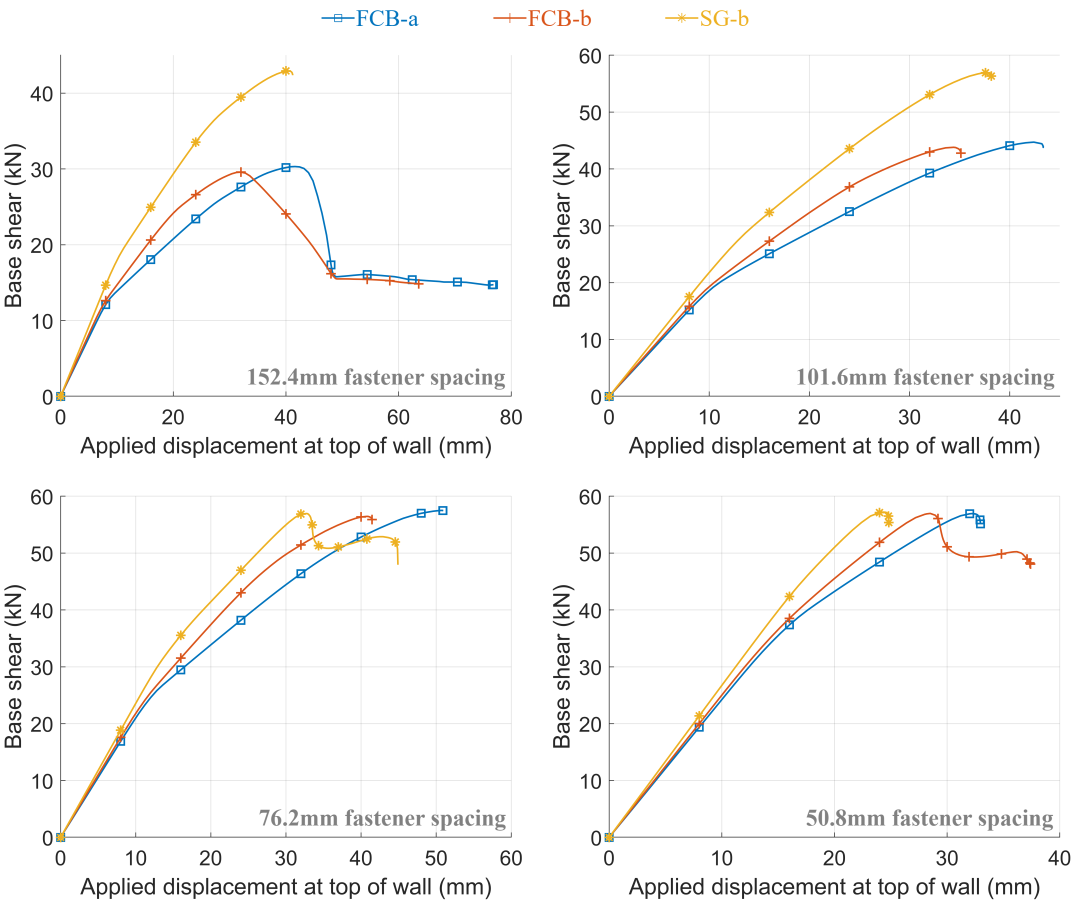

Figure 3.10: Force-displacement finite element response of CFS shear walls sheathed with FCB (for screws a and b) and SG composite (for screw b) for four different fastener spacings, such as 152.4mm, 101.6mm, 76.2mm, 50.8mm (identifier in the lower right part of the graphs). Capacity percentage differences between FCB-sheathed and SG-sheathed shear walls are decreasing as fastener spacing is reducing.

3.3.6.1 Shear wall strength and stiffness

In general, as fastener spacing decreases (more fasteners in the perimeter), the shear wall capacity of all examined shear wall configurations increases, by 25%-48% (Fig. 3.10). Wall peak load (P_{max}) is presented in Table 3.7 for all examined sheathings and perimeter spacings. Higher peak strength is predicted for SG-sheathed shear walls of bigger fastener spacings in comparison to FCB-sheathed shear walls. This strength supremacy reduces as fastener spacing decreases from 152.4 mm (6 in.) to 50.8 mm (2 in.) due to the different governing failure mechanisms discussed in the following Subsection. SG-b shear wall configurations outperform the FCB-sheathed walls, by 0.4%-45%. FCB-a and FCB-b shear walls show little strength variability of 0.02%-2.5% for all fastener spacings.

Initial stiffness (K_{in} between 0-40% peak load) and secant stiffness (K_{sec} between 0-100% peak load) are summarized in Table 3.7 for all fastener spacings and every sheathing-screw configuration. Higher initial and secant stiffness are predicted for SG-sheathed walls compared to FCB-sheathed walls (both screws), by 7%–20% and 16%-53% respectively. Between the different screw types in FCB wall assemblies, FCB-b is governed by a higher initial stiffness of 3%-6%, and a higher secant stiffness 13%-26% in comparison to FCB-a walls for the different fastener spacings.

3.3.6.2 Failure mechanisms and fastener spacing impact

The dominant failure mechanisms (in addition to strength and stiffness) in FCB and SG-sheathed CFS shear walls are largely affected by the perimeter fastener spacings. A fastener spacing of 152.4 mm (6 in.) for all examined sheathing and screw types lead to CFS-to-sheathing connection failures, initiated from the corners of the wall and progressively transferred to each adjacent fastener along stud and track flanges. Failure initiates from the right bottom part of the walls and it distributes to all of the wall corners. For 101.6 mm (4 in.), FCB-sheathed shear walls (fastened with both screw *a* and screw *b*) are governed by CFS-to-sheathing connections, while SG-sheathed shear wall response is dominated by the yielding and large deformation of the top track. The 76.2 mm (3 in.) fastener spacing result to the occurrence of both connection failures and top track failure for FCB-sheathed walls, while SG-sheathed walls are governed exclusively by CFS steel framing failures (top track). At the smallest fastener spacing of 50.8 mm (2 in.), both FCB- and SG-sheathed walls are dominated by the yielding of the top track at the location of the applied load.

Table 3.7: Finite element modeling results of FCB- and SG-sheathed shear walls of the different screw types and perimeter fastener spacings. Secant stiffness K_{sec} (0-100% peak load), initial stiffness K_{in} (0-40% peak load) and peak strength P_{max} are summarized for all computational models.

Assembly type	Spacing (*mm*)	Secant stiffness K_{sec} (*kN/mm*)	Initial stiffness K_{in} (*kN/mm*)	Peak strength P_{max} (*kN*)
FCB - a	152.4	0.729	1.151	30.31
	101.6	1.054	1.874	44.71
	76.20	1.132	2.080	57.50
	50.80	1.768	2.422	56.95
FCB - b	152.4	0.924	1.604	29.58
	101.6	1.274	1.961	43.81
	76.20	1.384	2.172	56.45
	50.80	1.999	2.500	56.96
SG - b	152.4	1.073	1.808	42.92
	101.6	1.515	2.174	56.92
	76.20	1.737	2.325	56.96
	50.80	2.345	2.672	57.20

The different failure mechanisms are illustrated in Fig. 3.11 through connection progression of failure at the wall corners for higher spacings, and von-Mises stresses in the exploded view of the top track as fastener spacing decreases. Small fastener spacings lead to higher rigidity in shear wall perimeters, focusing the failure in the CFS framing itself than in the connections. Fastener spacing constitutes a crucial factor in the capacity, stiffness and failures of FCB- and SG-sheathed CFS shear walls.

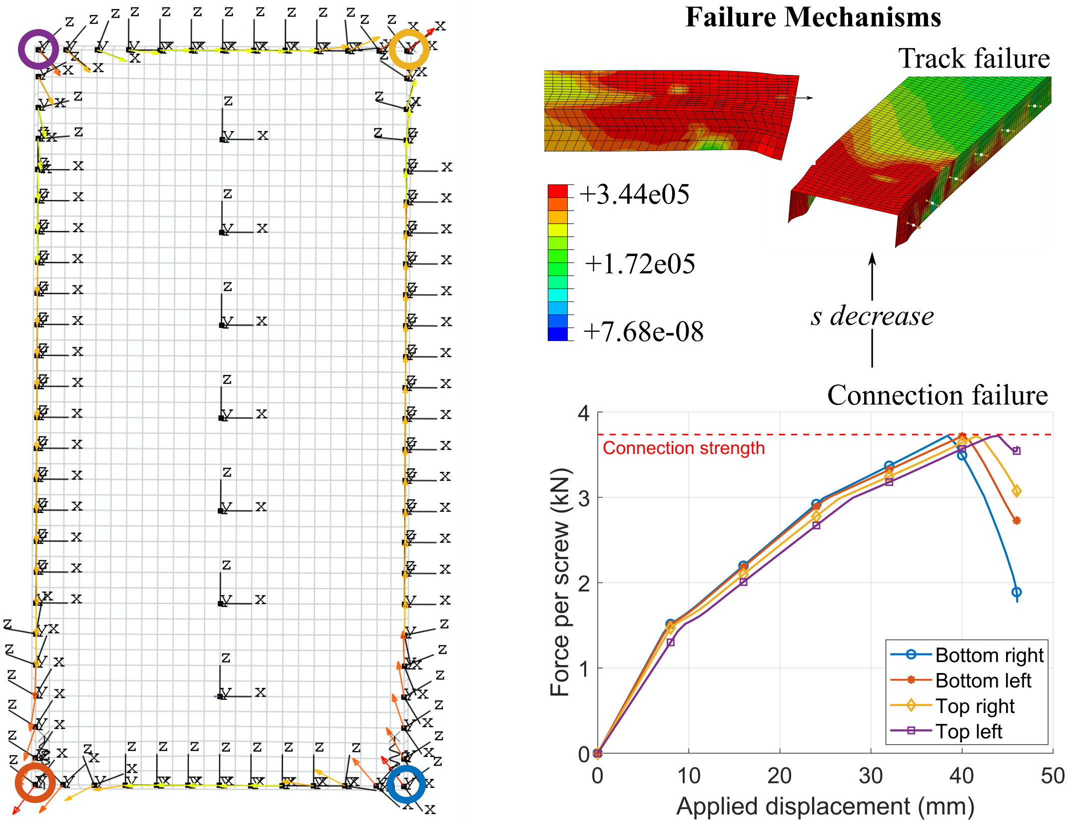

Figure 3.11: Governing failure mechanisms of all different FCB- and SG-sheathed shear walls. The failure mode changes as fastener spacing s decreases (152.4 mm, 101.6 mm, 76.2 mm, 50.8 mm) from CFS-to-sheathing connection progression of failure to CFS track failures. A wall representation including local fastener coordinate systems is depicted, along with progression of connection failures in wall corners and von-Mises stress in top track.

3.4 Shear wall AISI-S400 design recommendations and discussion

Higher capacity sheathings (such as FCB and SG) are not currently enabled within the AISI-S400-15 [5] design specifications. The finite element modeling suite in this study allows for design recommendations of FCB- and SG-sheathed CFS shear walls of different fastener spacings.

3.4.1 Deign capacities of FCB- and SG-sheathed shear walls

Base shear capacities per unit width v_n are provided in Table 3.8, accounting for the different examined sheathings (FCB and SG), screw types (a and b), and fastener spacings (152.4 mm (6 in.), a 101.6 mm (4 in.), a 76.2 mm (3 in.) and a 50.8 mm (2 in.)). Shear wall capacities of an aspect ratio of h:w=2:1 are summarized in Table 3.8, as suggested in AISI-S400-15 [5] code provisions for OSB-sheathed walls. The predicted shear wall capacities of FCB-sheathed walls (both screw types) and SG-sheathed walls are higher than the state-of-the-art OSB-sheathed CFS shear walls. Although OSB-sheathed experiments have been used to validate the finite element method used to provide these design recommendations, future experimental studies on the behavior of shear walls sheathed with FCB and SG are suggested in this work.

Table 3.8: Design recommendations of base shear capacities per unit width (v_n) of FCB- and SG-sheathed CFS shear walls. The results of four perimeter fastener spacings are summarized for a wall aspect ratio 2:1.

		Shear capacity per unit width v_n (kN/m)					
Assembly description	Aspect ratio ($h:w$)	Screw spacing (mm)				CFS thickness (mm)	Screw size-type
		152.4	101.6	76.20	50.80		
19.05 mm FCB	2:1	24.86	36.67	47.16	46.71	1.37	M4 - a
19.05 mm FCB	2:1	24.26	35.93	46.30	46.72	1.37	M4 - b
19.05 mm FCB	2:1	24.56	36.30	46.73	46.72	1.37	M4*
16.59 mm SG	2:1	35.20	46.69	46.72	46.92	1.37	M4 - b

$*$ Average of screw a and b

3.4.2 Impact of shear wall aspect ratio

To validate the design recommendations of FCB- and SG-sheathed CFS shear walls discussed in the previous subsection, the impact of shear wall aspect ratio (h:w higher than 2:1 and lower than 2:1), along with different wall characteristics and dimensions, are computationally evaluated herein and are compared with the wall capacities for h:w=2:1. Two shear wall configurations, as adopted by Liu et al. [70] (illustration in Fig. 3.12), are examined by maintaining the thicknesses and material properties of the FCB and SG sheathings discussed throughout this Chapter (instead of OSB sheathing) and by using the following different wall characteristics, and component dimensions and cross-sectional properties:

- a 1.22 m x 2.74 m (4 ft x 9 ft) wall and a 1.22 m x 2.74 m (4 ft x 9 ft) wall of an aspect ratio of 2.25:1 and 1.125:1 respectively,
- CFS tracks of a thickness of 1.37 mm and a cross section of 157.4 mm deep web, and 38.1 mm wide flange (600T150-54),
- CFS studs of a thickness of 1.37 mm and a cross section of 152.4 mm deep web, 41.3 mm wide flange, and 12.7 mm deep lip (600S162-54),
- a perimeter staggered fastener spacing of 152.4 mm (6 in.), and a field stud fastener spacing of 304.8mm (12in.),
- S/HDU6 Simpson Strong-tie hold-downs of a tensile stiffness of 2929 kN/m (56.7 kips/in.) and a compressive stiffness of 1000 times the tensile stiffness.
- a ledger track detail of a thickness of 2.46 mm and a cross section of 304.8 mm deep web, and 50.8 mm wide flange (1200T200-97) in both walls,
- a vertical seam detail of two lines of fasteners in the middle field stud spacing 152.4 mm (6 in.) for the smallest 1.125 wall aspect ratio, and
- an applied monotonic loading of 0.127 m (5 in.) via displacement control.

The finite element modeling approach described in Section 3.3 is used to provide the shear wall capacities of these two walls, which are compared with the predicted shear capacities V_n based on the equations in AISI-S400 [5] design code. For wall aspect ratios h:w≤2 and wall aspect ratios 2<h:w≤4, Eq. 10 and Eq. 11 are used respectively.

Base shear capacity of shear walls of h:w≤2 (h:w=2.25:1 herein) is calculated as:

$$V_n = v_n w \tag{10}$$

Base shear capacity of shear walls of 2<h:w≤4 (h:w=1.125:1 herein) is defined as:

$$V_n = v_n w\left(\frac{2w}{h}\right) \tag{11}$$

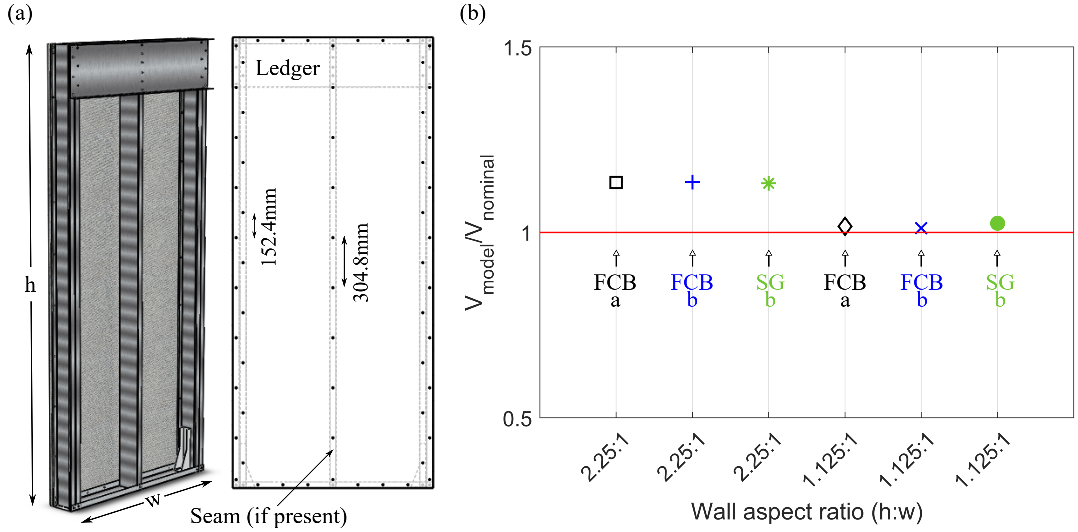

Figure 3.12: FCB- and SG-sheathed CFS shear walls of different aspect ratios of h:w≤2 and 2<h:w≤4. (a) Representation of wall dimensions, components and additional structural details, such as ledger, staggered fasteners and vertical seam (if present). (b) Capacity ratio of finite element model over recommended shear strength predictions for all sheathing-screw wall configurations (FCB-a, FCB-b, SG-b) against wall aspect ratio. Horizontal red line indicates a perfect prediction.

The finite element modeling results are compared to the recommended design base shear capacities in Fig. 3.12 for all FCB-a, FCB-b and SG-b shear wall configurations against the two examined aspect ratios. The horizontal red line indicates a perfect prediction. The resultant shear capacity ratios $V_{model}/V_{nominal}$ indicate an agreement of computational-to-predicted capacities within 1.2%-2.5% for wall aspect ratios lower than 2, while the recommended capacities underestimate the wall behavior by 14%-17% for wall aspect ratios higher than 2 towards conservatism. The more conservative recommended predictions can be associated with the 304.8 mm (1 ft) ledger in the 2.25 wall aspect ratio, which as discussed in Liu et al. [70] might behave as a h:w=2:1 wall.

The evaluation of the lateral performance of FCB- and SG-sheathed CFS shear walls under cyclic loading is an immediate future step of this work to additionally account for the hysteretic wall response using the CFS-to-sheathing Pinching4 parameters recommended in Section 3.3.

4 CONCLUSIONS AND FUTURE WORK: PART I

4.1 Concluding remarks and summary

PART I of this dissertation focused on the lateral performance of cold-formed steel (CFS) shear walls by varying the sheathing type, the screw type, the fastener spacing, the wall aspect ratio, the CFS thickness, the hold-down type, and the presence of constructional details. The shear connection response was also evaluated under monotonic and cyclic loading, and hysteretic parameters were extracted. The conclusions of this dissertation are multifaceted and shed light on innovative higher capacity shear wall design systems.

4.1.1 OSB-sheathed shear walls and connections

A benchmark finite element modeling approach of OSB-sheathed CFS shear walls was introduced accounting for CFS-to-OSB experimental connection variable behavior.

The shear behavior of the connections between CFS members and OSB sheathing were experimentally examined and their inherent response variability was quantified through 30 identical connection tests under monotonic loading. The results demonstrated a significant connection capacity variability of 38%. The connection behavior was governed by two failure mechanisms: a) the pull-through of the screws followed by bearing in the locations of the screws, and b) the shear failure of the screws (broken screws) followed by bearing. An average backbone connection behavior was extracted, along with statistical parameters.

This study also introduced a high fidelity fastener-based finite element modeling approach to evaluate and understand the lateral behavior of CFS-shear walls sheathed with OSB sheathing. The introduced modeling approach was compared and validated with nine different experimental configurations throughout the literature. The results showed that the introduced computational modeling approach accurately captured strength, stiffness, and failure modes in accordance with the experiments. CFS-to-OSB connection behavior represented the most critical load path in shear wall response (initiated from the corners and distributed along stud and track length), and thus important attention was given to their simulation through experimentally-derived behavior. An extensive parametric analysis was conducted and showed that CFS-to-OSB connections response varying between $\mu \pm \sigma$ an $\mu \pm 2\sigma$ significantly affected the shear wall response by 12% and 25% respectively. All the remaining examined parameters did not impact (less than 5%) the shear wall capacity and failures, while stiffness was additionally affected by the OSB shear modulus and the hold-down stiffness.

To further address the connection variability and its effect in shear wall capacity, a probabilistic analysis was conducted. Randomness was introduced in the system behavior through the average connection peak load variable, while stiffness was maintained constant in all generated random fastener backbones. Monte Carlo (MC) simulations on OSB-sheathed shear walls were conducted for three fastener spacings (152.4 mm (6in.), 304.8 mm (12 in.), 609.6 mm (24 in.)), illustrating a wall variability less than 5% for all cases. Higher coefficient of variation was predicted as fastener spacing increased, while MC-to-deterministic mean ratio reduced as fastener spacing increased indicating a series system. These results concluded that although significant variability governed the connection response, less variability dominated the OSB-sheathed CFS shear wall response.

4.1.2 Higher capacity sheathed shear walls and connections

The impact of higher capacity sheathings, such as FCB and composite SG, was investigated using two screw types on connection behavior via monotonic and cyclic experiments, and on full shear wall behavior via high fidelity finite element analyses.

The shear connection behavior of FCB-sheathed specimens fastened with screw *a* and screw *b*, and SG-sheathed specimens fastened with screw *b* was evaluated via an experimental program of 18 tests (9 monotonic and 9 cyclic). Little variability occurred between the identical repetitions of each sheathing-screw configuration, and screw pull-through or shear screw failure governed the connection response for both FCB and SG sheathings, followed by sheathing tear out and/or bearing. CFS-to-FCB and CFS-to-SG capacities were predicted higher than the state-of-the-art CFS-to-OSB connection capacities, while stiffness was slightly higher than OSB-sheathed specimens. SG-sheathed specimens resulted to the highest behavior than FCB-sheathed specimens (screws *a* and *b*). Furthermore, average backbones and Pinching4 hysteretic parameters were obtained from these tests and proposed in this work through an optimization method which minimized the error in strength and cumulative energy.

CFS shear walls sheathed with FCB and SG composite sheathings were computationally examined for four different fastener spacings (152.4 mm (6 in.), 101.6 mm (4 in.) and 76.2 mm (3 in.) and 50.8 mm (2 in.)) under monotonic loading. The finite element modeling results illustrated that SG-sheathed shear walls were governed by a higher peak strength and a higher initial stiffness for bigger fastener spacings (higher than 101.4 mm (4 in.)) in comparison with FCB-sheathed shear walls (screws *a* and *b*), while lower perimeter fastener (lower than 76.2 mm (3 in.)) spacings leaded to similar capacities between the different sheathings. This was attributed to the different dominant failure mechanisms. As fastener spacing on the wall perimeter reduced from 152.4 mm (6 in.) to 50.8 mm (2 in.), the governing failure mechanism shifted from CFS-to-sheathing connection failures to CFS members failures (yielding of the top track). Specifically, FCB-sheathed walls were governed by CFS-to-FCB connection failures for fastener spacing higher than 101.6 mm (4 in.), while top track yielding and large deformation governed the wall response for 50.8 mm (2 in.) fastener spacing. SG-sheathed CFS shear walls were dominated by connection failures for 152.4 mm (6 in.) fastener spacing, while fastener spacing lower than 101.6 mm (4 in.) leaded to the CFS framing failure. This study also introduced innovative design recommendations for FCB- and SG-sheathed shear walls that are not currently enabled in the design specifications of AISI-S400 [5]. Shear capacities per unit width were recommended for these systems focusing on a wall aspect ratio of h:w=2:1, as in the current AISI-S400 provisions for OSB-sheathed walls. The wall aspect ratio and the different wall characteristics and constructional details did not affect the recommended shear capacities. FCB-sheathed and SG-sheathed CFS shear wall shear capacities were predicted higher than the state-of-the-design OSB-sheathed walls.

4.2 Future extensions

This study provided a robust fastener-based finite element modeling method to evaluate the lateral behavior of sheathed CFS shear walls, and recommended innovative design recommendations of high capacity sheathing options. To expand this research and enhance the current findings, the following future extensions are suggested:

- Introduction of a new and accurate design method for sheathed CFS shear walls is an immediate extension of this work. This will aim to improve the conservative resistance factor ϕ=0.6 considered in the current design code provisions for OSB-sheathed CFS shear walls. The probabilistic approach conducted in this dissertation can be used towards this direction by calculating a new resistance factor based on MC-to-deterministic mean capacity ratios and the predicted coefficients of variations for the different fastener spacings. This will improve the design predictions for both researchers and practitioners.

- An experimental program of FCB- and SG-sheathed CFS shear walls is a future step of this study. Although experiments on OSB-sheathed walls are used to validate the introduced computational approach in this work, monotonic and cyclic experiments on FCB- and SG-sheathed CFS shear walls will further support the recommended design capacities. This test program can focus on various wall configurations and characteristics, and provide new wall data to enable the adoption of their superior capacities in the current AISI-S400 code. These high capacity sheathings can be also tested and used in diaphragm design.
- Introduction/modification of the proposed finite element modeling approach to account for the hysteretic fastener response under cyclic loading. This will allow the use of the recommended experimental Pinching4 parameters for FCB- and SG-sheathed connections and the investigation of their cyclic impact in shear wall behavior. Phenomenological performance-based finite element modeling approaches, as well as high-fidelity computational methods can benefit from the Pinching4 connection behavior.
- Investigation of new shear wall characteristics, such as tunable fastener patterns, and exploration of modular CFS wall systems is another suggestion of this work. The benchmark modeling approach of this work can be used to efficiently provide predictions of panelized wall systems in the sub-system level, as well

as in the full building level. This will allow the investigation of innovative prefabricated wall systems based on optimal connection pattern and number, sheathing type and thickness or detail presence of each individual application.

- Development of a simplified modeling approach for sheathed cold-formed steel shear walls is a promising future extension of this work. For example, a spring-like element able to represent the full shear wall lateral response will largely reduce the model computational cost, and will also allow for full building simulations using high fidelity modeling approaches. This method, along with the introduction of analytical closed-form equations, can accurately, cost-efficiently and time-efficiently describe the full shear wall behavior and be easily adopted by engineers in academia and industry.
- Innovative energy absorbing elements/methods to improve the CFS building performance can be examined under earthquake events as a future step. Additive manufacturing and 3D printing techniques can enhance this effort by fabricating new mechanical metamaterials that can provide properties unachievable in the nature (further discussed in PART II of this dissertation). Cellular lattice structures of superior properties, such as multi-stability or auxeticity, can benefit CFS construction by replacing their connecting elements or sheathings.

To conclude, this dissertation is the first research effort of providing an accurate benchmark modeling approach of OSB-sheathed walls by tackling the connection variability, while it provides pioneering design recommendations of FCB- and SG-sheathed higher capacity walls and hysteretic Pinching4 connection parameters. As a result, its expansion will benefit the research community and the design through new and more advantageous methods than the common state-of-the-design structural applications.

Part II:

Mechanical Performance of Metal Plate-Lattice Architected Materials

5 INTRODUCTION: PART II

5.1 Architected materials: background and motivation

The increased demand of lightweight materials with advanced strength and stiffness properties in structural applications pushes to the forefront innovative man-made materials to enhance the state-of-the-art material options. The accelerated development of 3D printing and additive manufacturing techniques (such as direct laser writing (DLW), self-propagating photopolymer waveguides (SPPW), projection micro-stereolithography (PSL)) enhances the opportunities of obtaining new materials of intricate architectures with advantageous and unique properties previously unachievable in nature. Significant attention has been given to cellular solids (materials composed of solids and voids) with mechanical properties determined primarily by their architectural design rather than their solid constituent material. These materials are called architected materials, and along with lattice design adaption (solids in crystal locations) in their topology, they can offer superior material properties and expand the design charts to low-density structures with high strength, stiffness, fracture toughness, damage tolerance, energy absorption, and stability. Furthermore, extraordinary properties such as negative Poisson's ratio, negative stiffness, near zero shear modulus, recoverability, and negative thermal expansion among others, have been attained during the last years by pushing outside of the state-of-the-art methods and by introducing new mechanical metamaterial architectures.

The rapid evolution of engineering materials is discussed by Ashby [9] and is described via material property charts including combinations of two material properties at each of the graphs. These charts indicate not only current material capabilities, but also unattainable property combinations that existing materials haven't achieved yet. This allows for the investigation of innovative architected materials of different geometries to achieve new advantageous properties (Zheng et al. [120], Bauer et al. [10]). Fleck et al. [45] discusses the abilities and behavior of different architectures of micro-architected materials in terms of strength, stiffness and fracture toughness. A significant parameter towards the exploration of different mechanical metamaterials is the use and development of various additive manufacturing techniques. For example, a three-dimensional holographic lithography is explored by Campbell et al. [21] to fabricate microstructures, such as photonic crystals. A laser powder-bed fusion method is used by Wang et al. [111] for the fabrication of high strength and ductility material architectures, while self-propagating photopolymer waveguide approach is studied by Jacobsen et al. [61] for the fabrication of open-cell truss structures, and is also used by Schaedler et al. [88] to construct ultralight microlattice structures with superior properties.

Imperfection sensitivity has been extensively examined in cylindrical shells and spherical shells by describing their behavior with knockdown factors (Seide et al. [92], Peterson et al. [86], Gerasimidis et al. [47], Yadav and Gerasimidis [115], Yadav et al. [114]). Since geometric imperfections are inevitable in real-life (through additive manufacturing or big-scale construction), understanding the imperfection sensitivity of cellular materials and provide knockdown factors can shed light on new properties aiming to fill the empty space in the design charts. Imperfection sensitivity has been greatly examined in two-dimensional cellular solids by investigating the impact of six imperfection types on the yielding of 2D foams (Chen et al. [23]), as well as the effect of five imperfect morphologies on the fracture toughness of 2D lattices (Romijn and Fleck [87]). Furthermore, the imperfection sensitivity of isotropic 2D lattice structures, such us triangular, Kagome and hexagonal grids, is examined by Symons and Fleck [101] with regards to their elastic moduli. Three-dimensional lattice sensitivity to imperfections is also examined via a Selective Laser Melting technique

(Liu et al. [68]), assessing the mechanical performance and failure mechanisms of metallic imperfect lattice structures.

Innovative mechanical metamaterials, as obtained by tailoring their architectures, offer new and superior material properties unachievable by any traditional structural materials, such as concrete or steel. The interconnection of Materials Engineering and Structural Engineering can offer significant benefits to the current construction methods. A notable example is the Eiffel Tower, which is based on a structural hierarchical design. Focusing on innovative ultra-thin cellular lattice structures, understanding their capabilities, and expanding them into imperfection insensitive properties, not only will further fill the material design charts, but will also advance the structural design code provisions.

5.2 Literature review

Cellular lattice materials are categorized either as closed-cell architectures (such as honeycombs) or open-cell architectures (such as trusses). This classification emerges from the geometry of the lattices which determines the deformation and the failure mechanisms of each topology. Open-cell geometries are stretching-dominated materials (strut stretching failures), while closed-cell geometries are bending-dominated materials (cell wall bending failures). The different architected material topologies that have received particular attention during the past years can be chronologically classified as foams and honeycombs, truss-lattices, shell-lattices, and plate-lattices (as illustrated in Fig. 5.1).

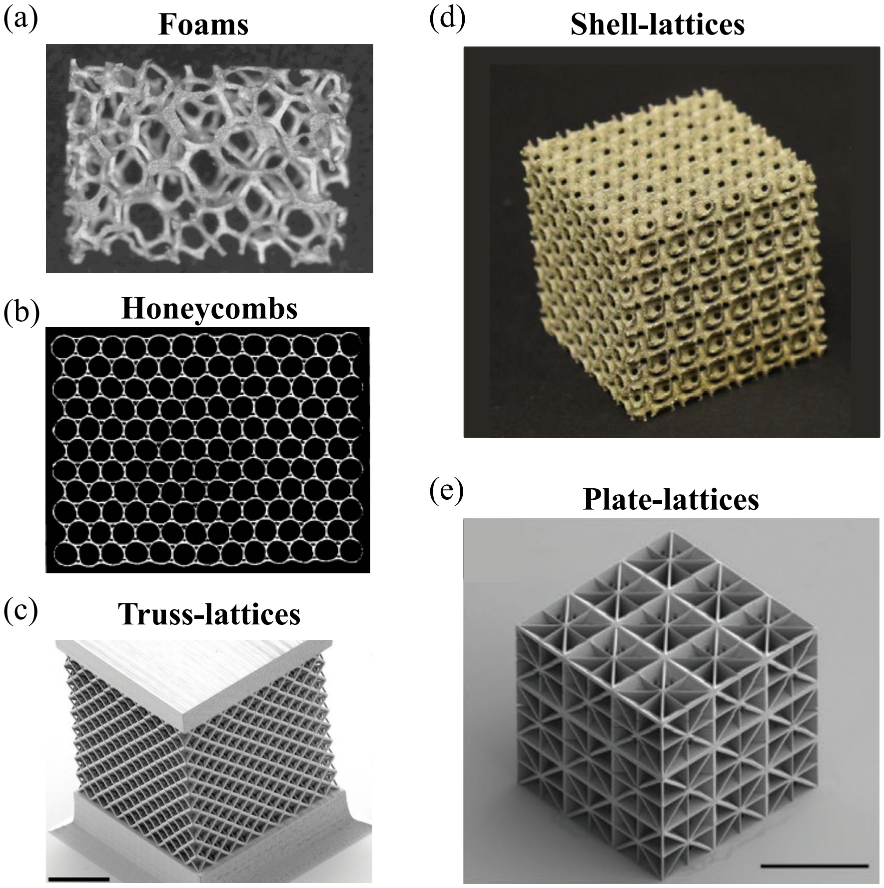

Figure 5.1: Architected material topologies: (a) foams (photo by Deshpande and Fleck [35]) and (b) honeycombs (photo by Papka and Kyriakides [81]), (c) truss-lattices (photo by Gross et al. [51]), (d) shell-lattices (photo by Bonatti and Mohr [17], and (e) plate-lattices (photo by Tancogne-Dejean et al. [102]).

5.2.1 Foam and honeycomb material research

Honeycombs (two-dimensional cellular materials) and foams (three-dimensional cellular materials) have been investigated by multiple research efforts over the past years. Gibson et al. [49] investigated the elastic and plastic mechanical properties of silicone rubber and aluminum honeycombs of different densities and cell geometries via experimental and analytical methods. Polycarbonate honeycombs have been uniaxially crushed (Papka and Kyriakides [82]), and biaxially crushed (Papka and

Kyriakides [81]), demonstrating localized stability-governed collapse mechanisms.

The mechanical performance of foams has been evaluated by Gibson and Ashby [48] through testing and analysis of three types of polymeric foams describing their different collapse mechanisms. Deshpande et al. [34] investigated foams governed of stretching-dominated or bending dominated behavior based on the rigidity of the pin-jointed assemblies of the materials. The impact of strain rate is studied by Deshpande and Fleck [35] via testing of two ultra-light aluminum alloy foams.

5.2.2 Truss-lattice material research

The mechanical performance of truss-lattices have been extensively studied by multiple research efforts (Wallack and Gibson [109], Wicks and Hutchinson [112]), displaying their superior properties against foams and honeycombs. Significant attention has been given to octet truss-lattice materials and their mechanical properties (Deshpande et al. [36], Mohr [77], Elsayed and Pasini [39]). Furthermore, fracture toughness of the octet truss has been evaluated by O'Masta et al. [80], while defect sensitivity has been assessed by Gross et al. [51]. Nanolattices also received a lot of interest by multiple researchers (Gu and Greer [52], Bauer et al. [11]), demonstrating the significant benefits they offer in terms of strength and stiffness, and their potential on upscaling and hierarchy. Meza et al. [75] studied the resilience of hierarchical materials using the octahedron and octet-truss with regards to strength, stiffness, and failure mechanisms. Tancogne-Dejean and Mohr [104] evaluated the response of elastic isotropic truss lattices of cubic symmetry through analytical, experimental and computational work, while Tancogne-Dejean and Mohr [105] showed that tapered truss-lattices resulted to higher elastic moduli and specific energy absorption than the standard rod truss-lattice of the same geometry.

5.2.3 Shell-lattice material research

Recent studies have focused on shellular lattice architectures (continuous smooth shells) concluding their superiority in elastic moduli in comparison to truss-lattices. Han et al. [55] experimentally examined the response of shellular structures of a Triple Periodic Minimal Surface (TPMS-like) in comparison to microlattices and nanolattices, while Han et al. [54] introduced a fabrication method of such structures. Bonatti et al. [16] introduced and investigated optimized smooth-shell TPMS-like materials of face-centered cubic (FCC) geometry via experimental and computational work, demonstrating their advantageous properties against the octet truss. Bonatti et al. [17] expanded this work into additional smooth-shell architectures based on the simple cubic (SC) and body centered cubic (BCC) geometries. Lee et al. [66], computationally evaluated the response of shell-lattices of Schwarz Primitive TPMS structures with periodic boundary conditions, while Al-Ketan et al. [6] experimentally examined the mechanical properties of primary interpenetrating phase composites (IWPs) of TPMS structures under compression in comparison to truss-lattices.

5.2.4 Plate-lattice material research

Recently, a new generation of lattice materials composed of plates in the closest-packed planes of crystals, denoted as plate-lattices, has been explored by Berger et al. [12] and Tancogne-Dejean et al. [102]. Plate-lattice architectures of cubic symmetry have been proposed and compared with truss lattices and/or foams achieving high stiffness (Hashin Shtrikman upper bound [56] is reached) and elastic isotropy. Specifically, Berger et al. [12] numerically and analytically examined the stiffness and elastic isotropy of a cubic+octet foam combination (or simple cubic and face-centered cubic (SC-FCC) combination), while Tancogne-Dejean et al. [102] experimentally and numerically evaluated the stiffness and elastic isotropy of SC-FCC (simple cubic and face-centered cubic) and SC-BCC (simple cubic and body-centered cubic) in comparison to truss-lattices of the same architectures. Furthermore, strength has been investigated by Tancogne-Dejean et al. [103] for different strain rates via experimental and computational methods focusing on SC-BCC, and by Crook et al. [26] for SC-FCC plate-nanolattices showing that plate-lattices can also reach the strength theoretical upper bound (Suquet bound) through experimental and numerical approaches. Plate-lattices have been also approached by Chen et al. [25] and Kader et al. [62] enhancing their advantageous properties against different types of cellular materials and by evaluating their cell morphology, respectively. Besides closed-cell plate-lattices, half-open-cell plate-lattices are also investigated by Duan et al. [38] in comparison to truss-lattices and smooth-shell lattices via experiments and finite element modeling.

Although stiffness has been extensively evaluated showing that plate-lattices are the stiffest materials to date, and strength has been widely approached for high relative densities indicating that plate-lattices are additionally the strongest existing lattices, to the author's knowledge strength and stability of low-density plate-lattice materials has not yet been reported. The understanding of their behavior and their capabilities is crucial for both Materials Engineering and Structural Engineering, since they can fill the current charts with new properties previously unattainable by any architected materials, and enhance the design options with innovative and superior structural materials. The adoption of these materials in structural applications, and specifically in lightweight construction, can potentially improve the performance of infrastructure towards reliability and resilience. Plate-lattices can offer benefits, such as ultra-high strength and stiffness, imperfection insensitivity, energy dissipation mechanisms, damage tolerance, and act as self-healing materials and repair structural components in structural applications.

5.3 Dissertation organization of PART II

This work aims to provide pioneering research on the imperfection sensitivity of plate-lattice architected materials under compression and propose new and accurate knockdown factors for these structures. This study is a high-fidelity finite element modeling approach focused on perfect and imperfect plate-lattices of cubic symmetry with periodic boundary conditions. Eigenmodes are used to introduce the different initial imperfections to the imperfect plate-lattice architectures.

PART II of this dissertation is organized as follows:

- Chapter 5 (this Chapter) includes the introduction and the motivation for PART II of this dissertation, as well as the literature review for the examined fields and the contribution of this study to the research community and the design.

- Chapter 6 focuses on the mechanical elastic properties of metal plate-lattice materials of cubic symmetry by introducing finite element models under compression loading to observe elastic buckling and by comparing the resulted elastic moduli with the theoretical stiffness bound (Hashin-Shtrikman upper bound).

- Chapter 7 presents the stability evaluation and the imperfection sensitivity investigation of plate-lattices. Analytically, this Chapter is composed of fully elastic-plastic nonlinear finite element analyses of perfect and imperfect lattice architectures under compression focusing on low relative densities. This Chapter partially presents the work of Derveni et al. [33].

- Chapter 8 includes the summary and overall conclusions of PART II of this dissertation, as well as future extensions of this work.

6 ELASTIC PROPERTIES AND ELASTIC BUCKLING OF METAL PLATE-LATTICE MATERIALS

Chapter overview: This chapter examines the elastic response of plate-lattice materials, introduces the finite element method, evaluates the Young's, shear and bulk modulus in comparison with the theoretical bounds, and predicts the elastic critical buckling strain for various relative densities.

6.1 Plate-lattice architected materials

Plate-lattice architected materials are innovative materials composed of plates of different orientations in space used to transfer loading between the adjacent members of the lattice structures. The selected different plates of plate-lattices feature a cubic symmetry and are located in a way similar to crystal structures. Berger et al. [12] introduced an isotropic plate-lattice structure composed of a combination of the simple cubic (SC) and face-centered cubic (FCC) symmetry (cubic+octet geometry), and Tancogne-Dejean et al. [102] introduced a design map of more geometries including additionally the body-centered cubic (BCC) symmetry and its combinations (SC-BCC, SC-BCC-FCC) along with SC-FCC. These plate-lattices showed superior properties in comparison to any existing mechanical metamaterials and are adopted and investigated in this current study.

6.1.1 Lattice topology

Unit-cells of SC, BCC, FCC, SC-BCC and SC-FCC, as adapted from Berger et al. [12] and Tancogne-Dejean et al. [102], are constructed as shown in Fig. 6.1. The anisotropic SC, BCC and FCC structures are used to obtain the isotropic combinations SC-BCC and SC-FCC using fractions of the thickness of SC plates (t_{SC}), as indicated in Fig. 6.1. To construct SC-BCC, the thickness of BCC plates is equal to $t_{BCC}=\sqrt{2}t_{SC}$, while to construct SC-FCC the thickness of FCC plates is equal to $t_{FCC}=9t_{SC}/8\sqrt{3}$. The Zener ratio ζ, as defined in Eq. 12, is illustrated against relative density ρ^* for SC-BCC and SC-FCC in Fig. 6.1, demonstrating the isotropy of these structures.

The Zener ratio is calculated as:

$$\zeta = \frac{2C_3}{(C_1 - C_2)} \tag{12}$$

where C_1, C_2 and C_3 are the three elastic constants of the stiffness tensor matrix for geometries of cubic symmetry, as defined in Eq. 13. A Zener ratio equal to $\zeta=1$ indicates isotropy.

The stiffness tensor is defined as:

$$C = \begin{bmatrix} C_1 & C_2 & C_2 & 0 & 0 & 0 \\ C_2 & C_1 & C_2 & 0 & 0 & 0 \\ C_2 & C_2 & C_1 & 0 & 0 & 0 \\ 0 & 0 & 0 & C_3 & 0 & 0 \\ 0 & 0 & 0 & 0 & C_3 & 0 \\ 0 & 0 & 0 & 0 & 0 & C_3 \end{bmatrix} \tag{13}$$

6.1.2 Plate-lattice size

This work examines the mechanical performance of plate-lattices of different relative densities. The ratio of the volume of the solid phase (V_s) by the volume of the unit-cell (V) defines each relative density ρ^*. Relative density varies by altering the thickness of the plates (t_{SC}, t_{BCC}, t_{fCC}) and maintaining constant the side length (L) of the unit-cells. Side length is equal to L=16.404 mm (0.646 in.), while thickness varies from 1.367 mm (0.0538 in.) to ultra-thin 5.468 μm (0.000215 in.). As a result, four different relative densities ρ*=25%, ρ*=15%, ρ*=5% and ρ*=0.5% are selected. Given that SC, BCC, FCC, SC-BCC and SC-FCC geometries are not composed of the same number of plates, the plate thicknesses vary between the different geometries of the same relative densities ρ*, as summarized in Table 6.1.

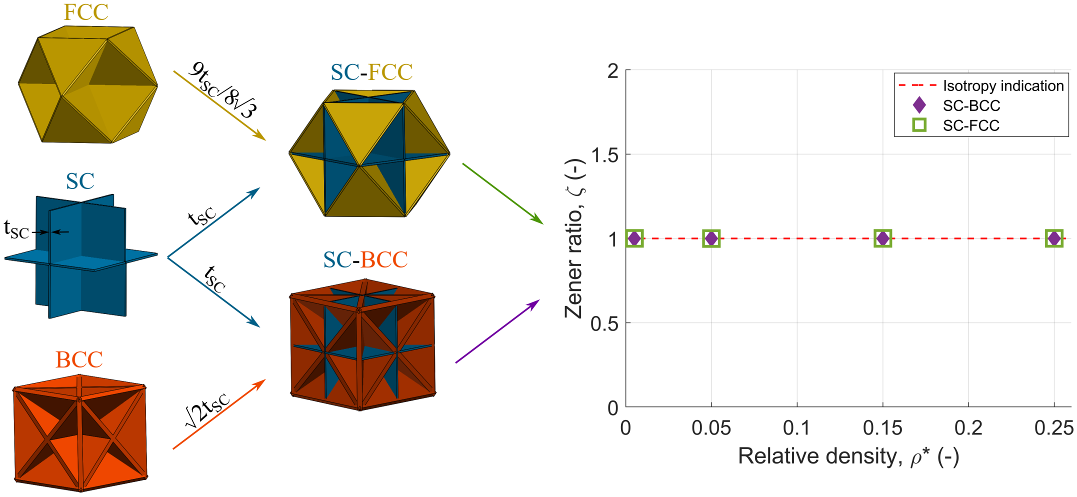

Figure 6.1: Plate-lattice architected materials of cubic symmetry representation. The anisotropic SC, BCC and FCC, and their isotropic combinations SC-BCC, SC-FCC are constructed. Isotropy is obtained via thickness ratios of the constituent geometries (indicated in the arrows using the SC thickness (t_{SC})). The Zener Ratio (ζ) against relative density (ρ*) is illustrated to show the isotropy of SC-BCC and SC-FCC.

6.2 Finite element modeling

High-fidelity computational modeling of plate-lattices is introduced through finite element software ABAQUS (2018) [2]. The modeling approach and assumptions do not alter with the architecture and relative density, in order to obtain consistent and comparable results for all simulations. Material properties, boundary conditions, analysis solver, loading conditions, mesh type and mesh size are described herein. All SC, BCC, FCC, SC-BCC, SC-FCC (adapted from Tancogne-Dejean et al. [102] and/or Berger et al. [12]) geometries are constructed and assembled in ABAQUS.

Table 6.1: Plate thickness of all SC, BCC, FCC, SC-BCC and SC-FCC for relative densities of ρ*=25%, ρ*=15%, ρ*=5% and ρ*=0.5%. Thickness varies for the different geometries of the same relative densities.

		Plate thickness (mm)			
Geometry		ρ*=25%	ρ*=15%	ρ*=5%	ρ*=0.5%
SC	t_{SC}:	1.367	0.820	0.273	0.027
BCC	t_{BCC}:	0.483	0.290	0.097	0.010
FCC	t_{FCC}:	0.592	0.355	0.118	0.012
SC-BCC	t_{SC}*:	0.273	0.164	0.055	0.005
	t_{BCC}:	0.387	0.232	0.077	0.008
SC-FCC	t_{SC}:	0.547	0.328	0.109	0.011
	t_{FCC}*:	0.355	0.213	0.071	0.007

* Minimum thickness also denoted as t in Chapter 7

6.2.1 Constituent material properties

Metal plate-lattices are simulated, and specifically PH1 stainless steel powder properties are used to simulate the base material. The base material is modeled as elastic herein. The Young's Modulus of the selected stainless steel material is equal to E_s=200 GPa (29000 ksi) and the Poisson's ratio is equal to ν=0.3. The base material density is equal to ρ=7.8 g/cm^3 (0.28 lb/in.^{3}).

6.2.2 Mesh size and element type

The plate-lattices are composed and assembled of plates of different orientations in space. This requires same mesh size and element type between the different plates of each architecture in order to merge all the nodes of the plates and to unify the assembly. Mesh type of three-dimensional four-node S4 shell elements are selected from ABAQUS library and a uniform mesh size of 0.3 mm (0.012 in.) is used for all plate-lattice unit-cells. All the nodes in the intersections of plates are merged by merging their mesh. Fig. 6.2 illustrates the meshed SC, BCC, FCC, SC-BCC, and SC-FCC geometries and their dimensions.

6.2.3 Lattice boundary conditions

All unit-cells are simulated by using periodic boundary conditions (PBC). Periodicity is used to represent structures that can be repetitively assembled in all x-, y-, z-directions. This eliminates any possible impact of finite size structures versus tessellations. Periodic boundary conditions are applied via virtual nodes which are connected with equations constraints. The rotation of the boundary surfaces are allowed, while displacements are constrained. Based on the mesh, nodes of the plate-lattice boundary surfaces in opposite sides of the unit-cells are connected via kinematic constraints.

6.2.4 Analysis solver and loading conditions

This study examines both, elastic properties and elastic buckling of plate-lattices of different relative densities. For this reason, Linear Perturbation Analyses are conducted, and specifically Static step is chosen to evaluate the elastic moduli, and Buckle step is selected to assess the elastic buckling of SC, BCC, FCC, SC-BCC, SC-FCC plate-lattice materials. A strain of 0.01 mm/mm is applied in all unit-cells for static and buckle analyses. To define the elastic unit-cell properties, uniaxial compression in all x-, y-, z- directions is applied, as well as shear in all three directions, and biaxial compression in the three directions (simultaneous compression in two axes). To evaluate the elastic buckling capacity, uniaxial compression in x-direction is applied, as shown in Fig. 6.2.

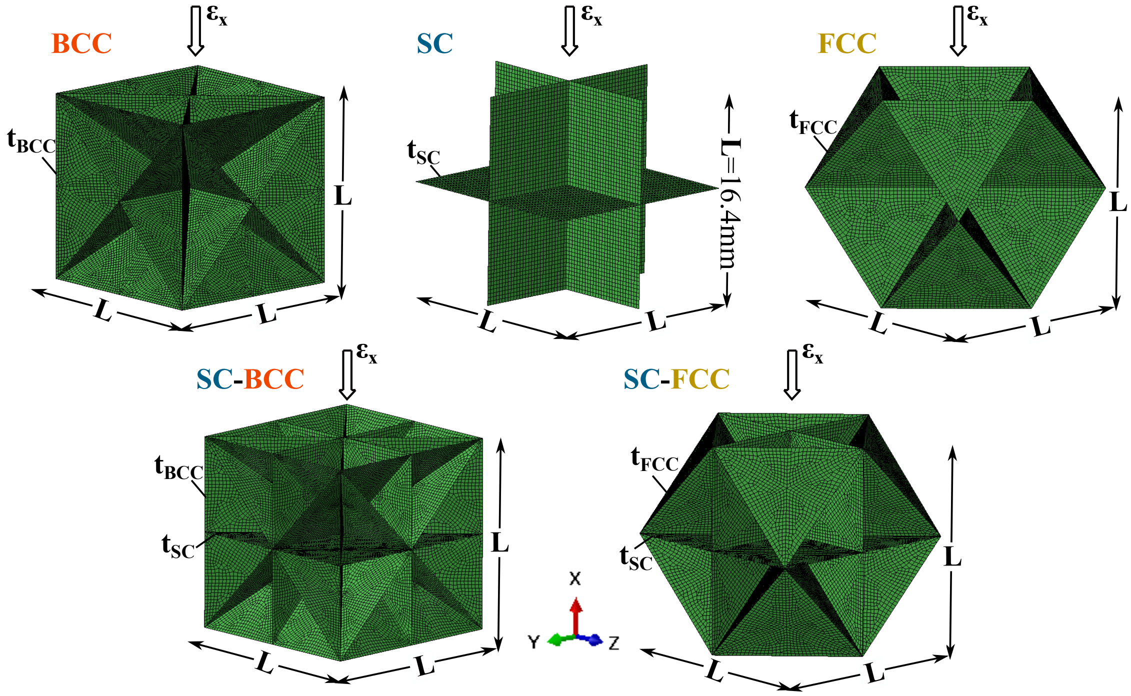

Figure 6.2: Mesh representation for all SC, BCC, FCC, SC-BCC and SC-FCC plate-lattices. The selected mesh size is equal to 0.3 mm (0.012 in.). The unit-cell length remains constant and equal to L=16.404 mm (0.646 in.) and thickness varies with relative density for the different architectures (t_{SC}, t_{BCC}, t_{FCC}). Uniaxial compression is applied for buckling evaluation, while axial compression, shear and biaxial compression are applied for elastic moduli evaluation.

6.3 Elastic results and discussion

The linear elastic performance of plate-lattices are numerically examined and results are provided for stiffness, strength and failures. The resulted elastic moduli are presented to capture the stiffness of SC, BCC, FCC, SC-BCC and SC-FCC, and the resulted elastic critical buckling strains to understand their capacities. The metal elastic moduli predicted herein are also used to validate the introduced finite element (FE) modeling approach by comparing them with Tancogne-Dejean et al. [102] polymer respective moduli. The introduced FE model is further expanded into stability predictions.

6.3.1 Elastic moduli of plate-lattices

Plate-lattice Young's modulus E, shear modulus G and bulk modulus K are evaluated and discussed herein. Fig. 6.3 illustrates the resultant elastic moduli for all anisotropic SC, BCC, FCC architectures and all isotropic SC-BCC, SC-FCC for the different examined relative densities of ρ*=0.5%, ρ*=5%, ρ*=15% and ρ*=25%. Normalized Young's modulus, shear modulus and bulk modulus are obtained by dividing these elastic properties by the respective moduli of the solid material (E_s, G_s, K_s) multiplied by the respective relative densities (ρ*) against relative densities. Deformed shapes of the different loading conditions are illustrated in Fig. 6.4 through von-Mises stress contours of all examined geometries (red color: highest stresses, blue color: lowest stresses).

6.3.1.1 Anisotropic SC, BCC, FCC plate-lattices

The Young's modulus (E), the shear modulus (G) and the bulk modulus (K) of the anisotropic plate-lattices (SC, BCC, FCC), as shown on the right graphs of Fig. 6.3, refer to the [100] loading direction. In detail, the Young's modulus of SC is the highest, while the Young's modulus of FCC is the lowest between the examined architectures. An opposite trend is obtained for the shear modulus, while bulk modulus is similar for all architectures. These results are in accordance with Tancogne et al. [102] (shown in Fig. S1 in their supplementary information for polymer specimens).

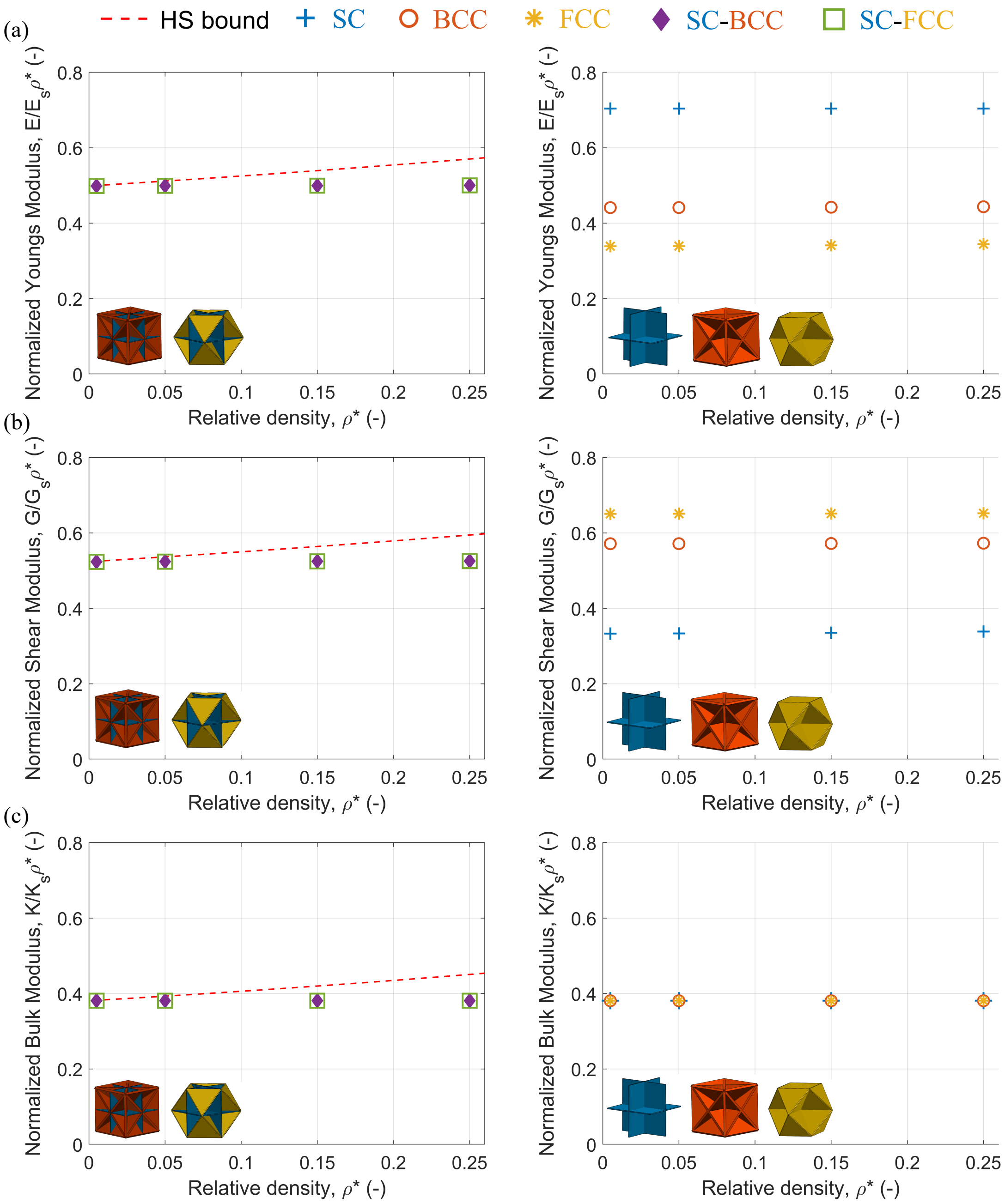

Figure 6.3: Elastic moduli for the anisotropic SC, BCC and FCC, and for the isotropic SC-BCC and SC-FCC in comparison to the theoretical Hashin Shtrikman (HS) upper bound. a) Normalized Young's modulus against relative density (ρ^*), b) normalized shear modulus versus ρ^*, and c) normalized bulk modulus against ρ^* for all geometries. Isotropic plate-lattices reach the HS bound for low relative densities.

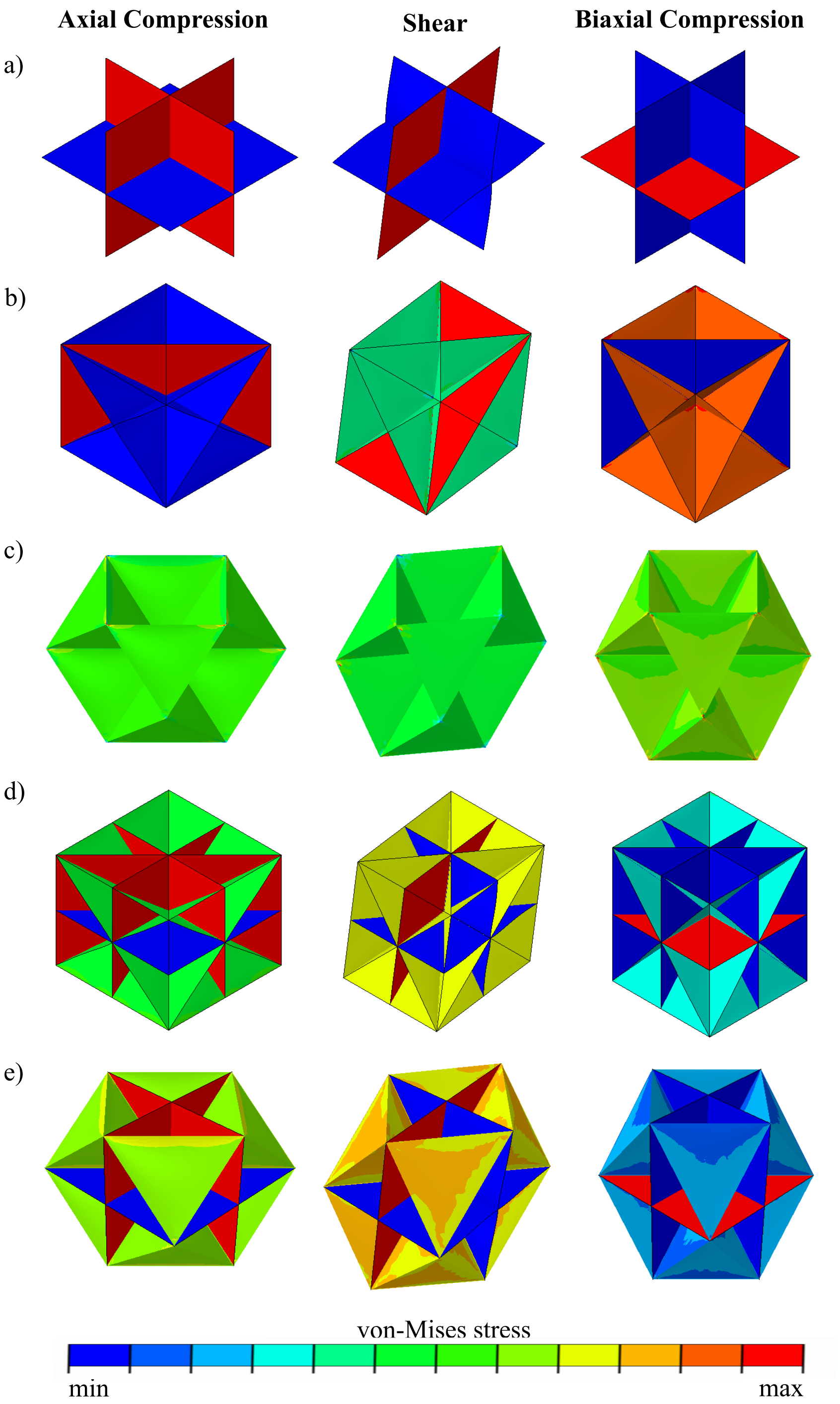

Figure 6.4: Von-Mises stresses of (a) SC, (b) BCC, (c) FCC, d) SC-BCC and e) SC-FCC for different loading conditions, such as uniaxial compression, shear and biaxial compression. The red color represents the highest stresses, the blue the lowest and all the remaining are intermediate stresses.

6.3.1.2 Isotropic SC-BCC, SC-FCC plate-lattices

The elastic moduli E, G and K of the isotropic plate-lattices (SC-BCC, SC-FCC) are depicted on the left graphs of Fig. 6.3, along with the Hashin-Shtrikman (HS) bound predictions. The HS bound is the theoretical stiffness bound for composite two-phase materials. Both, SC-BCC and SC-FCC, are able to achieve the HS upper bound for all Young's, shear and bulk modulus for low relative densities. The HS bound for all elastic moduli is calculated based on Eq. 14, Eq. 15, Eq. 16, Eq. 17 for bulk K_{HS}, shear G_{HS} and Young's E_{HS} modulus, and for the Poisson's ratio v_{HS}, respectively. These results are also in agreement with Tancogne-Dejean et al. [102], and they support the superiority of plate-lattices in terms of stiffness in comparison to any architected materials investigated to date. It needs to be mentioned here that differences for higher relative densities between this current work and Tancogne-Dejean et al. [102] are attributed to the shell element choice in comparison to solid element selection, while for smaller relative densities the resulted stiffness is identical in both studies. This current work investigates low relative densities between ρ^*=0.5% and ρ^*=25% to provide accurate results.

The Hashin-Shtrikman bulk modulus upper bound is defined as:

$$K_{HS} = K_s + \frac{1-\rho^*}{(K_v - K_s)^{-1} + \rho^*(K_s + \frac{4}{3}G_s)^{-1}} \tag{14}$$

The Hashin-Shtrikman shear modulus upper bound is defined as:

$$G_{HS} = G_s + \frac{1-\rho^*}{(G_v - G_s)^{-1} + \frac{2\rho^*(K_s+2G_s)}{5G_s(K_s+\frac{4}{3}G_s)}} \tag{15}$$

The Hashin-Shtrikman upper bound on Young's modulus is calculated as:

$$E_{HS} = \frac{9G_{HS}K_{HS}}{3K_{HS} + G_{HS}} \tag{16}$$

The corresponding Hashin-Shtrikman Poisson's ratio is obtained as:

$$v_{HS} = \frac{3K_{HS} - 2G_{HS}}{2(3K_{HS} + G_{HS})} \tag{17}$$

where E_{HS}, G_{HS}, K_{HS} are the theoretical upper bounds of Young's modulus, shear modulus and bulk modulus, respectively, while E_s, G_s, K_s are the elastic moduli of the solid phase, and K_v=0, G_v=0 are the bulk and shear moduli of the void phase with zero stiffness.

6.3.2 Elastic buckling of plate-lattices

To evaluate and understand the elastic buckling response of plate-lattice architected materials, the different resultant eigenvalues and eigenmodes are extracted from the Buckle analyses. Unit-cells are used for all geometries in this section, except for SC for which a 2x2x2 tessellation is selected. As described in the following Chapter 7 through a tessellation dependency study, a 2x2x2 SC is used to capture buckling wavelengths twice those of the unit cells. All 2x2x2 SC, 1x1x1 BCC, 1x1x1 FCC, 1x1x1 SC-BCC and 1x1x1 SC-FCC plate-lattices with periodic boundary conditions are subjected to uniaxial compression (0.02 mm/mm applied strain for 2x2x2 tessellations instead of 0.01 mm/mm for unit-cells). The first 25 eigenmodes of all geometries are illustrated in Fig. 6.5 for relative densities of ρ*=0.5%, ρ*=5%, ρ*=15%, and ρ*=25%. Fig. 6.5 also includes the first eigenmode shapes of all geometries, that are used in the Chapter 7 as initial imperfections to the geometries. Table 6.2 summarizes the critical buckling strain values based on the first eigenvalue (λ_1), and Fig. 6.6

include the resultant first eigenmode shapes including displacement (magnitude) contours of the different geometries.

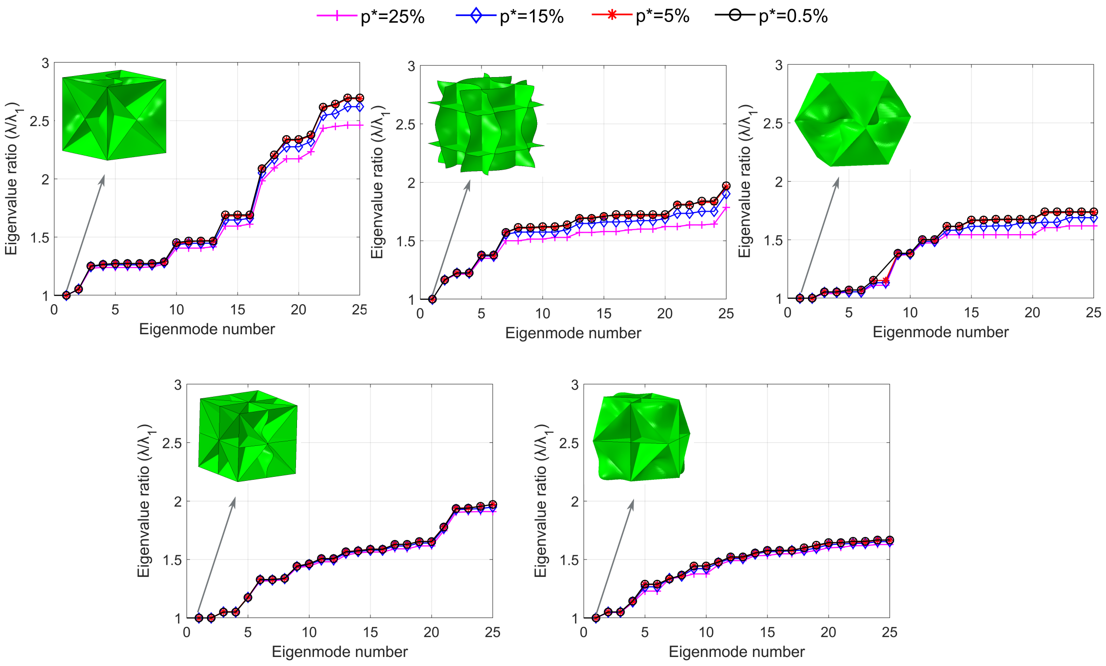

Figure 6.5: Eigenvalue ratio (eigenvalue (λ) normalized by first eigenvalue (λ_1)) against the 25 first eigenmodes. Elastic buckling and imperfection sensitivity is indicated. A λ/λ_1 decrease between the relative densities of each geometry indicates imperfection sensitivity for low-density materials. Lower λ/λ_1 between the architectures indicate geometries more prominent to imperfections. Inset figures depict the first eigenmode shapes.

6.3.2.1 Critical buckling strain of plate-lattices

The results in Fig. 6.5 constitute an indication of the imperfection sensitivity of plate-lattices through normalized eigenvalues (λ/λ_1) as relative density decreases for linear elastic analyses, as well as the stability assessment for all the different geometries. The anisotropic plate-lattices SC, BCC and FCC show a decrease in the normalized eigenvalues as relative density increases for the first 25 eigenmodes. This means that imperfection sensitivity exists for these structures. Imperfection sensitivity is more pronounced in higher eigenmodes. The isotropic plate-lattices, SC-BCC and SC-FCC, result to smaller normalized eigenvalue reductions as relative density decreases from ρ*=25% to ρ*=0.5%. This indicates less imperfection sensitivity between the different densities of the same geometries. The eigenvalue ratios (λ/λ_1) of the isotropic plate-lattice combinations are slightly smaller in comparison to the anisotropic lattice structures (SC, BCC, FCC).

Table 6.2: Elastic buckling capacity of SC, BCC, FCC, SC-BCC and SC-FCC based on the first eigenvalues for densities between ρ*=0.5% and ρ*=25% under uniaxial compression.

Uniaxial Compression				
Plate-lattice geometry	Critical buckling strain λ_1 (mm)			
	ρ*=0.5%	ρ*=5%	ρ*=15%	ρ*=25%
SC	1.218e-5	1.214e-3	0.011	0.028
BCC	0.757e-5	0.755e-3	0.007	0.018
FCC	2.990e-5	2.970e-3	0.026	0.066
SC-BCC	0.378e-5	0.377e-3	0.003	0.009
SC-FCC	0.900e-5	0.898e-3	0.008	0.022

The first eigenvalue represents the most critical buckling capacity towards conservatism, and thus is further discussed herein. As shown in Table 6.2, FCC results to the highest buckling strain for all examined relative densities, which decreases for SC, SC-FCC, BCC and SC-BCC which results to the lowest eigenvalue λ_1. Even though eigenvalues are different over the range of relative densities between ρ*=25% and ρ*=0.5% (decreasing almost linearly), the modal shapes (first eigenmodes) remain constant for each respective eigenmode in all densities. Furthermore, same modal shapes throughout the different relative densities are predicted for higher modes in each architecture, as graphically illustrated in Fig. 6.6. The SC geometry is governed by buckling in the plates aligned with the loading direction. Similarly, BCC lattice structures are governed by plate buckling in the vertical plates, while SC-BCC by the buckling of one set of vertical plates. FCC is dominated by triangular side plate buckling, while SC-FCC by triangular face plate-buckling.

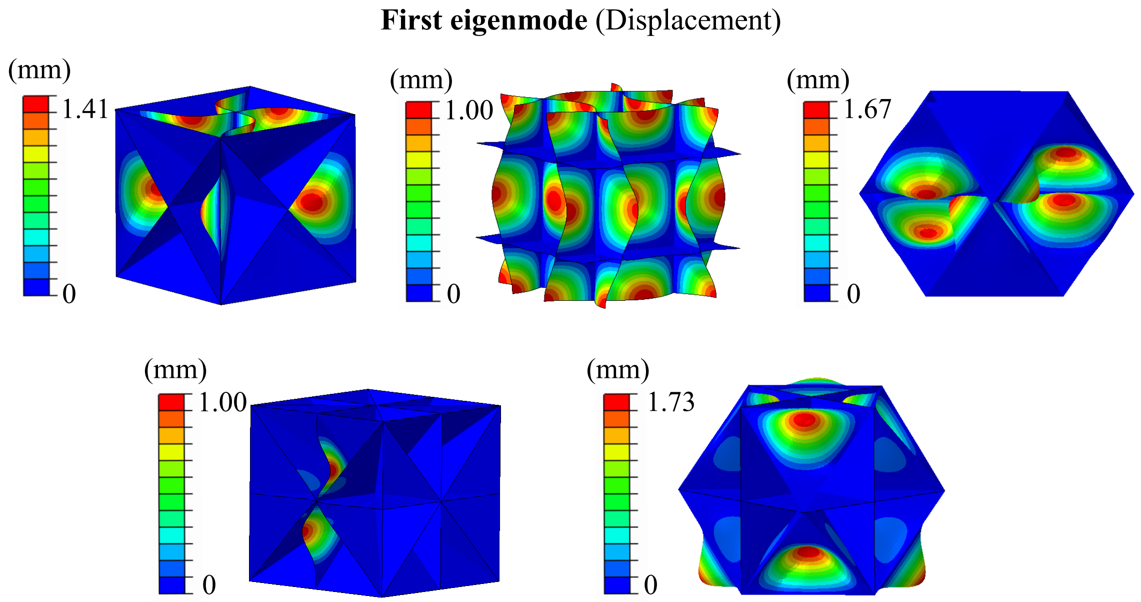

Figure 6.6: First eigenmode illustration of each plate-lattice material for all relative densities within ρ^*=25% and ρ^*=0.5%. The modal shapes remain constant between all relative densities for all architectures (SC, BCC, FCC, SC-BCC, SC-FCC). Contours refer to the displacement (magnitude) for all geometries.

6.3.2.2 Impact of loading type

The critical buckling strain based on the first eigenvalue of plate-lattices under hydrostatic pressure is presented in Table 6.3 for comparison purposes with uniaxial compression eigenvalues. An applied strain of 0.01 mm/mm is chosen for all three directions. The first eigenvalues of the same relative densities for the different loading conditions show the same trend as FCC and SC have the highest capacity and SC-BCC results to the lowest capacity between the examined geometries. Lower eigenvalues of plate-lattices are predicted under hydrostatic pressure when compared to uniaxial compression. First eigenmode shapes also differ between hydrostatic loading and uniaxial compression loading.

Table 6.3: Elastic buckling capacity of SC, BCC, FCC, SC-BCC and SC-FCC based on the first eigenvalues for densities between ρ^*=0.5% and ρ^*=25% under hydrostatic pressure.

Hydrostatic Pressure				
Plate-lattice geometry	Critical buckling strain λ_1 (mm)			
	ρ^*=0.5%	ρ^*=5%	ρ^*=15%	ρ^*=25%
SC	5.281e-6	5.262e-4	4.612e-3	0.012
BCC	2.312e-6	2.309e-4	2.058e-3	0.006
FCC	5.265e-6	5.249e-4	4.612e-3	0.012
SC-BCC	1.503e-6	1.501e-4	1.342e-3	0.004
SC-FCC	1.894e-6	1.892e-4	1.688e-3	0.005

Elastic and hyperelastic buckling capacity including geometric nonlinearities and imperfection sensitivity is an immediate future step of this work to fully characterize the elastic performance of plate-lattice materials under uniaxial compression and/or hydrostatic pressure. These results will also aim to introduce new and/or imperfection insensitive plate-lattice geometries.

7 IMPERFECTION SENSITIVITY AND KNOCKDOWN FACTORS OF METAL PLATE-LATTICE ARCHITECTED MATERIALS

Chapter overview: This chapter investigates the stability and imperfection sensitivity of plate-lattice materials, describes the finite element modeling approach, discusses the plate-lattice response of different relative densities in terms of strength, stiffness and failure mechanisms, and suggests innovative knockdown factors.

7.1 Plate-lattice materials and methods

Plate-lattice mechanical metamaterials are innovative materials composed of plates in a manner analogous to crystal structures. Similarly to Chapter 6, closed-cell geometries are selected in this study, and the mechanical performance of the different lattice topologies is examined for various relative densities. Since the selected plate-lattices result to superior properties in terms of stiffness (Berger et al. [12], Tancogne-Dejean et al. [102]) and strength (Crook et al. [26]) in comparison to any existing architected materials, the goal of this work is to additionally shed light on the unexplored stability and imperfection sensitivity of these materials. The different architectures and relative densities, as well as the introduced finite element method are described herein.

7.1.1 Plate-lattice geometry

Five plate-lattice material topologies, as described in Chapter 6, are selected and illustrated in Fig. 7.1a. The simple cubic (SC), the body-centered cubic (BCC), and the face-centered cubic (FCC) structures are used independently and in combinations. All SC, BCC, and FCC geometries are lattices of cubic symmetry and they are anisotropic. The combinations of these architectures based on different thickness ratios between their plates lead to the isotropic plate-lattices SC-BCC and SC-FCC. Analytical equations on the thickness combination ratios of these materials are discussed by Berger et al. [12] and Tancogne-Dejean et al. [102] and are adopted herein. Eq. 18 displays the thickness ratios of the SC-BCC lattice combinations, while Eq. 19 displays the thickness ratios of the SC-FCC combinations.

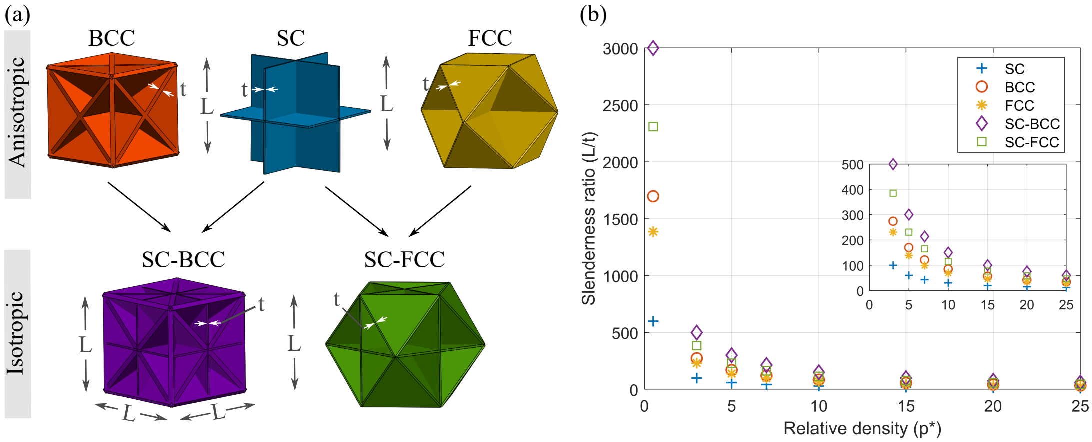

Figure 7.1: Plate-lattice architected material architectures. (a) Three anisotropic elementary architectures of cubic symmetry (SC, BCC,FCC) and two isotropic combinations (SC-BCC, SC-FCC). Side length L is constant for all unit-cells, while t represents the minimum plate thickness of each geometry, (b) slenderness ratio (L/t) against relative density (ρ^*) graph indicating the thickness differences between the architectures of the same density. The lowest slenderness ratios are observed in SC, while the highest slenderness are shown in SC-BCC.

The isotropic SC-BCC plate-lattices are calculated as:

$$\frac{t_{BCC}}{t_{SC}} = \sqrt{2} \tag{18}$$

The isotropic SC-FCC plate-lattices are defined as:

$$\frac{t_{FCC}}{t_{SC}} = \frac{9}{8\sqrt{3}} \tag{19}$$

where t_{SC} is the plate thickness of SC geometry, t_{BCC} is the plate thickness of BCC geometry, and t_{FCC} is the plate thickness of FCC geometry.

A variety of relative densities is examined by varying the thickness of the plate-lattices and maintaining constant the unit-cell length. Specifically, relative densities between ρ*=0.5% and ρ*=25% are selected aiming to provide pioneering results on ultra-low relative densities. Relative densities are calculated based on the ratios of volume of the solid constituent (V_s) over the volume of the whole unit-cell (V), as depicted in Eq. 20 (ρ* of each plate-lattice geometry is calculated via Eq. 21, Eq. 22, Eq. 23, Eq. 24 and Eq. 25 in Appendix B). The unit-cell length is equal to L=16.404 mm (0.649 in.) for all geometries (as in Tancogne-Dejean et al. [103]).

$$\rho^* = \frac{V_s}{V} \tag{20}$$

Since the main goal of this study is to explore and understand the stability and sensitivity of plate-lattices to geometric imperfections, the material sizes can be also described by their plate slenderness ratios, similarly to cylindrical and spherical shell definitions. The slenderness ratio is defined as the ratio of the constant length L over the minimum plate thickness t (L/t). The plate thickness of the lattices varies between the different geometries of the same relative density. Fig. 7.1b illustrates the slenderness ratio of all SC, BCC, FCC, SC-BCC, and SC-FCC plate-lattices against their relative density. SC, BCC, FCC are composed of plates of uniform thickness throughout the unit-cell (constant thickness), while SC-BCC and SC-FCC are composed of two different thicknesses based on each constituent geometry, from which t refers to the SC plate thickness and to the FCC plate thickness, respectively (minimum thickness at each case). As number of plates increases between the geometries, plate thickness decreases, and thus slenderness ratios increase for the same relative density. As a result, SC-BCC has the highest slenderness ratios since it is the most braced with plates geometry, while SC has the lowest slenderness ratios as it is composed of fewer plates in comparison to all geometries of the same densities.

7.1.2 Finite element modeling

Herein, 200 nonlinear plastic analyses are conducted to examine the imperfection sensitivity, as well as 40 linear elastic analysis to obtain the respective modal shapes that are used as initial imperfections for the imperfect geometries. High-fidelity finite element analysis is conducted through finite element software ABAQUS ([2]). Table 7.1 summarizes the simulated geometries and the analysis suite for this section.

Table 7.1: Finite element analysis matrix and methods for plate-lattice architected material imperfection sensitivity study. Imperfections are included as modal shapes and knockdown factors are recommended for ρ*=25% to ρ*=0.5%.

Relative density	Anisotropic			Isotropic	
(ρ*)	SC	BCC	FCC	SC-BCC	SC-FCC
ρ*=25%, ρ*=20%,	40 Linear Eigenvalue Analyses				
ρ*=15%, ρ*=10%,	→ Initial imperfection shapes				
ρ*=7%, ρ*=5%,	200 Nonlinear Dynamic Analyses				
ρ*=3%, ρ*=0.5%	→ Knockdown factors of 0t, 0.1t, 0.5t, 1t, 2t				

7.1.2.1 Mesh size, element type, and material properties

As described in Chapter 6, S4 four-node shell elements are used for the simulation of all geometries. Different element types (S4, S4R, S8R, S3, S3R) have been also examined, and S4 is chosen based on result accuracy and computational cost reduction. The mesh size is selected as 0.3 mm (0.012 in.) for all geometries, which is in agreement with Tancogne-Dejean et al. [103] and Crook et al. [26] mesh sizes. Equal number of elements is used in all the constituent plates of each plate-lattice material, which allows for mesh merging of the nodes and elements at the intersections. This is necessary in order to restrict the constituent plates of behaving independently in space, and to assure accurate load transferring between the components. Mesh convergence and mesh sizes are depicted in Fig. 7.2 for all SC, BCC, FCC, SC-BCC, SC-FCC plate-lattices.

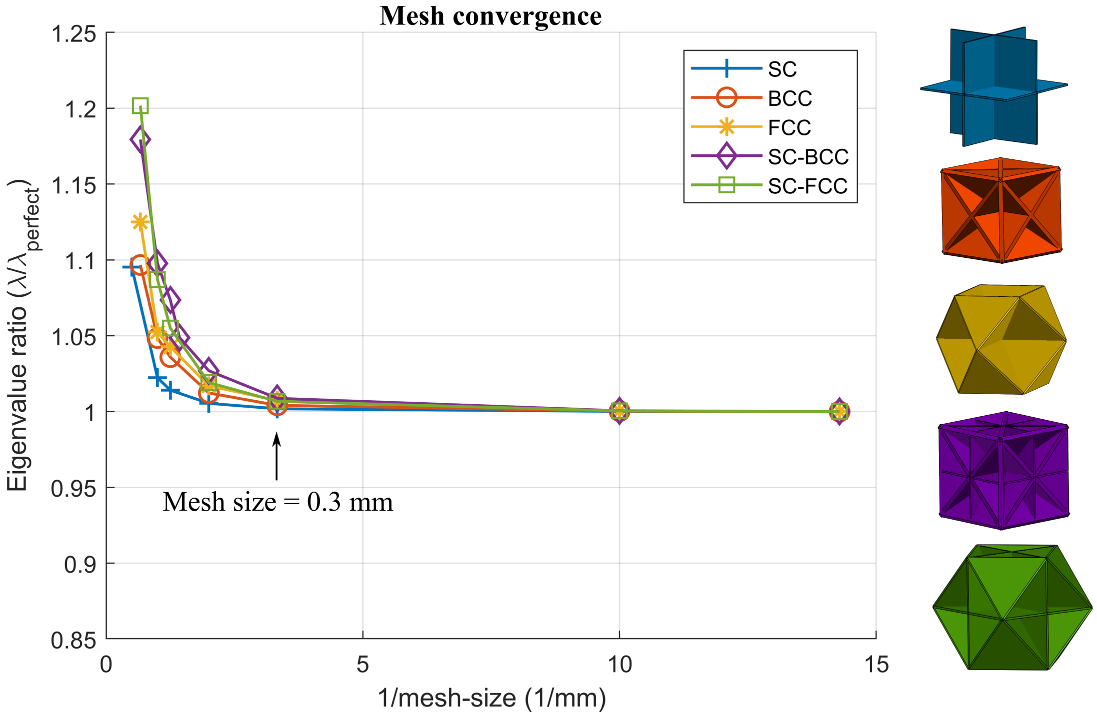

Figure 7.2: Mesh convergence based on the first eigenvalue ratio ($\lambda/\lambda_{perfect}$) against the ratio 1/mesh-size for all anisotropic SC, BCC and FCC, and isotropic SC-BCC and SC-FCC. A constant mesh size of 0.3 mm (0.012 in.) is selected for all examined geometries and for all relative densities using S4 elements.

This work focuses on metal plate-lattices, and specifically the PH1 stainless steel powder is used, as discussed in Chapter 6. The constituent material is simulated as elastic perfectly plastic and its properties (Young's modulus E_s, yield strength σ_y, density ρ) are summarized in Table 7.2.

Table 7.2: Material properties of stainless steel SC, BCC, FCC, SC-BCC, SC-FCC plate-lattice architected materials.

Material Property	PH1 Stainless Steel *
Young's modulus	200 GPa
Yield strength	1000 MPa
Density	7.8 g/cc

∗ Simulated as elastic-perfectly plastic

7.1.2.2 Uniaxial loading and boundary conditions

The plate-lattices are subjected to uniaxial compression (at x-direction). The strain rate is selected as 0.0004/sec for all architectures. Dynamic Implicit solver is chosen for all analyses, since Static General and Static Riks cannot accurately capture the response of the low-density materials. A Quasi-Static application is selected and a Smooth Step amplitude is used. A time period of T=50 sec, an initial and maximum increment size of 0.005, and a minimum step size of 10^{-10} are applied. The preceding parameters are obtained via an extensive parametric study, which aims to accurately capture the full behavior of all lattice structures, and in parallel to reduce the computational cost. For this purpose, a stiffness damping coefficient of 0.001 is also incorporated in the models. Geometric nonlinearities are also included in this work.

Periodic boundary conditions are used to simulate the plate-lattice materials aiming to reduce any finite size effects. Kinematic constraints are applied between the periodic pairs (matching nodes) in the lattice boundary surfaces. The periodic boundary condition application includes virtual nodes through equation constraints.

7.1.2.3 Tessellation dependency

To further eliminate finite size effects, a tessellation dependency study is conducted. Tessellation numbers of up to 10x10x10 are examined in terms of eigenvalue 1. Fig. 7.3 illustrates that the BCC, FCC, SC-BCC, and SC-FCC can be accurately simulated through unit-cell models with periodic boundary conditions, while SC first eigenvalue convergence is achieved for 2x2x2 tessellations. The first eigenmode shape of SC is governed by buckling with a wavelength twice that of the unit-cell in contrast to the remaining geometries. Since the first eigenmode is used in this work, as an initial imperfection, the tessellation dependency convergence is mainly focused on this parameter.

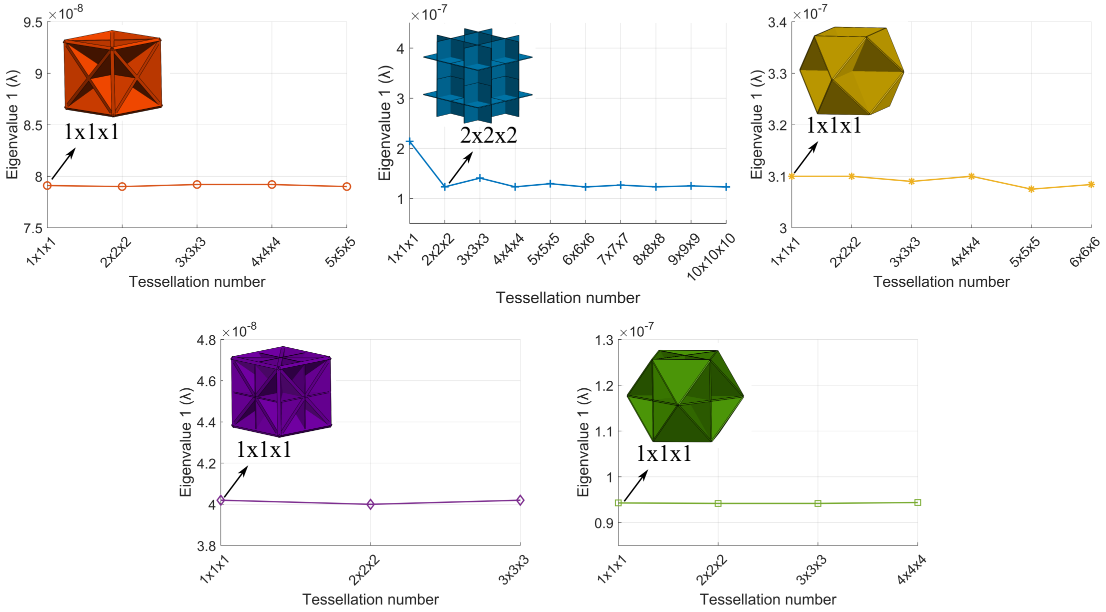

Figure 7.3: Tessellation dependency study. Eigenvalue against tessellation number is displayed for all architectures (up to 10x10x10 tessellation). A 1x1x1 unit-cell is chosen for BCC, FCC, SC-BCC and SC-FCC, while a 2x2x2 tessellation is selected for SC to provide accurate results. The resulted eigenmodes illustrated that SC is governed by a buckling mode twice the length of the unit-cells.

7.2 Modal shapes and imperfections

Since the main focus of this study is the imperfection sensitivity of plate-lattices, the selection of imperfection amplitudes and the different resulted eigenmodes and eigenvalues need to be discussed for all 2x2x2 SC, 1x1x1 BCC, 1x1x1 FCC, 1x1x1 SC-BCC, 1x1x1 SC-FCC. A comparison of the critical buckling strain between the geometries is also illustrated.

7.2.1 Imperfection amplitudes

Imperfections are introduced in all the geometries based on their modal shapes. Specifically, the first eigenmode is used as an initial imperfection and its magnitude is scaled by the thickness of the plates. The imperfection amplitudes considered in this work are $0.1t$, $0.5t$, $1t$, and $2t$, where t is the minimum thickness of the plates of each plate-lattice. Although SC, BCC and FCC are composed of a uniform plate thickness with a constant t, SC-BCC and SC-FCC are composed of two sets of elementary plate architectures and thus the minimum t is used towards conservatism. Since the imperfection sensitivity of plate-lattices is evaluated for a range of relative densities between ρ^*=0.5% and ρ^*=25%, the selected amplitudes vary for the different densities. The impact of an imperfection amplitude of a constant magnitude regardless the relative density is also evaluated in the Subsection 7.3.4.

7.2.2 Eigenmodes and eigenvalues

The first eigenvalues and eigenmodes are illustrated in Fig. 7.4. The critical buckling strain based on the first eigenvalue varies between the architectures. The isotropic combinations SC-BCC and SC-FCC result to lower critical buckling strain values in comparison to the anisotropic SC, BCC and FCC plate-lattice buckling strains (FCC outperforms the remaining geometries in critical buckling strain). SC-BCC and SC-FCC are composed of more plates and thus they are composed of more braced lengths in contrast to SC, BCC and FCC.

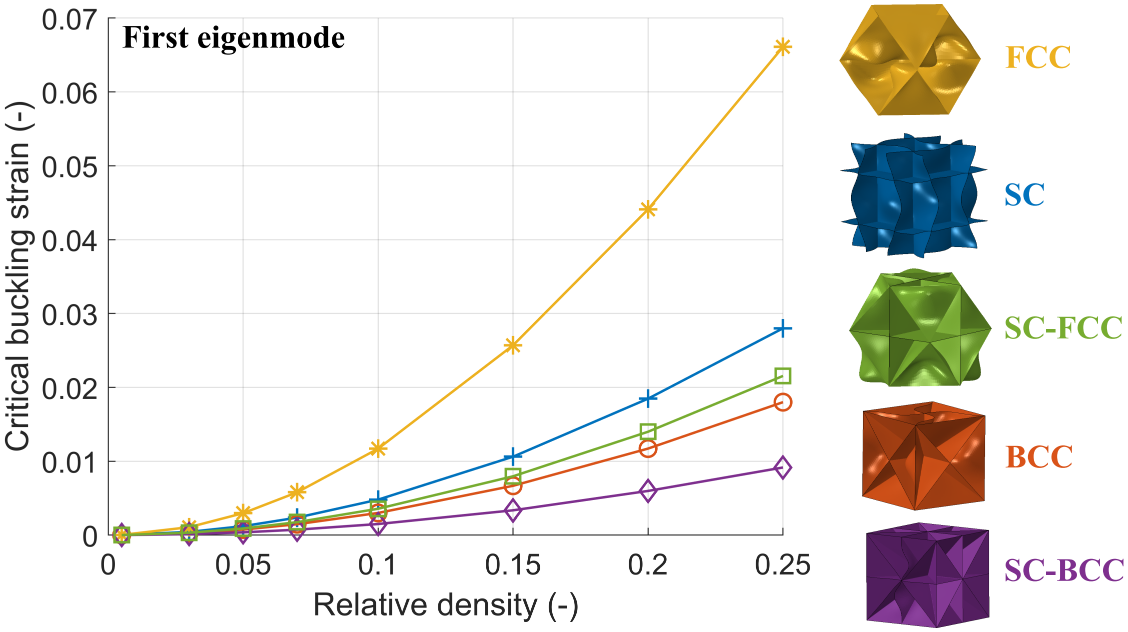

Figure 7.4: Summarized first eigenvalues and eigenmodes of all plate-lattice materials for various relative densities within ρ^*=25% and ρ^*=0.5%. Modal shapes (eigenmode 1) depicted herein remain constant between all relative densities for all architectures (SC, BCC, FCC, SC-BCC, SC-FCC). The critical buckling strain (eigenvalue 1) of the isotropic combinations (SC-BCC and SC-FCC) is smaller than the anisotropic lattices (SC, BCC and FCC).

The first eigenmodes, as shown in the inset figures of Fig. 7.4, are the selected initial imperfections of the imperfect lattices. These modal shapes do not vary with relative density, and thus the same imperfect shape is introduced for all relative densities of the same architecture. The SC and BCC plate-lattice imperfections are mainly focused on the plates aligned with the loading direction, while the FCC geometric imperfections are concentrated in the side triangular plates. The SC-BCC imperfect shape is more pronounced in one of the plates aligned with the loading directions, and the SC-FCC imperfect shape is based on the face triangular plate deformation. The impact of different modal shapes as initial imperfections is also examined in Subsection 7.3.4.

7.3 Stability results and discussion

The goal of this work is to assess the strength, stiffness and failure modes of perfect and imperfect plate-lattices, and to introduce accurate knockdown factors of strength and stiffness for various relative densities and imperfection amplitudes. Herein, the finite element results and main findings for material behavior including plasticity are presented and discussed.

7.3.1 Strength and stiffness

Fig. 7.5 (along with Fig. B.1, Fig. B.2, Fig. B.3, Fig. B.4 in Appendix B) depict the macroscopic stress versus the applied strain for all SC, BCC, FCC, SC-BCC, and SC-FCC plate-lattices of various relative densities (four out of the eight densities within ρ^*=25% and ρ^*=0.5%), respectively. These results are intended for comparisons between the different relative densities of each geometry, as well as for comparisons between the different geometries in terms of strength and initial stiffness.

The capacity of all examined plate-lattices decreases as relative density decreases (thinner plates). This trend is also illustrated in Fig. 7.6 via peak load against relative density graphs. The strength from ρ^*=25% to ρ^*=0.5% does not decrease linearly throughout the density range due to the different governing failure mechanisms between higher and lower relative densities (discussed in the following Subsection 7.3.2). SC plate-lattices result to higher strength in comparison to all other geometries since they are composed of plates 80% thicker than the SC-BCC which is composed of the most and thinnest plates. The effect of imperfection amplitudes in the capacity of plate-lattices varies for the different relative densities of each architecture, and is discussed in Subsection 7.3.3.

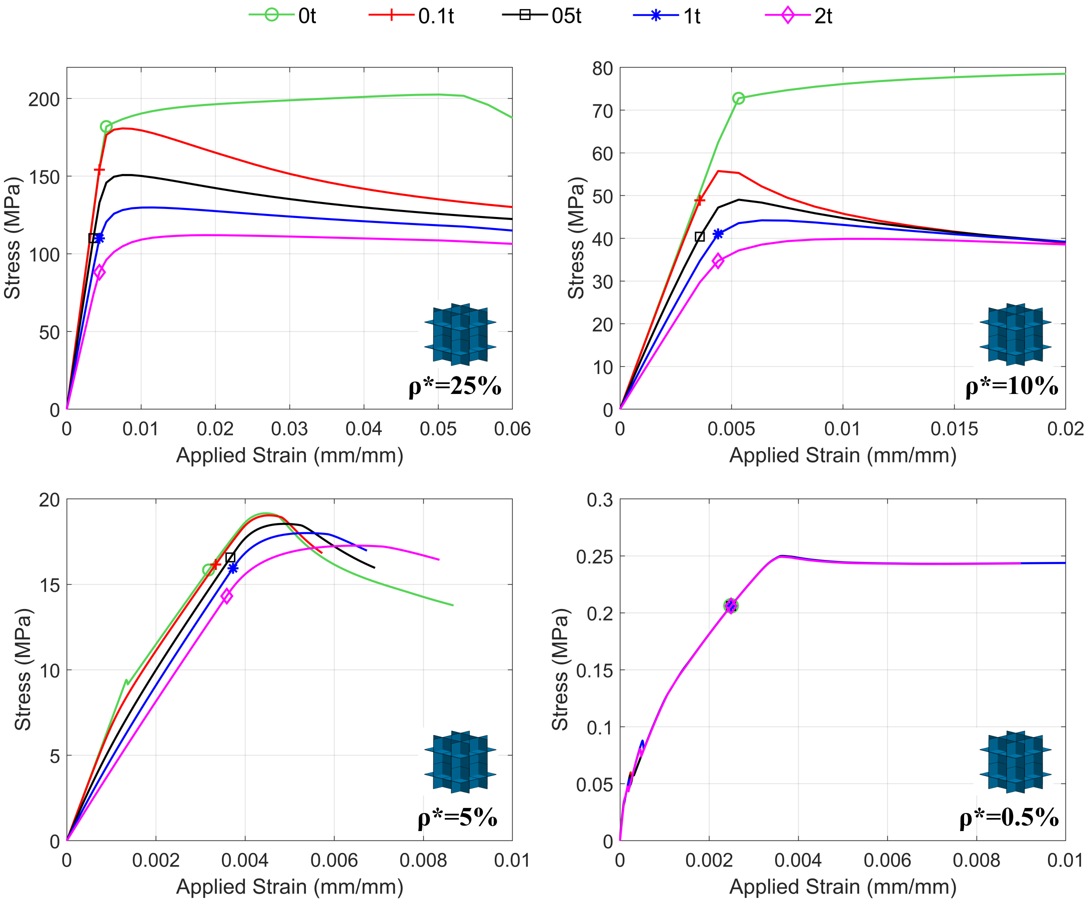

Figure 7.5: Macroscopic stress against applied strain of SC plate-lattices of four relative densities within ρ*=25% and ρ*=0.5% for representation. Markers indicate plasticity initiation for each relative density. Strength and stiffness reduces as relative density decreases. The reduced imperfection impact to the capacity, stiffness and displacement is illustrated as relative density reduces.

Initial stiffness of perfect and imperfect architectures is summarized for all geometries and relative densities in Fig. 7.7, as obtained from the stress-strain curves. Initial stiffness decreases as imperfection amplitude increases for all SC, BCC, FCC, SC-BCC and SC-FCC plate-lattices. Constant stiffness knockdown factors are predicted for all relative densities of each architecture. Furthermore, linear stiffness decrease occurs as relative density decreases for all geometries. SC results to the highest stiffness, while FCC to the lowest initial stiffness for uniaxial compression. Furthermore, displacement at peak load for all plate-lattice architectures and all examined imperfection amplitudes are summarized in Table 7.3 for four relative densities between ρ^*=25% and ρ^*=0.5%.

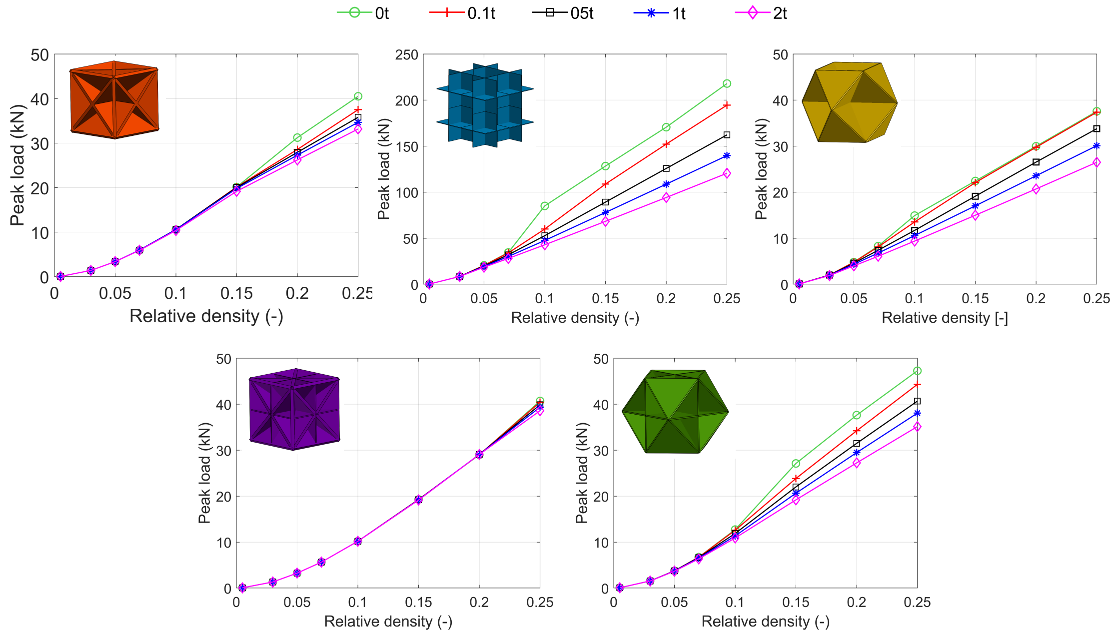

Figure 7.6: Peak load against relative densities within ρ^*=0.5% and ρ^*=25% for all SC, BCC, FCC, SC-BCC and SC-FCC plate-lattice materials of various imperfection amplitudes of $0t$, $0.1t$, $0.5t$, $1t$, $2t$. Nonlinear strength increase is predicted as relative density increases. As plate thicknesses reduce (lower density), a lower imperfection impact is observed.

7.3.2 Failure mechanisms

The failure modes of the different examined plate-lattice architectures vary with relative density and with imperfection amplitude. In general, high-density materials are purely governed by plasticity and bending of the plates, while low-density lattices are governed by elastic buckling followed by plasticity and plate-bending. In all simulations, plasticity is present before the macroscopic peak strength is reached. Deformed shapes of all architectures for the highest and lowest examined relative densities (ρ^*=25% and ρ^*=0.5%, respectively) and imperfection amplitudes (2t and 0t) are illustrated in Fig. 7.8 through von-Mises stress contours.

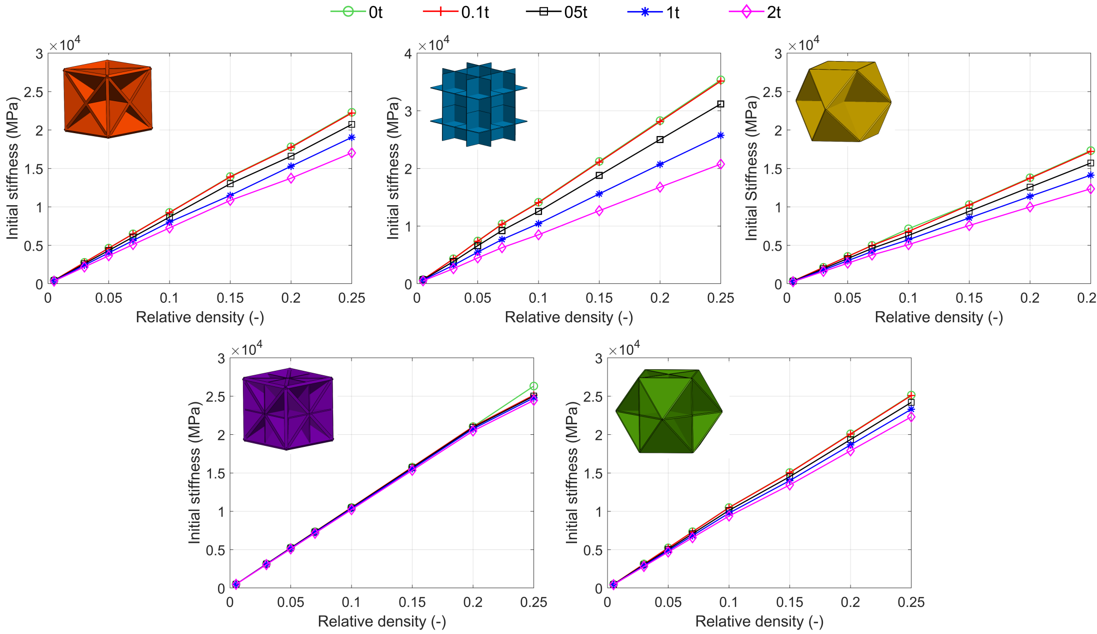

Figure 7.7: Initial stiffness versus relative densities within ρ^*=0.5% and ρ^*=25% for all SC, BCC, FCC, SC-BCC and SC-FCC plate-lattice materials of various imperfection amplitudes of 0t, 0.1t, 0.5t, 1t, 2t. Linear stiffness increase is predicted as relative density increases. As relative density increases, stiffness becomes more imperfection sensitive in comparison to lower densities.

For SC plate-lattices of relative densities between ρ^*=25% and ρ^*=10%, the axial compression and yielding of the vertical plates govern the response of the perfect geometries followed by rotation of the intersections aligned with the loading direction and bending of the plates. All the imperfect architectures for these densities are governed by yielding and bending of the plates in a manner similar to their initial imperfect shapes. For relative densities between ρ^*=7% and ρ^*=5%, perfect SC plate-lattices initially show axial compression and high stress concentration in the vertical plates (in loading direction), which is followed by elastic buckling initiated from the rotation of the top intersections prior to yielding of the plates and bending. Imperfect lattices also show yielding of the plates and large deformation due to rotation of the top intersections. For low (ρ*=3%) and ultra-low (ρ*=0.5%) relative densities, a buckling mode different from the initial imperfection (more waves) governs the response in both perfect and imperfect plate-lattices. The perfect SC plate lattices show high stress concentration in the vertical plates, a first buckling mode similar to the initial imperfection (first jump in stress-strain curves), and different buckling mode/modes (second and/or third jump in stress-strain curves) before the yielding of the plates and the bending and folding mechanism at peak strength.

Similar behavior and progression of failure are observed in all architectures. For FCC plate-lattices of relative densities between ρ*=25% and ρ*=10%, axial compression, and yielding of the plates govern the response of their perfect geometries, while bending on a way similar to the initial imperfection govern the imperfect lattice response. As relative density decreases from ρ*=7% to ρ*=0.5%, the perfect cases failure progression initiates by the high stress concentration in the intersections followed by the rotation of the intersections towards the loading direction and buckling of the triangular plates in a different mode from the initial imperfection (more waves). Plasticity appears after the elastic buckling and before peak load is reached. Since BCC, SC-FCC, and SC-BCC are composed of more plates acting as braces, their plates are thinner for the same relative densities in comparison to SC and FCC. That means that even though progression of failure is similar to the preceding descriptions for the remaining SC-FCC, BCC and SC-BCC plate-lattices, the governing yielding and bending of the plates shift to elastic buckling prior to yielding and bending from relative densities of ρ*=10%, ρ*=15%, ρ*=20% (bifurcation points) and lower for SC-FCC, BCC and SC-BCC, respectively.

Table 7.3: Displacement at peak load for all SC, BCC, FCC, SC-BCC and SC-FCC plate-lattice architectures and all $0t$, $0.1t$. $0.5t$, $1t$ and $2t$ imperfection amplitudes for relative densities within ρ*=25% and ρ*=0.5% (four densities are depicted for representation).

		Displacement at peak load (mm)			
Geometry	Amplitude	ρ*=25%	ρ*=10%	ρ*=5%	ρ*=0.5%
SC	$0t$	1.647	0.825	0.146	0.119
	$0.1t$	0.246	0.144	0.149	0.119
	$0.5t$	0.380	0.174	0.161	0.119
	$1t$	0.246	0.208	0.176	0.119
	$2t$	0.612	0.332	0.213	0.119
BCC	$0t$	0.340	0.186	0.183	0.340
	$0.1t$	0.190	0.185	0.183	0.274
	$0.5t$	0.216	0.186	0.183	0.340
	$1t$	0.244	0.190	0.184	0.274
	$2t$	0.274	0.199	0.191	0.340
FCC	$0t$	0.244	0.144	0.141	0.120
	$0.1t$	0.190	0.144	0.139	0.121
	$0.5t$	0.244	0.144	0.133	0.120
	$1t$	0.340	0.166	0.129	0.120
	$2t$	0.492	0.216	0.128	0.120
SC-BCC	$0t$	0.187	0.157	0.147	0.412
	$0.1t$	0.166	0.157	0.146	0.452
	$0.5t$	0.190	0.160	0.147	0.452
	$1t$	0.190	0.156	0.146	0.375
	$2t$	0.216	0.156	0.147	0.412
SC-FCC	$0t$	0.412	0.108	0.107	0.274
	$0.1t$	0.190	0.110	0.105	0.274
	$0.5t$	0.190	0.106	0.106	0.274
	$1t$	0.190	0.104	0.106	0.274
	$2t$	0.190	0.103	0.106	0.306

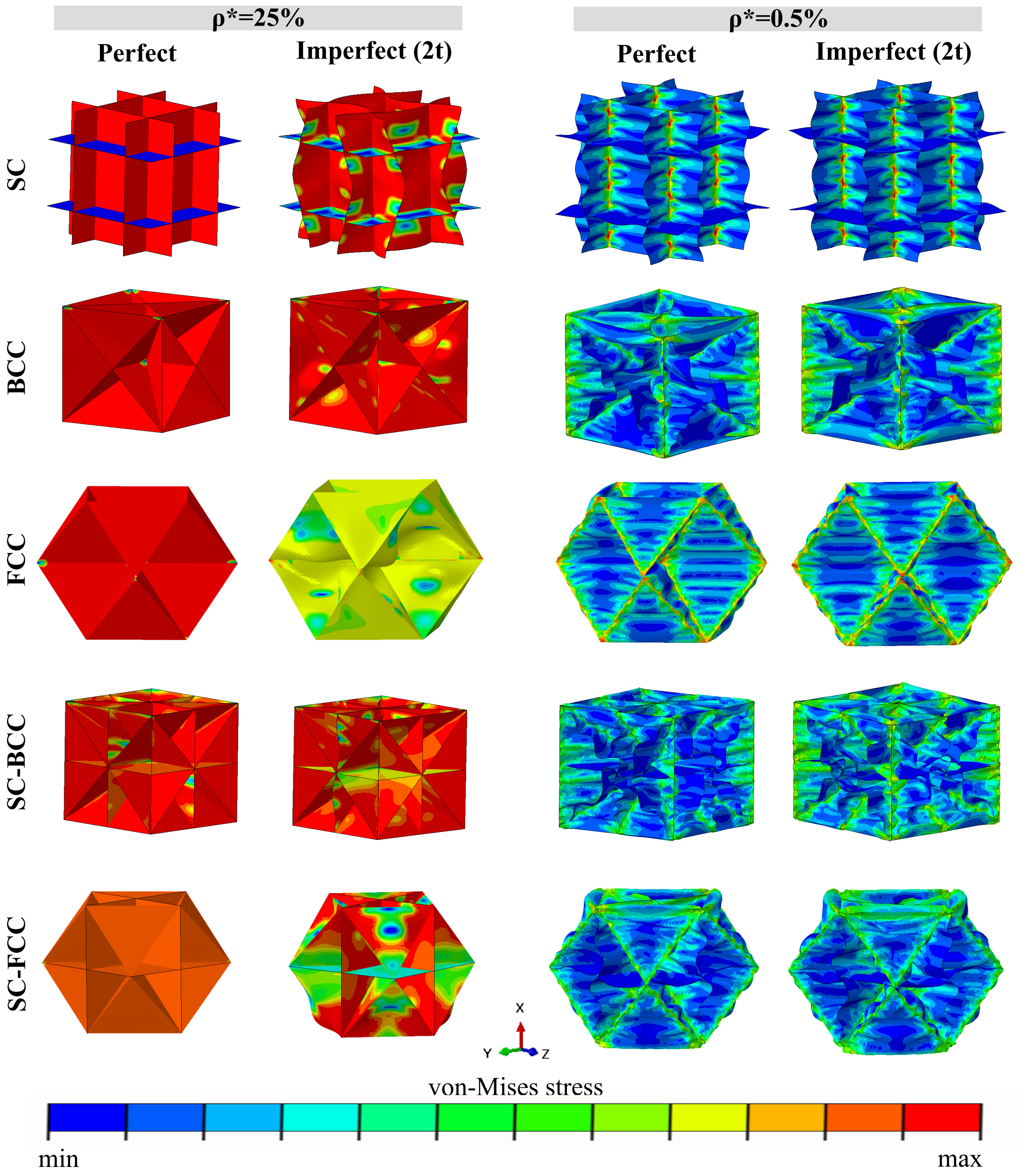

Figure 7.8: Deformed shapes of all SC, BCC, FCC, SC-BCC and SC-FCC plate lattices at peak load. The contours represent von-Mises stresses of each architecture (red: high stress, blue:low stress). The highest examined relative density ρ*=25% and the lowest ρ*=0.5%, as well as the lowest imperfection 0t (perfect) and the highest 2t imperfection, are illustrated herein for representation. Different buckling modes govern the low-density materials (figure scale=5) in comparison to high-density materials (non scaled figures).

7.3.3 Knockdown factors

Innovative knockdown factors are introduced for all examined plate-lattices in Fig. 7.9 in terms of capacity for different slenderness ratios. The slenderness ratio for each geometry is defined as the ratio of length over the minimum plate thickness (L/t), and the knockdown factors are calculated as the ratio of peak strength of imperfect architectures over the peak strength of the perfect lattices (P/P_y). As explained in Section 7.1, as relative density decreases the slenderness ratio increases. The results of all examined plate-lattices (SC, BCC, FCC, SC-BCC, SC-FCC), all relative densities (ρ*=0.5%, ρ*=0.5%, ρ*=0.5%, ρ*=3%, ρ*=5%, ρ*=7%, ρ*=10%, ρ*=15%, ρ*20%, ρ*=25%), and all imperfection amplitudes (0.1t, 0.5t, 1t, 2t) are discussed herein and depicted in Fig. 7.9.

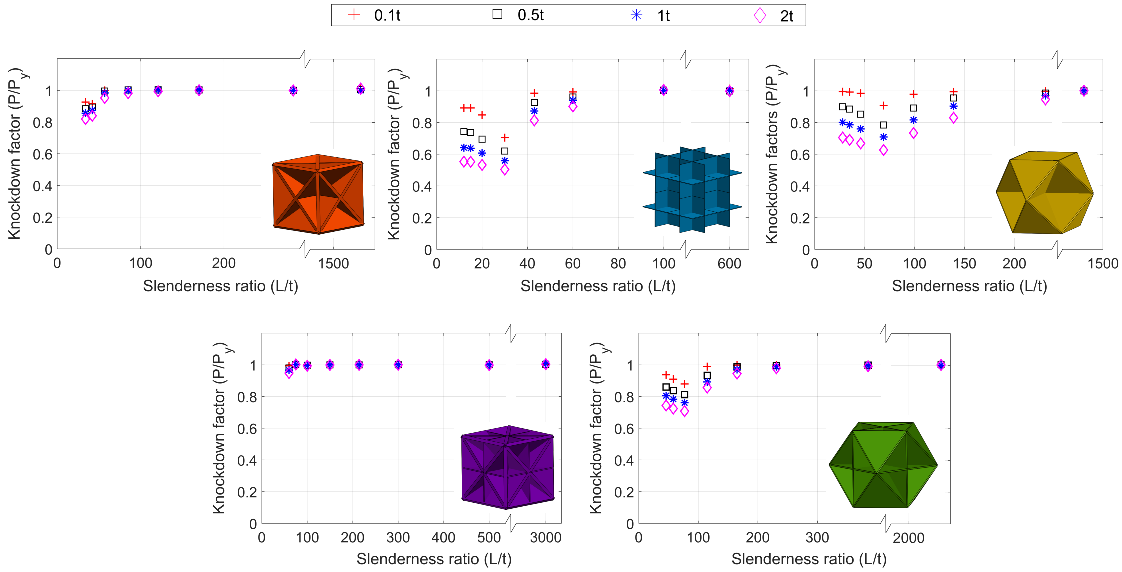

Figure 7.9: Strength Knockdown factors against slenderness ratios of SC, BCC, FCC, SC-BCC and SC-FCC plate-lattices. Summarized knockdowns of various relative densities (ρ*=25%, ρ*=20%, ρ*=15% , ρ*=10%, ρ*=7%, ρ*=5%, ρ*=3% and ρ*=0.5%) and of different imperfection amplitudes (0.1t, 0.5t, 1t, 2t) are illustrated. Plate-lattices indicate imperfection sensitivity for high relative densities, while for low relative densities they become imperfection sensitivity. SC is the most sensitive geometry, and SC-BCC is the most insensitive architecture to geometric imperfections.

Strength knockdown factors for all the examined geometries vary within 0.5 and 1. SC plate-lattice result to the lowest knockdown factors showing the highest imperfection sensitivity, while SC-BCC result to the lowest knockdown factors in comparison to all geometries for higher relative densities. As relative density decreases (slenderness ratio increases) all the geometries become imperfection insensitive. This is the most significant finding of this work which allows SC, BCC, FCC, SC-BCC, SC-FCC plate-lattices to maintain their capacities regardless any geometric imperfections. The change of imperfection sensitive relative densities to imperfection insensitive relative densities lies in the different governing failure modes, as described in Subsection 7.3.2. Given that plate thickness varies for the different geometries of the same relative densities, the bifurcation point of imperfection sensitivity to imperfection insensitivity in all geometries varies.

For SC-plate lattices, knockdown factors decrease from ρ^*=25% to ρ^*=10%, indicating imperfection sensitivity (capacity decreases from $0.1t$ to $2t$). For ρ^*=7% to ρ^*=5%, sensitivity to imperfections is still present, while knockdown factors are increasing (higher than 0.8). For SC plate-lattices of ρ^*=3% to ρ^*=0.5%, knockdown factors are equal to unity which means that their capacity is governed by imperfection insensitivity. Similar behavior is observed for all plate-lattices examined herein. FCC plate-lattices are sensitive to geometric imperfections for ρ^*=25% to ρ^*=3%, while they become imperfection insensitive for ρ^*=0.5%. Imperfection insensitivity appears for SC-FCC plate lattices for relative densities lower than ρ^*=5%, while for BCC imperfection insensitivity is predicted for relative densities lower than ρ^*=7%. SC-BCC becomes imperfection insensitive for relative densities lower than ρ^*=20%, while it is governed by the highest knockdown factors (close to 1) in comparison to all remaining geometries. The knockdown factors of SC-BCC plate-lattices of ρ^*=25% indicate a lowest knockdown factor of 0.95 which is in accordance with Tancogne-

Dejean et al. [103] experimental-to-computational knockdown factor of 0.95 for low strain rate tests. The proposed knockdown factors of plate-latices accounting for plasticity are introduced herein aiming to constitute a benchmark approach of imperfection sensitivity/insensitivity for these structures.

7.3.4 Amplitude and initial imperfection impact

To further examine the impact of imperfection amplitude in the imperfection insensitive relative densities, a constant imperfection amplitude of 2.734 mm (0.108 in.) (equal to $2t$ of ρ*=25%) is applied in SC geometry of ρ*=0.5% (equal to $100t$ of ρ*=0.5%). Fig. 7.10a, illustrates that the examined plate-lattices are imperfection insensitive even for higher imperfection amplitudes relatively to their thicknesses.

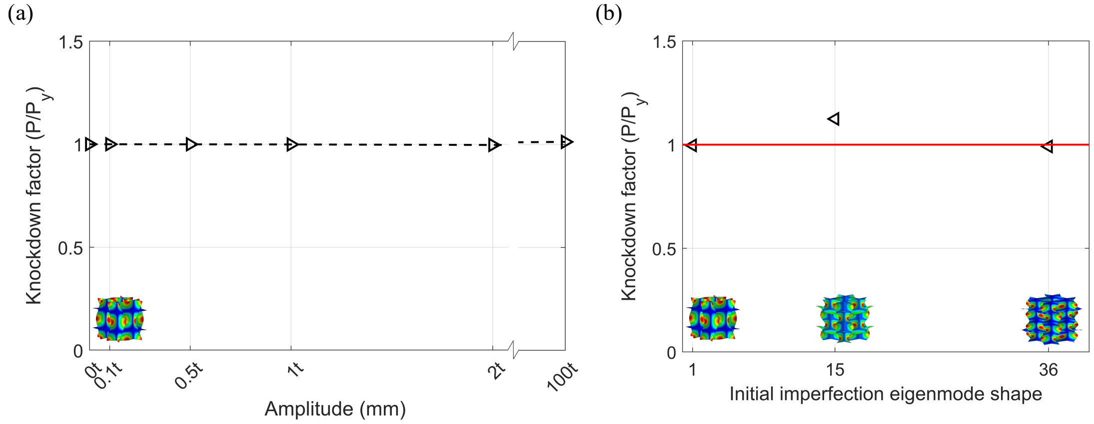

Figure 7.10: Parameter impact to imperfection insensitivity of SC plate-lattice materials of relative density ρ*=0.5%. (a) High amplitude effect ($100t$), and (b) initial imperfection shape effect (eigenmode 15, eigenmode 36) using $2t$ imperfection amplitudes. Imperfection insensitivity is observed for different imperfection amplitudes and different initial imperfections for plate-lattices. Inset figures illustrate the initial imperfection shapes at the different cases.

Furthermore, the impact of different initial imperfections is investigated herein, by selecting a different eigenmode from the Buckle analysis as the initial imperfection. The results of $2t$ imperfection amplitude are illustrated in Fig. 7.10b (corresponding eigenomodes are included as inset figures), showing that SC plate-lattices of ρ*=0.5% maintain their imperfection insensitivity properties regardless the initial imperfection, since the peak strength knockdown is overestimated by 0.52% to 12% for the different examined modes in comparison to first eigenmode.

The main and pioneering finding of this work is that besides high strength and stiffness, closed-cell plate-lattices of cubic symmetry are also insensitive to geometric imperfections. These new properties enhance the superiority of plate-lattices in comparison to other metamaterials, and can benefit not only Materials Science, but also Structural Engineering applications.

8 CONCLUSIONS AND FUTURE WORK: PART II

8.1 Concluding remarks and summary

PART II of this dissertation focused on the elastic and plastic performance, and imperfection sensitivity of plate-lattices mechanical metamaterials. Five periodic closed-cell plate-lattices of relative densities between ρ*=25% and ρ*=0.5% were examined, from which SC, BCC, FCC were the anisotropic geometries and SC-BCC, SC-FCC were the isotropic combinations. The conclusions of this dissertation are pioneering and shed light on new properties of these structures.

8.1.1 Elastic performance of plate-lattices

A shell finite element model was introduced and the periodic plate-lattices subjected to uniaxial compression, shear and biaxial compression were examined to obtain the elastic moduli, while the plate-lattices under uniaxial compression and hydrostatic pressure were investigated to obtain the elastic critical buckling strain.

The examined isotropic SC-BCC and SC-FCC plate-lattices were able to approach, and most importantly achieve the theoretical Hashin-Shtrikman stiffness upper bound for all Young's, shear and bulk moduli for low densities. This renders isotropic plate-lattice mechanical metamaterials as the stiffest materials to date. The normalized elastic moduli of both SC-BCC and SC-FCC resulted to the same stiffness of around 0.50, 0.52 and 0.39 for normalized Young's, shear and bulk modulus, respectively. The anisotropic SC, BCC, and FCC elastic moduli showed that SC normalized Young's modulus was higher than BCC and FCC by around 37% and 52% respectively for all examined relative densities, while SC normalized shear modulus was lower than

BCC and FCC by 62% and 71% respectively. Normalized bulk modulus resulted to the same stiffness of around 0.38 for all geometries and relative densities.

The critical elastic buckling strain based on the first eigenvalue was predicted lower for the isotropic plate-lattice combinations in comparison to anisotropic plate lattices. Specifically, FCC and SC illustrated the highest first eigenvalues, while SC-BCC demonstrated the lowest first eigenvalues for all relative densities between ρ^*=0.5% and ρ^*=25% and for both uniaxial compression and hydrostatic loading. In general, uniaxial compression leaded to higher elastic buckling strains than hydrostatic pressure. The elastic imperfection sensitivity was also approached through normalized eigenvalues for the first 25 eigenmodes. The normalized eigenvalues decreased as relative density increased indicating imperfection sensitivity by varying the relative densities. All the anisotropic SC, BCC and FCC showed higher imperfection sensitivity than the isotropic SC-BCC and SC-FCC between the different relative densities since their normalized eigenvalues varied more with the relative density. Furthermore, SC-BCC and SC-FCC were governed by lower normalized eigenvalues in comparison to SC, BCC, and FCC. Finally, the predicted eigenmodes of all architectures where constant between the different relative densities.

8.1.2 Imperfection sensitivity of plate-lattices

Perfect and imperfect plate-lattices of different imperfection amplitudes were examined under uniaxial compression. The first eigenmodes of the elastic buckling analyses were used as initial imperfections to all SC, BCC, FCC, SC-BCC and SC-FCC, and the $0.1t$, $0.5t$, $1t$ and $2t$ imperfection amplitudes were considered (t is the minimum plate thickness of each geometry). The impact of the constituent material plasticity was also investigated herein.

The peak strength of all the investigated plate-lattice materials reduced with the decrease of relative density from ρ*=25% to ρ*=0.5%. Eight relative densities within this range were selected. Similarly initial stiffness decreased as relative density reduced. The strength decrease was not predicted as linear, while the stiffness decrease was linear. SC was the strongest and stiffest architecture, while SC-BCC was the least strong and stiff geometry. Increased imperfection amplitude indicated strength decrease or constant strength, while demonstrated decreased stiffness. Two failure mechanisms mainly governed the behavior of all SC, BCC, FCC, SC-BCC and SC-FCC: a) the yielding of the plates (primarily those aligned with the loading direction) followed by rotation of the intersections at the loading direction and bending of the plates, and b) the elastic buckling of a mode different from the introduced initial imperfection (after the rotation of the top intersections) followed by the yielding of the plates initiated from the intersections and leading to the plate-lattice bending mechanism. The first case was more pronounced in the higher density ranges, while the second mode was present in the low density ranges. In general, plasticity governed the response of all SC, BCC, FCC, SC-BCC, SC-FCC plate-lattices for all relative densities and all imperfection amplitudes.

The most significant finding of this work was the innovative knockdown factor predictions for all examined plate-lattices. The results demonstrated that all examined plate-lattice architectures were sensitive to imperfections for higher relative densities, while their sensitivity reduced as relative density decreased, and it was finally eliminated for lower relative densities. SC showed the highest sensitivity to imperfections with a knockdown factor of around 0.5 for ρ* higher than 10%, while it became imperfection insensitive for ρ* lower than 3%. FCC followed SC with knockdowns of 0.6 for ρ* higher than 10% and imperfection insensitivity for ρ* equal to 0.5%. SC-FCC become imperfection insensitive for ρ* lower than 5%, while BCC and SC-BCC where the least imperfection sensitive geometries indicating imperfection insensitivity for ρ^* lower than 7% and ρ^* lower than 20% respectively. This was attributed to the topologies of the architectures (more plates leaded to smaller thicknesses) and as a result the different governing failure mechanisms from pure yielding and plate bending for high densities to elastic buckling followed by yielding and bending for the low-densities. Finally, knockdown factors were not affected by the selected imperfection amplitudes, as well as the selected eigenmode shapes of initial imperfections. This study concludes that plate-lattices, besides their high stiffness and strength, are also insensitive to geometric imperfections.

8.2 Future extensions

This work provided a pioneering research mainly focused on the stability and imperfection sensitivity of plate-lattice mechanical metamaterials including plasticity. To expand this research and enhance the current findings, the following future extensions are suggested:

- Investigation of elastic and hyperelastic plate-lattice material stability and imperfection sensitivity is an immediate extension of this work. This will aim to understand the behavior of perfect and imperfect geometries governed mainly by elastic buckling, and provide new knockdown factors. This proposed research, along with the current results of this dissertation, can be used as a benchmark approach to fully characterize the response not only of metal plate-lattices, but also of lattices of various constituent materials, such as polymer.

- Additive manufacturing of perfect and imperfect metal plate-lattice architectures is a future step of this study. This will allow for the investigation of innovative techniques to fabricate closed-cell plate-lattices to experimentally examine and validate the imperfection sensitivity/insensitivity of these structures.

Different imperfections besides modal shapes can be used, such as wavy imperfection or a dimple imperfection, to examine the knockdown effect accounting for both imperfection type and amplitude.

- Introduction of new plate-lattice geometries, closed-cell or open-cell, including appropriate braces to prevent brittle buckling failures or using unique architectural designs to eliminate the imperfection sensitivity is a future extension of this work. New geometries, and specifically open-cell geometries, will advance the experimental investigation of plate-lattices, since additive manufacturing allows for easier 3D printing techniques of open-cell architectures.
- Another future suggestion is the investigation of plate-lattice materials in the nano-scale. Nanolattices follow the ”smaller is stronger” concept, and can offer multiple advantages and superior properties in comparison to bigger scale materials. The investigation of the size effect in plate-lattices will allow for comparisons with different lattice architectures, such as truss-lattices, of a variety of relative densities tackling the strength, stiffness, energy absorption, and stability of ultra-thin architectures.
- Structural hierarchy, as in Eiffel Tower, is another promising future recommendation that can be triggered to enhance the mechanical performance of various structural applications. Hierarchically-structured nanometric or micrometric plate-lattices can offer superior and unique properties, such as recoverability, and can reinforce the potential of the upscaling of these structures. This will benefit both, Materials Science literature and Structural Engineering design.
- Interdisciplinary goals between Structural Engineering and Materials Engineering can be also achieved by combining and expanding the findings of this dissertation. For example, plate-lattice materials can replace the critical fasteners

between CFS and sheathing in cold-formed steel wall construction, and provide higher wall capacity, higher wall stiffness, and higher wall and connection energy absorption capacity under earthquake or wind loading. Furthermore, the extraordinary plate-lattice material properties, including their imperfection insensitivity, will allow for innovative infrastructure repair solutions.

To conclude, this dissertation is the first research effort of tackling the imperfection sensitivity of various plate-lattice materials focusing in low-density materials and providing knockdown factors. As a result, its expansion will benefit different engineering fields through new and more advantageous materials and methods than the common state-of-the-art options.

A APPENDIX

This Appendix includes the connection test rig and specimen in the INSTRON machine, illustrating an OSB-sheathed specimen (Fig. A.1). The test rig illustrated herein is used for all relevant connection test configurations. The different screw types a and b are also pictured indicating their differences, and photographs of FCB- and SG-sheathed connection specimens are included for representation after testing.

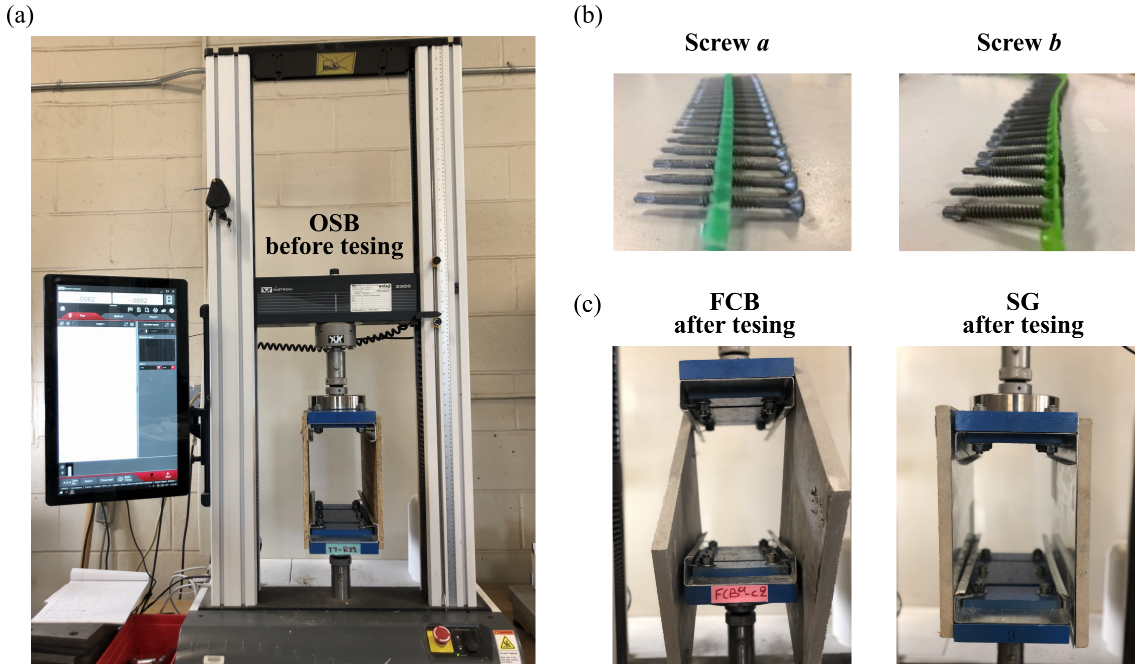

Figure A.1: Experimental connection test configuration and components. (a) Test rig and stud-screw-sheathing specimen located in INSTRON machine before testing. OSB sheathing is illustrated in the photograph for representation. (b) Examined self-drilling screw types indicating the screw length, head and thread differences between screw a and b. (c) Pictures of actual specimens (FCB and SG) after testing illustrating the failure of the connections either due to screw pull-through or shear screw failure.

This Appendix also includes the converted system to individual screw test results of the 30 identical specimens (using Eq. 1, Eq. 2, Eq. 3 from Chapter 2), as well as tensile coupon tests of studs used in specimens failed by both pull-through and shear failure (three repetitions each) in Fig. A.2.

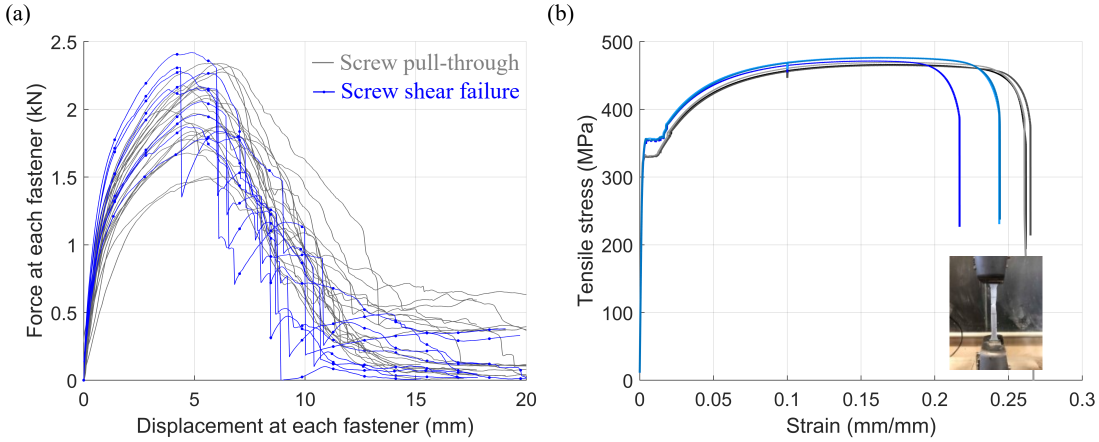

Figure A.2: Experimental results and failure indication. (a) Single screw test results of the 30 identical tests, and (b) tensile CFS coupon stud testing (in total 9 tests). Grey-colored lines indicate specimens failed by screw pull-through, while blue-colored lines indicate specimens failed by shear screw failure.

The following acronyms are used in PART I of this dissertation:

BC – Boundary Condition,

CFS – Cold-Formed Steel,

FCB – Fiber Cement Board,

FE – Finite Element method,

MC – Monte Carlo simulation,

MPC – Multi-Point Constraint,

OSB – Oriented Strand Board,

RP – Reference Point, and

SG – Steel-Gypsum board.

The following symbols and notation are used in PART I of this dissertation:

B = stud and track flange width (mm),

COV = coefficient of variation of connection response (%),

CTF_1 = connection total force at direction 1 in ABAQUS (kN),

CTF_2 = connection total force at direction 2 in ABAQUS (kN),

CTF_3 = connection total force at direction 3 in ABAQUS (kN),

D = stud and track lip depth (mm),

E = Young's modulus of CFS (MPa),

E_s = Young's modulus of OSB sheathing (MPa),

E_{s1} = Young's modulus of OSB sheathing // to strength axis (MPa),

E_{s2} = Young's modulus of OSB sheathing $\perp$ to strength axis (MPa),

E_{s3} = out-of-plane Young's modulus of OSB sheathing (MPa),

$(EI)_s$ = panel bending stiffness ($kN - mm^2/mm$),

eNd_i = connection backbone displacement in negative branch (mm),

eNf_i = connection backbone load in negative branch (kN),

ePd_i = connection backbone displacement in positive branch (mm),

eNf_i = connection backbone load in positive branch (kN),

G_s = shear modulus of OSB sheathing (MPa),

G_{s12} = shear modulus of OSB sheathing through thickness (MPa),

G_{s13} = out-of-plane shear modulus of OSB sheathing (MPa),

G_{s23} = out-of-plane shear modulus of OSB sheathing (MPa),

$(Gt)_s$ = panel rigidity (kN/mm),

H = stud and track web depth (mm),

h = shear wall height (m),

K = stud-screw-sheathing specimen stiffness (kN/m),

K_i = individual screw stiffness (kN/m),

K_{secant} = FE model secant stiffness at 0-100% peak load (kN/m),

$K_{initial}$ = FE model initial stiffness at 0-40% peak load (kN/m),

K_{middle} = FE model middle stiffness at 40-80% peak load (kN/m),

K_{final} = FE model final stiffness at 80-100% peak load (kN/m),

P = stud-screw-sheathing specimen force (kN),

P_i = individual screw force (kN),

P_1 = individual screw force at 40% peak load (kN),

P_2 = individual screw force at 80% peak load (kN),

P_3 = individual screw force at 100% peak load (kN),

P_4 = individual screw force at 30% post peak load (kN),

$rDispN$ = reloading screw displacement parameter in negative branch (mm),

$rDispP$ = reloading screw displacement parameter in positive branch (mm),

$rForceN$ = reloading screw force parameter in negative branch (kN),

$rForceP$ = reloading screw force parameter in positive branch (kN),

s = screw spacing at stud-screw-sheathing tests (mm),

s_p = screw spacing at shear wall perimeter (mm),

s_f = screw spacing at shear wall field stud (mm),

t_1 = stud thickness (mm),

t_2 = track thickness (mm),

t_s = sheathing thickness (mm),

$uForceN$ = unloading screw force parameter in negative branch (kN),

$uForceP$ = unloading screw force parameter in positive branch (kN),

w = shear wall width (m),

Δ = stud-screw-sheathing specimen and reference displacement (mm),

Δ_i = individual screw displacement (mm),

Δ_m = screw monotonic displacement at 80% post-peak load (mm),

Δ_1 = individual screw displacement at 40% peak load (mm),

Δ_2 = individual screw displacement at 80% peak load (mm),

Δ_3 = individual screw displacement at 100% peak load (mm),

Δ_4 = individual screw displacement at 30% post peak load (mm),

θ = connection local coordinate system angle calculation,

μ = mean connection response (mm or kN),

ν = Poisson's ratio of CFS,

ν_s = Poisson's ratio of OSB sheathing,

σ = standard deviation of connection response (mm or kN), and

σ_y = yield strength of CFS members (MPa).

B APPENDIX

This Appendix includes the resulted relative density calculations, as adapted by Tancogne-Dejean et al. [102], for all SC, BCC, FCC, SC-BCC, and SC-FCC plate-lattice architected materials. Eq. 21, Eq. 22, Eq. 23, Eq. 24 and Eq. 25 are used to calculate all respective ρ^* based on t_{SC}, t_{BCC} and t_{FCC} plate thicknesses of SC plates, BCC plates and FCC plates respectively and the constant side length L. These equations are used along with Eq. 18 and Eq. 19 for the isotropic combinations.

The relative density of SC plate-lattices is calculated as:

$$\rho^* = 3\frac{t_{SC}}{L} \tag{21}$$

The relative density of BCC plate-lattices is obtained as:

$$\rho^* = 6\sqrt{2}\frac{t_{BCC}}{L} \tag{22}$$

The relative density of FCC plate-lattices is defined as:

$$\rho^* = 4\sqrt{3}\frac{t_{FCC}}{L} \tag{23}$$

The relative density of SC-BCC plate-lattices is obtained as:

$$\rho^* = 15\frac{t_{SC}}{L} \tag{24}$$

The relative density of SC-FCC plate-lattices is calculated as:

$$\rho^* = 7.5\frac{t_{SC}}{L} \tag{25}$$

This Appendix also includes the stress-strain curves of BCC, FCC, SC-BCC and SC-FCC plate-lattices (similarly to SC in Chapter 7) for ρ^*=25%, ρ^*=10%, ρ^*=5%, ρ^*=0.5% (four out of eight densities for representation) and for $0t$, $0.1t$, $0.5t$ and $2t$ imperfection amplitudes. Fig. B.1, Fig. B.2, Fig. B.3, Fig. B.4 (along with Fig. 7.5) indicate the strength, stiffness and imperfection sensitivity decrease as relative density decreases for all examined plate-lattices.

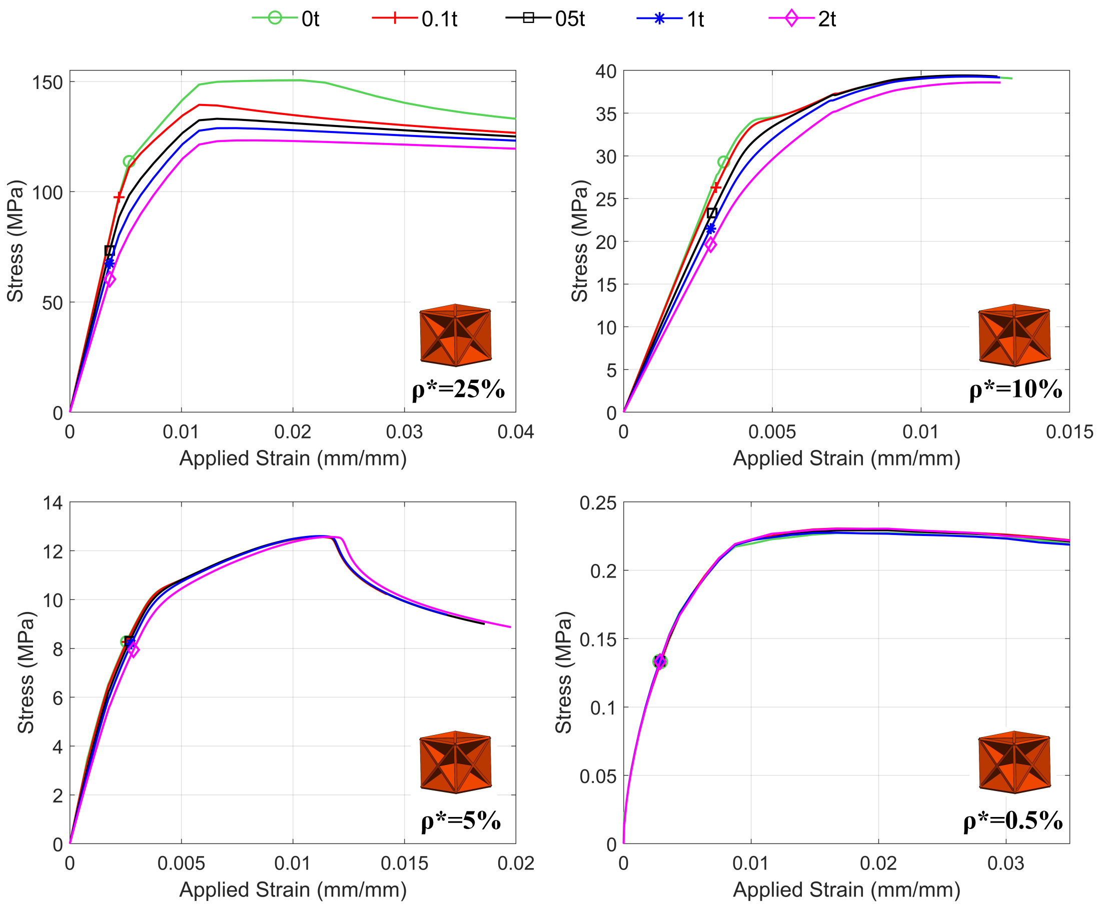

Figure B.1: Macroscopic stress against applied strain of BCC plate-lattices of four relative densities within ρ^*=25% and ρ^*=0.5% for representation. Strength and stiffness reduces as relative density decreases. The reduced imperfection impact to the capacity, stiffness and displacement is illustrated as relative density reduces.

Plasticity appears before the peak load is reached for all plate-lattice architectures herein and for all examined relative densities and imperfection amplitudes. The graphs in this Appendix can be used to compare strength and stiffness between the different geometries, indicating that SC is the strongest and stiffest of the geometries, while SC-BCC has the lowest strength and stiffness in comparison to the remaining geometries for uniaxial compression.

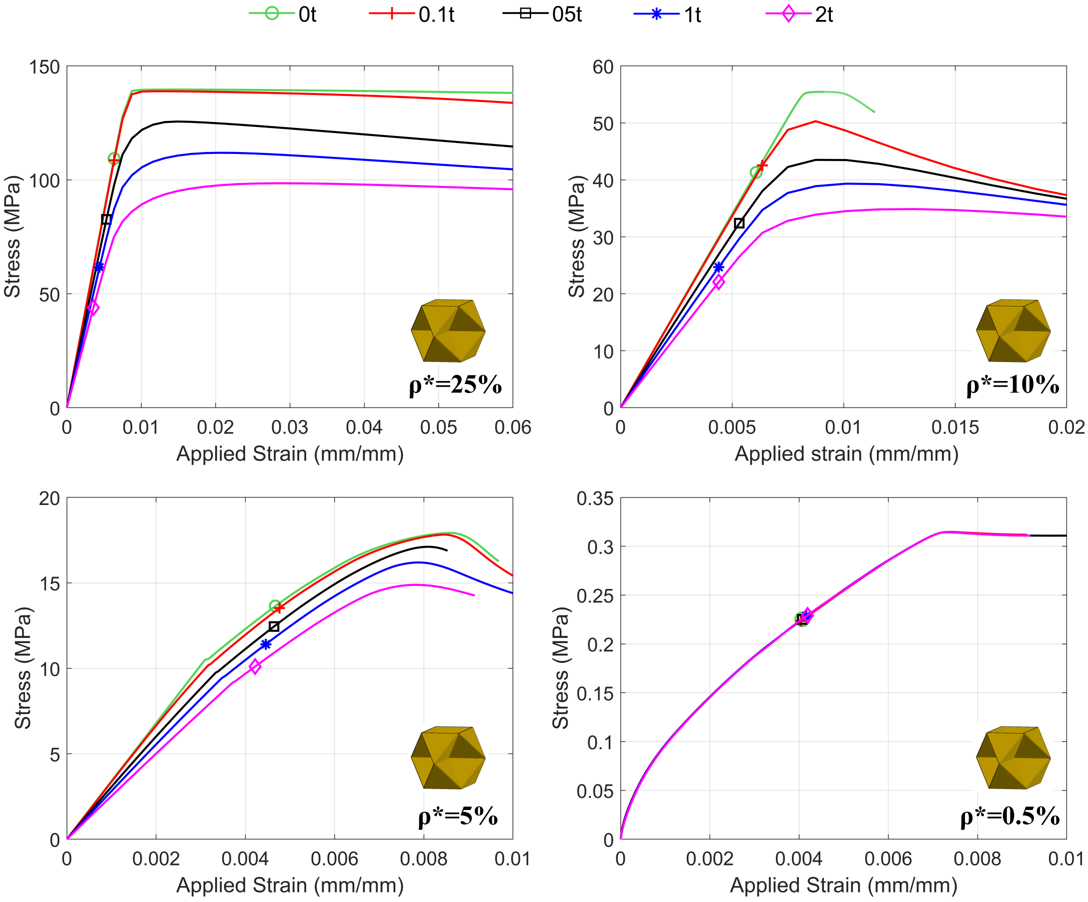

Figure B.2: Macroscopic stress against applied strain of FCC plate-lattices of four relative densities within ρ*=25% and ρ*=0.5% for representation. Strength and stiffness reduces as relative density decreases. The reduced imperfection impact to the capacity, stiffness and displacement is illustrated as relative density reduces.

The isotropic SC-BCC and SC-FCC plate-lattices indicate less imperfection sensitivity than their constituent SC, BCC and FCC plate-lattices even for higher relative densities. As shown in these stress-strain curves SC-BCC is the least sensitive plate-lattice to geometric imperfections in comparison to the remaining examined geometries.

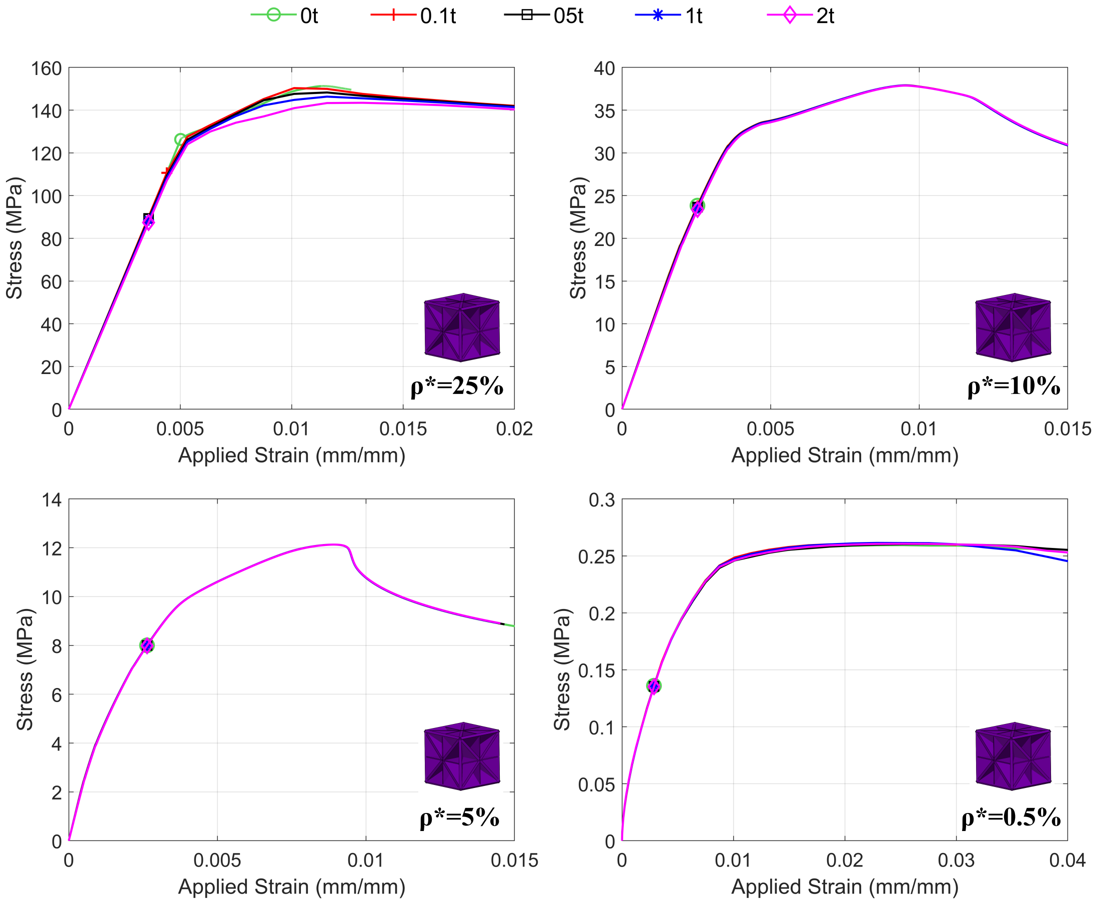

Figure B.3: Macroscopic stress against applied strain of SC-BCC plate-lattices of four relative densities within ρ^*=25% and ρ^*=0.5% for representation. Strength and stiffness reduces as relative density decreases. The reduced imperfection impact to the capacity, stiffness and displacement is illustrated as relative density reduces.

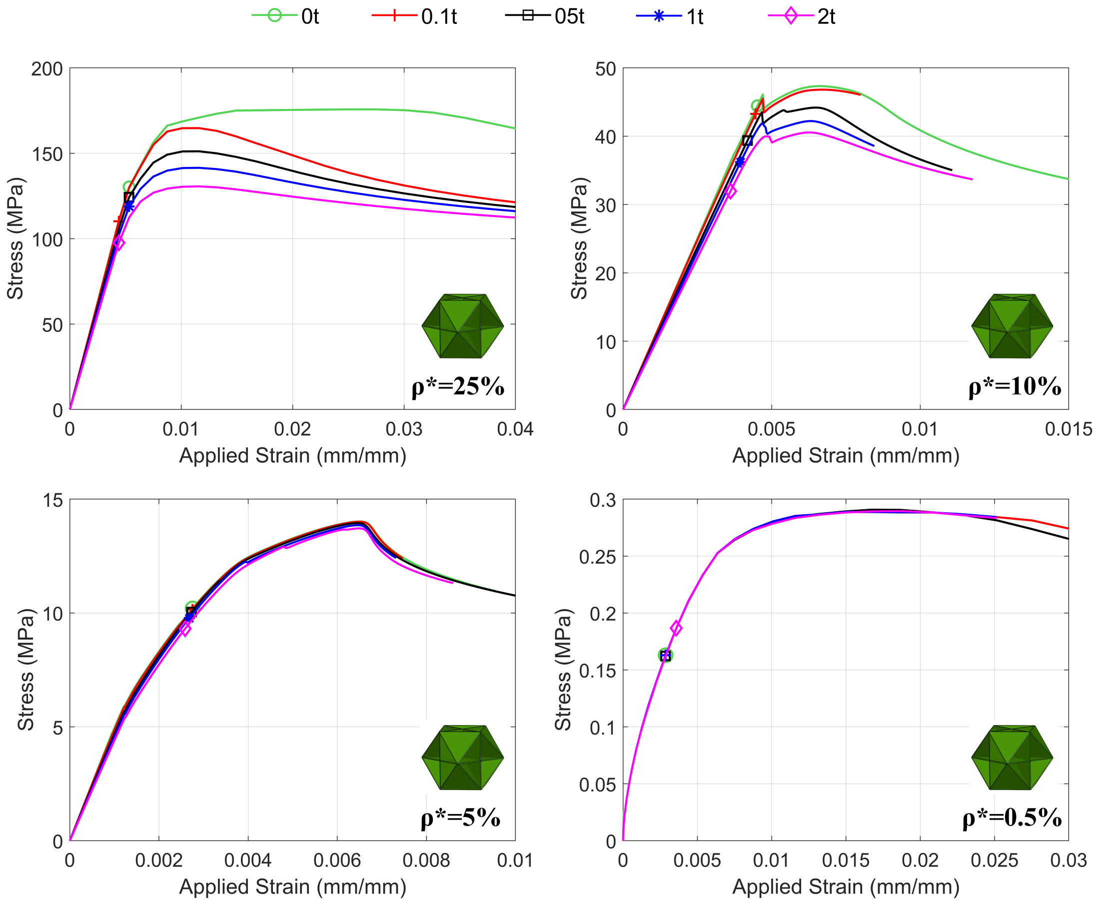

Figure B.4: Macroscopic stress against applied strain of SC-FCC plate-lattices of four relative densities within ρ*=25% and ρ*=0.5% for representation. Strength and stiffness reduces as relative density decreases. The reduced imperfection impact to the capacity, stiffness and displacement is illustrated as relative density reduces.

The following acronyms are used in PART II of this dissertation:

BCC – Body-Centered Cubic,

FCC – Face-Centered Cubic,

HS – Hashin-Shtrikman bound,

PBC – Periodic Boundary Conditions,

SC – Simple Cubic,

SC-BCC – Simple Cubic and Body-Centered Cubic, and

SC-FCC – Simple Cubic and Face-Centered Cubic.

The following symbols and notation are used in PART II of this dissertation:

C = elastic stiffness tensor,

C_i = elastic constants of the stiffness tensor,

E = Young's modulus of plate-lattice materials (GPa),

E_{HS} = Hashin-Shtrikman Young's modulus upper bound (GPa),

E_s = Young's modulus of solid phase of materials (GPa),

G = shear modulus of plate-lattice materials (GPa),

G_{HS} = Hashin-Shtrikman shear modulus upper bound (GPa),

G_s = shear modulus of solid phase of materials (GPa),

G_v = shear modulus of void phase of materials (GPa),

K = bulk modulus of plate-lattice materials (GPa),

K_{HS} = Hashin-Shtrikman bulk modulus upper bound (GPa),

K_s = bulk modulus of solid phase of materials (GPa),

K_v = bulk modulus of void phase of materials (GPa),

L = side length of plate-lattices (mm),

P = peak load of perfect plate-lattices (kN),

P_y = peak load of perfect plate-lattices (kN),

T = time period (sec),

t = minimum thickness of combined plate-lattices (mm),

t_{BCC} = plate thickness of FCC plate-lattices (mm),

t_{FCC} = plate thickness of BCC plate-lattices (mm),

t_{SC} = plate thickness of SC plate-lattices (mm),

V = volume of the whole unit-cell (mm^3),

V_s = volume of solid phase of materials (mm^3),

λ = eigenvalue of plate-lattices,

λ_1 = first eigenvalue (critical buckling strain),

ν = Poisson's ratio of constituent material,

ν_{HS} = Hashin-Shtrikman Poisson's ratio,

ρ = density of 316L stainless steel (g/cm^3)

ρ^* = relative density,

σ_y = yield strength of base material (MPa), and

ζ = Zener ratio of isotropic plate-lattices.

References

[1] ABAQUS (2014). Abaqus theory guide. In *Version 6.14*. Dassault Systems Simulia Corp, USA.

[2] ABAQUS (2018). Abaqus theory guide. In *Version 6.18*. Dassault Systems Simulia Corp, USA.

[3] AISI-S100-16 (2016). North american specification for the design of cold-formed steel structural members. In *AISI-S100*. American Iron and Steel Institute, Washington, D.C.

[4] AISI-S200-12 (2012). North american specification for cold-formed steel framing - general provisions. In *AISI-S200*. American Iron and Steel Institute, Washington, D.C.

[5] AISI-S400-15 (2015). North american standard for seismic design of cold-formed steel structural systems. In *AISI-S400*. American Iron and Steel Institute, Washington, D.C.

[6] Al-Ketan, O., Assad, M. A., and Al-Rub, R. K. A. (2017). Mechanical properties of periodic interpenetrating phase composites with novel architected microstructures. *Composite Structures*, 176:9–19.

[7] Altoontash, A. (2004). *Simulation and damage models for performance assessment of reinforced concrete beam-column joints.* PhD thesis, Stanford university Stanford, California.

[8] APA (2012). Panel design specification. In *APA-D510C*. The Engineered Wood Association, Tacoma, WA.

[9] Ashby, M. F. (2010). *Materials Selection in Mechanical Design.* Fourth Edition, Butterworth Heinemann, Oxford.

[10] Bauer, J., Hengsbach, S., Tesari, I., Schwaiger, R., and Kraft, O. (2014). High-strength cellular ceramic composites with 3d microarchitecture. *Proceedings of the National Academy of Sciences*, 111(7):2453–2458.

[11] Bauer, J., Meza, L. R., Schaedler, T. A., Schwaiger, R., Zheng, X., and Valdevit, L. (2017). Nanolattices: an emerging class of mechanical metamaterials. *Advanced Materials*, 29(40):1701850.

[12] Berger, J., Wadley, H., and McMeeking, R. (2017). Mechanical metamaterials at the theoretical limit of isotropic elastic stiffness. *Nature*, 543(7646):533–537.

[13] Bian, G., Chatterjee, A., Buonopane, S. G., Arwade, S. R., Moen, C. D., and Schafer, B. W. (2017). Reliability of cold-formed steel framed shear walls as impacted by variability in fastener response. *Engineering Structures*, 142:84–97.

[14] Bian, G., Padilla-Llano, D., Leng, J., Buonopane, S., Moen, C., and Schafer, B. (2015). Opensees modeling of cold-formed steel framed wall system. In *Proceedings of 8th International Conference on Behavior of Steel Structures in Seismic Areas.*

[15] Blais, C. (2006). Testing and analysis of light gauge steel frame/9 mm osb panel shear walls. M.Eng. thesis, McGill University, Montreal, Canada.

[16] Bonatti, C. and Mohr, D. (2019a). Mechanical performance of additively-manufactured anisotropic and isotropic smooth shell-lattice materials: Simulations & experiments. *Journal of the Mechanics and Physics of Solids*, 122:1–26.

[17] Bonatti, C. and Mohr, D. (2019b). Smooth-shell metamaterials of cubic symmetry: anisotropic elasticity, yield strength and specific energy absorption. *Acta Materialia*, 164:301–321.

[18] Branston, A. E. (2004). Development of a design methodology for steel frame/wood panel shear walls. M.Eng. thesis, McGill University, Montreal, Canada.

[19] Branston, A. E., Chen, C. Y., Boudreault, F. A., and Rogers, C. A. (2006). Testing of light-gauge steel-frame - wood structural panel shear walls. *Canadian Journal of Civil Engineering*, 33(5):561 – 572.

[20] Buonopane, S., Bian, G., Tun, T., and Schafer, B. (2015). Computationally efficient fastener-based models of cold-formed steel shear walls with wood sheathing. *Journal of Constructional Steel Research*, 110:137–148.

[21] Campbell, M., Sharp, D., Harrison, M., Denning, R., and Turberfield, A. (2000). Fabrication of photonic crystals for the visible spectrum by holographic lithography. *Nature*, 404(6773):53–56.

[22] Castaneda, H. and Peterman, K. D. (2021). Moment-rotation response of cold-formed steel joist-to-ledger connections with variable-finishes in ledger-framed construction. *Journal of Constructional Steel Research*, 176:106396.

[23] Chen, C., Lu, T., and Fleck, N. (1999). Effect of imperfections on the yielding of two-dimensional foams. *Journal of the Mechanics and Physics of Solids*, 47(11):2235–2272.

[24] Chen, C. Y. (2004). Testing and performance of steel frame / wood panel shear walls. M.Eng. thesis, McGill University, Montreal, Canada.

[25] Chen, Z., Xie, Y. M., Wu, X., Wang, Z., Li, Q., and Zhou, S. (2019). On hybrid cellular materials based on triply periodic minimal surfaces with extreme mechanical properties. *Materials & Design*, 183:108109.

[26] Crook, C., Bauer, J., Izard, A. G., de Oliveira, C. S., e Silva, J. M. d. S., Berger, J. B., and Valdevit, L. (2020). Plate-nanolattices at the theoretical limit of stiffness and strength. *Nature communications*, 11(1):1–11.

[27] DaBreo, J., Balh, N., Ong-Tone, C., and Rogers, C. (2014). Steel sheathed cold-formed steel framed shear walls subjected to lateral and gravity loading. *Thin-Walled Structures*, 74:232–245.

[28] Derveni, F., Gerasimidis, S., and Peterman, K. D. (2019). Capturing cold-formed steel shear wall behavior through nonlinear fastener-based modeling. In *Proceedings of the SSRC Stability Conference, St. Louis, Missouri*.

[29] Derveni, F., Gerasimidis, S., and Peterman, K. D. (2020a). Behavior of cold-formed steel shear walls sheathed with high-capacity sheathing. *Engineering Structures*, 225:111280.

[30] Derveni, F., Gerasimidis, S., and Peterman, K. D. (2020b). Impact of fastener spacing on the behavior of cold-formed steel shear walls sheathed with fiber cement board.

[31] Derveni, F., Gerasimidis, S., and Peterman, K. D. (2020c). Nonlinear fastener-based modeling of cold-formed steel shear walls. In *Structures Congress 2020*, pages 697–708. American Society of Civil Engineers Reston, VA.

[32] Derveni, F., Gerasimidis, S., Schafer, B. W., and Peterman, K. D. (2021a). High-fidelity finite element modeling of wood-sheathed cold-formed steel shear walls. *Journal of Structural Engineering*, 147(2):04020316.

[33] Derveni, F., Gross, A. G., Peterman, K. D., and Gerasimidis, S. (2021b). Imperfection sensitivity of metallic plate-lattice materials. In *Proceedings of the SSRC Stability Conference*.

[34] Deshpande, V., Ashby, M., and Fleck, N. (2001a). Foam topology: bending versus stretching dominated architectures. *Acta materialia*, 49(6):1035–1040.

[35] Deshpande, V. and Fleck, N. (2000). High strain rate compressive behaviour of aluminium alloy foams. *International Journal of Impact Engineering*, 24(3):277–298.

[36] Deshpande, V. S., Fleck, N. A., and Ashby, M. F. (2001b). Effective properties of the octet-truss lattice material. *Journal of the Mechanics and Physics of Solids*, 49(8):1747–1769.

[37] Ding, C. (2015). Monotonic and cyclic simulation of screw-fastened connections for cold-formed steel framing. M.S. thesis, Virginia Tech, Blacksburg, VA.

[38] Duan, S., Wen, W., and Fang, D. (2020). Additively-manufactured anisotropic and isotropic 3d plate-lattice materials for enhanced mechanical performance: Simulations & experiments. *Acta Materialia*, 199:397–412.

[39] Elsayed, M. S. and Pasini, D. (2010). Multiscale structural design of columns made of regular octet-truss lattice material. *International Journal of Solids and Structures*, 47(14-15):1764–1774.

[40] Fiorino, L., Della Corte, G., and Landolfo, R. (2007). Experimental tests on typical screw connections for cold-formed steel housing. *Engineering Structures*, 29(8):1761–1773.

[41] Fiorino, L., Macillo, V., and Landolfo, R. (2017a). Experimental characterization of quick mechanical connecting systems for cold-formed steel structures. *Advances in Structural Engineering*, 20(7):1098–1110.

[42] Fiorino, L., Macillo, V., and Landolfo, R. (2017b). Shake table tests of a full-scale two-story sheathing-braced cold-formed steel building. *Engineering Structures*, 151:633–647.

[43] Fiorino, L., Pali, T., Bucciero, B., Macillo, V., Terracciano, M. T., and Landolfo, R. (2017c). Experimental study on screwed connections for sheathed cfs structures with gypsum or cement based panels. *Thin-Walled Structures*, 116:234–249.

[44] Fiorino, L., Shakeel, S., Macillo, V., and Landolfo, R. (2018). Seismic response of cfs shear walls sheathed with nailed gypsum panels: Numerical modelling. *Thin-Walled Structures*, 122:359–370.

[45] Fleck, N. A., Deshpande, V. S., and Ashby, M. F. (2010). Micro-architectured materials: past, present and future. *Proceedings of the Royal Society A: Mathematical, Physical and Engineering Sciences*, 466(2121):2495–2516.

[46] Fülöp, L. A. and Dubina, D. (2004). Performance of wall-stud cold-formed shear panels under monotonic and cyclic loading: Part ii: Numerical modelling and performance analysis. *Thin-Walled Structures*, 42(2):339–349.

[47] Gerasimidis, S., Virot, E., Hutchinson, J., and Rubinstein, S. (2018). On establishing buckling knockdowns for imperfection-sensitive shell structures. *Journal of Applied Mechanics*, 85(9).

[48] Gibson, I. and Ashby, M. F. (1982). The mechanics of three-dimensional cellular materials. *Proceedings of the Royal Society of London. A. Mathematical and Physical Sciences*, 382(1782):43–59.

[49] Gibson, L. J., Ashby, M. F., Schajer, G., and Robertson, C. (1982). The mechanics of two-dimensional cellular materials. *Proceedings of the Royal Society of London. A. Mathematical and Physical Sciences*, 382(1782):25–42.

[50] Green, G. G., Winter, G., and Cuykendall, T. R. (1947). *Light gage steel columns in wall-braced panels*. Cornell Univ.

[51] Gross, A., Pantidis, P., Bertoldi, K., and Gerasimidis, S. (2019). Correlation between topology and elastic properties of imperfect truss-lattice materials. *Journal of the Mechanics and Physics of Solids*, 124:577–598.

[52] Gu, X. W. and Greer, J. R. (2015). Ultra-strong architected cu meso-lattices. *Extreme Mechanics Letters*, 2:7–14.

[53] Gypsum Association (2019). Gypsum board typical mechanical and physical properties. *GA 235*, 10.

[54] Han, S. C. and Kang, K. (2019). Another stretching-dominated micro-architectured material, shellular. *Materials Today*, 31:31–38.

[55] Han, S. C., Lee, J. W., and Kang, K. (2015). A new type of low density material: Shellular. *Advanced Materials*, 27(37):5506–5511.

[56] Hashin, Z. and Shtrikman, S. (1963). A variational approach to the theory of the elastic behaviour of multiphase materials. *Journal of the Mechanics and Physics of Solids*, 11(2):127–140.

[57] Hikita, K. (2006). Impact of gravity loads on the lateral performance of light gauge steel frame/wood panel shear walls. M.Eng. thesis, McGill University, Montreal, Canada.

[58] Hoehler, M. S., Smith, C. M., Hutchinson, T. C., Wang, X., Meacham, B. J., and Kamath, P. (2017). Behavior of steel-sheathed shear walls subjected to seismic and fire loads. *Fire safety journal*, 91:524–531.

[59] Hutchinson, T., Wang, X., Hegemier, G., Meacham, B., and Kamath, P. (2018). Physical damage evolution during earthquake and post-earthquake fire testing of a mid-rise cold-formed steel framed building. In *Proceedings of the 11th US National Conference on Earthquake Engineering*.

[60] Iuorio, O., Fiorino, L., and Landolfo, R. (2014). Testing cfs structures: The new school bfs in naples. *Thin-walled structures*, 84:275–288.

[61] Jacobsen, A. J., Barvosa-Carter, W., and Nutt, S. (2007). Micro-scale truss structures formed from self-propagating photopolymer waveguides. *Advanced Materials*, 19(22):3892–3896.

[62] Kader, M., Hazell, P., Brown, A., Tahtali, M., Ahmed, S., Escobedo, J., and Saadatfar, M. (2020). Novel design of closed-cell foam structures for property enhancement. *Additive Manufacturing*, 31:100976.

[63] Kechidi, S. and Bourahla, N. (2016). Deteriorating hysteresis model for cold-formed steel shear wall panel based on its physical and mechanical characteristics. *Thin-Walled Structures*, 98:421–430.

[64] Khaliq, W. and Moghis, A. (2017). Shear capacity of cold-formed light-gauge steel framed shear-wall panels with fiber cement board sheathing. *International Journal of Steel Structures*, 17(4):1404–1414.

[65] Krawinkler, H., Parisi, F., Ibarra, L., Ayoub, A., and Medina, R. (2000). Development of a testing protocol for wood frame structures, curee publication no. *W-02, California*.

[66] Lee, D.-W., Khan, K. A., and Al-Rub, R. K. A. (2017). Stiffness and yield strength of architectured foams based on the schwarz primitive triply periodic minimal surface. *International Journal of Plasticity*, 95:1–20.

[67] Leng, J., Schafer, B. W., and Buonopane, S. G. (2013). Modeling the seismic response of cold-formed steel framed buildings: model development for the cfs-nees building. In *Proceedings of the Annual Stability Conference-Structural Stability Research Council*.

[68] Liu, L., Kamm, P., García-Moreno, F., Banhart, J., and Pasini, D. (2017). Elastic and failure response of imperfect three-dimensional metallic lattices: the role of geometric defects induced by selective laser melting. *Journal of the Mechanics and Physics of Solids*, 107:160–184.

[69] Liu, P., Peterman, K. D., and Schafer, B. W. (2012). Test report on cold-formed steel shear walls. *Research Report CFS-NEES, RR03, June 2012*.

[70] Liu, P., Peterman, K. D., and Schafer, B. W. (2014). Impact of construction details on osb-sheathed cold-formed steel framed shear walls. *Journal of Constructional Steel Research*, 101:114–123.

[71] Lowes, L., Mitra, N., and Altoontash, A. (2004). A beam-column joint model for simulating the earthquake response of reinforced concrete frames, peer report 2003/10, pacific earthquake engineering research center. *University of California, Berkeley*.

[72] Macillo, V., Fiorino, L., and Landolfo, R. (2017). Seismic response of cfs shear walls sheathed with nailed gypsum panels: Experimental tests. *Thin-Walled Structures*, 120:161–171.

[73] MATLAB (2019). The MathWorks Inc., Natick, Massachusetts.

[74] McKenna, F., Fenves, G., Jeremic, B., and Scott, M. (2015). Open system for earthquake engineering simulation, 2000. *URL http://opensees. berkeley. edu.[May 2008].*

[75] Meza, L. R., Zelhofer, A. J., Clarke, N., Mateos, A. J., Kochmann, D. M., and Greer, J. R. (2015). Resilient 3d hierarchical architected metamaterials. *Proceedings of the National Academy of Sciences*, 112(37):11502–11507.

[76] Mohebbi, S., Mirghaderi, S. R., Farahbod, F., Sabbagh, A. B., and Torabian, S. (2016). Experiments on seismic behaviour of steel sheathed cold-formed steel shear walls cladded by gypsum and fiber cement boards. *Thin-Walled Structures*, 104:238–247.

[77] Mohr, D. (2005). Mechanism-based multi-surface plasticity model for ideal truss lattice materials. *International Journal of Solids and Structures*, 42(11-12):3235–3260.

[78] Ngo, H. H. (2014). Numerical and experimental studies of wood sheathed cold-formed steel framed shear walls. M.S. thesis, Johns Hopkins University, Baltimore, MD.

[79] Okasha, A. F. (2004). Performance of steel frame / wood sheathing screw connections subjected to monotonic and cyclic loading. M.Eng. thesis, McGill University, Montreal, Canada.

[80] O'Masta, M., Dong, L., St-Pierre, L., Wadley, H., and Deshpande, V. (2017). The fracture toughness of octet-truss lattices. *Journal of the Mechanics and Physics of Solids*, 98:271–289.

[81] Papka, S. and Kyriakides, S. (1999). Biaxial crushing of honeycombs:—part 1: Experiments. *International Journal of Solids and Structures*, 36(29):4367–4396.

[82] Papka, S. D. and Kyriakides, S. (1998). In-plane crushing of a polycarbonate honeycomb. *International Journal of Solids and Structures*, 35(3-4):239–267.

[83] Peterman, K. D., Nakata, N., and Schafer, B. W. (2014). Hysteretic characterization of cold-formed steel stud-to-sheathing connections. *Journal of Constructional Steel Research*, 101:254–264.

[84] Peterman, K. D., Stehman, M. J., Madsen, R. L., Buonopane, S. G., Nakata, N., and Schafer, B. W. (2016a). Experimental seismic response of a full-scale cold-formed steel-framed building. i: System-level response. *Journal of Structural Engineering*, 142(12):04016127.

[85] Peterman, K. D., Stehman, M. J., Madsen, R. L., Buonopane, S. G., Nakata, N., and Schafer, B. W. (2016b). Experimental seismic response of a full-scale cold-formed steel-framed building. ii: Subsystem-level response. *Journal of Structural Engineering*, 142(12):04016128.

[86] Peterson, J., Seide, P., and Weingarten, V. (1968). Buckling of thin-walled circular cylinders.

[87] Romijn, N. E. and Fleck, N. A. (2007). The fracture toughness of planar lattices: Imperfection sensitivity. *Journal of the Mechanics and Physics of Solids*, 55(12):2538–2564.

[88] Schaedler, T. A., Jacobsen, A. J., Torrents, A., Sorensen, A. E., Lian, J., Greer, J. R., Valdevit, L., and Carter, W. B. (2011). Ultralight metallic microlattices. *Science*, 334(6058):962–965.

[89] Schafer, B. W., Ayhan, D., Leng, J., Liu, P., Padilla-Llano, D., Peterman, K. D., Stehman, M., Buonopane, S. G., Eatherton, M., Madsen, R., et al. (2016). Seismic response and engineering of cold-formed steel framed buildings. In *Structures*, volume 8, pages 197–212. Elsevier.

[90] Schafer, B. W., Li, Z., and Moen, C. D. (2010). Computational modeling of cold-formed steel. *Thin-Walled Structures*, 48(10-11):752–762.

[91] Schafer, B. W., Sangree, R. H., and Guan, Y. (2007). Experiments on rotational restraint of sheathing: final report. *American Iron and Steel Institute–Committee on Framing Standards, Washington, DC.*

[92] Seide, P., Weingarten, V., and Morgan, E. (1960). The development of design criteria for elastic stability of thin shell structures. Technical report, TRW Space Technology Labs Los Angeles CA.

[93] Selvaraj, S. and Madhavan, M. (2019). Investigation on sheathing-fastener connection failures in cold-formed steel wall panels. In *Structures*, volume 20, pages 176–188. Elsevier.

[94] Serrette, R., Encalada, J., Hall, G., Matchen, B., Nguygen, H., and Williams, A. (1997a). Additional shear wall values for light weight steel framing. Report. No. LGSRG-1-97, Light Gauge Steel Research Group, Department of Civil Engineering, Santa Clara University, Santa Clara, Calif.

[95] Serrette, R., Nguyen, H., and Hall, G. (1996). Shear wall values for light weight steel framing. Report. No. LGSRG-3-96, Light Gauge Steel Research Group, Department of Civil Engineering, Santa Clara University, Santa Clara, Calif.

[96] Serrette, R. L., Encalada, J., Juadines, M., and Nguyen, H. (1997b). Static racking behavior of plywood, osb, gypsum, and fiberbond walls with metal framing. *Journal of Structural Engineering*, 123(8):1079–1086.

[97] Serrette, R. L., Morgan, K. A., and Sorhouet, M. A. (2002). Performance of cold-formed steel-framed shear walls: Alternative configurations. *Final Report: LGSRG-06-02, Santa Clara University, Santa Clara, CA.*

[98] Simpson Strong-Tie Co. Inc. (2001). Light gauge steel construction connectors. *Dublin, CA, USA.*

[99] Singh, A. and Hutchinson, T. C. (2018). Finite element modeling and validation of steel-sheathed cold-formed steel framed shear walls. In *Proceedings of the International Specialty Conference on Cold-Formed Steel Structures. St. Louis, Missouri.*

[100] Singh, A., Wang, X., Zhang, Z., Derveni, F., Castaneda, H., Peterman, K., Schafer, B., and Hutchinson, T. (2020). Lateral response of cold-formed steel framed steel sheathed in-line wall systems detailed for mid-rise build.

[101] Symons, D. D. and Fleck, N. A. (2008). The imperfection sensitivity of isotropic two-dimensional elastic lattices. *Journal of Applied Mechanics*, 75(5).

[102] Tancogne-Dejean, T., Diamantopoulou, M., Gorji, M. B., Bonatti, C., and Mohr, D. (2018). 3d plate-lattices: An emerging class of low-density metamaterial exhibiting optimal isotropic stiffness. *Advanced Materials*, 30(45):1803334.

[103] Tancogne-Dejean, T., Li, X., Diamantopoulou, M., Roth, C., and Mohr, D. (2019). High strain rate response of additively-manufactured plate-lattices: experiments and modeling. *Journal of Dynamic Behavior of Materials*, 5(3):361–375.

[104] Tancogne-Dejean, T. and Mohr, D. (2018a). Elastically-isotropic truss lattice materials of reduced plastic anisotropy. *International Journal of Solids and Structures*, 138:24–39.

[105] Tancogne-Dejean, T. and Mohr, D. (2018b). Stiffness and specific energy absorption of additively-manufactured metallic bcc metamaterials composed of tapered beams. *International Journal of Mechanical Sciences*, 141:101–116.

[106] Tao, F., Chatterjee, A., and Moen, C. D. (2017). Monotonic and cyclic response of single shear cold-formed steel-to-steel and sheathing-to-steel connections. Report. No. CE/VPI-ST-16-01, Virginia Tech., Blacksburg, Virginia.

[107] Vieira, L. and Schafer, B. W. (2009). Experimental results for translational stiffness of stud-sheathing assemblies. *AISI-COFS Project on Sheathing Braced Design of Wall Studs.*

[108] Vieira Jr, L. C. M. and Schafer, B. W. (2012). Lateral stiffness and strength of sheathing braced cold-formed steel stud walls. *Engineering Structures*, 37:205–213.

[109] Wallach, J. and Gibson, L. (2001). Mechanical behavior of a three-dimensional truss material. *International Journal of Solids and Structures*, 38(40-41):7181–7196.

[110] Wang, X., Pantoli, E., Hutchinson, T., Restrepo, J., Wood, R., Hoehler, M., Grzesik, P., and Sesma, F. (2015). Seismic performance of cold-formed steel wall systems in a full-scale building. *Journal of Structural Engineering*, 141(10):04015014.

[111] Wang, Y. M., Voisin, T., McKeown, J. T., Ye, J., Calta, N. P., Li, Z., Zeng, Z., Zhang, Y., Chen, W., Roehling, T. T., et al. (2018). Additively manufactured hierarchical stainless steels with high strength and ductility. *Nature materials*, 17(1):63–71.

[112] Wicks, N. and Hutchinson, J. W. (2001). Optimal truss plates. *International journal of solids and structures*, 38(30-31):5165–5183.

[113] Winter, G. (1960). Lateral bracing of beams and columns. *ASCE Transactions, Paper*, (3044).

[114] Yadav, K. K., Cuccia, N. L., Virot, E., Rubinstein, S. M., and Gerasimidis, S. (2021). A nondestructive technique for the evaluation of thin cylindrical shells' axial buckling capacity. *Journal of Applied Mechanics*, 88(5):051003.

[115] Yadav, K. K. and Gerasimidis, S. (2020). Imperfection insensitivity of thin wavy cylindrical shells under axial compression or bending. *Journal of Applied Mechanics*, 87(4).

[116] Yu, C. (2010). Shear resistance of cold-formed steel framed shear walls with 0.686 mm, 0.762 mm, and 0.838 mm steel sheet sheathing. *Engineering Structures*, 32(6):1522–1529.

[117] Zeynalian, M. and Ronagh, H. R. (2015). Seismic performance of cold formed steel walls sheathed by fibre-cement board panels. *Journal of Constructional Steel Research*, 107:1–11.

[118] Zhang, W., Mahdavian, M., Li, Y., and Yu, C. (2017). Experiments and simulations of cold-formed steel wall assemblies using corrugated steel sheathing subjected to shear and gravity loads. *Journal of Structural Engineering*, 143(3):04016193.

[119] Zhang, Z., Singh, A., Derveni, F., Torabian, S., Peterman, K., Hutchinson, T., and Schafer, B. (2020). Cyclic performance of steel sheet connections for cfs framed steel sheet sheathed shear walls.

[120] Zheng, X., Lee, H., Weisgraber, T. H., Shusteff, M., DeOtte, J., Duoss, E. B., Kuntz, J. D., Biener, M. M., Ge, Q., Jackson, J. A., et al. (2014). Ultralight, ultrastiff mechanical metamaterials. *Science*, 344(6190):1373–1377.